DYNAMIC DISPLACEMENT ANALYSIS OF A SHALLOW LANDSLIDE IN NORWOOD TUFF

by

Keith Eric Beisner

A thesis submitted to the faculty of
The University of Utah
in partial fulfillment of the requirements for the degree of

Master of Science

in

Geological Engineering

Department of Geology and Geophysics

The University of Utah

May 2011

The University of Utah Graduate School

STATEMENT OF THESIS APPROVAL

The thesis of **Keith Eric Beisner**

has been approved by the following supervisory committee members:

Aurelian C. Trandafir	, Chair	**11/04/2010** Date Approved
Ronald L. Bruhn	, Member	**11/04/2010** Date Approved
James C. Pechmann	, Member	**11/04/2010** Date Approved

and by **D. Kip Solomon** , Chair of the Department of **Geology and Geophysics**

and by Charles A. Wight, Dean of The Graduate School.

ABSTRACT

Northern Utah has a long history of landslides occurring on natural and man-made slopes. Earthquake activity in this region may exacerbate the incidence of landslides, thus increasing the potential of landslide related damage to residential structures and transportation corridors. In this context, the present study addresses the earthquake response in both drained and undrained conditions of a typical, shallow landslide in northern Utah occurring in completely decomposed Norwood Tuff. The slide mass geometry was obtained using a 2-D seismic refraction profile and previously collected geotechnical borehole data. The Newmark sliding block analysis was employed with a translational failure mechanism to determine the permanent dynamic slope displacements under various input accelerograms. The yield coefficient for both drained and undrained conditions was obtained from pseudo-static limit-equilibrium slope stability analyses. Based on the computational results, a methodology to evaluate the peak ground acceleration threshold that would distinguish between insignificant ground movement and potentially damaging slope displacements during an earthquake was developed. A normalized Arias intensity was subsequently used to compare the dynamic displacements in dry and partially saturated conditions. Dry slopes comprised of completely decomposed Norwood Tuff that experience

earthquake accelerations greater than 0.55*g* are considered unsafe against damaging displacements. Slopes that are partially saturated or contain a perched water table are considered unsafe when earthquake accelerations exceed 0.47*g*. Dynamic displacements in completely decomposed Norwood Tuff increase exponentially for partially saturated slopes relative to dry slopes as the normalized Arias intensity increases.

TABLE OF CONTENTS

APPENDICES

LIST OF TABLES

Table

CHAPTER 1

INTRODUCTION

Utah has a long history of landslide and earthquake activity. Risks associated with these two hazards include damage to homes and businesses, transportation corridors, and potential loss of human life. While much research has been done on landslides and earthquakes in Utah separately, there are little data relating earthquake energy and landslide displacement thresholds. Northern Utah provides an excellent study area for the potential of earthquake-induced landslides given the large number of active landslides in Norwood Tuff in this region combined with an historically active normal-fault system capable of producing large earthquakes (Figure 1.1). Urban development in this region is also accelerating and more construction occurs on hill slopes, thus increasing the need for understanding the risks posed by geologic activity in the area.

Geologic Setting

Northern Utah, from the Wasatch Range eastward, is considered part of the Middle Rocky Mountains physiographic province (Stokes, 1977). Coogan and King (2006) mapped the geologic sequence of the study area. The

crystalline basement consists of Precambrian Farmington Canyon rocks dating to the early Proterozoic. Cambrian and Mississippian marine sedimentary strata unconformably overlie the Precambrian basement rocks. The Cenozoic age Wasatch Formation, consisting mostly of conglomerate and sandstone, lies unconformably above the Precambrian and Paleozoic units. The Salt Lake Formation overlies the Wasatch Formation. The Norwood Tuff, a Tertiary age volcanic unit, is included as part of the Salt Lake Formation. The volcanic tuff underlies middle and upper Pleistocene glacial deposits. Laminations and thinly bedded structures observed in the Norwood Tuff indicate that they were originally deposited in a near-shore lacustrine environment. Subsequent fluvial reworking, weathering, and metamorphism of this material resulted in the formation of claystone, siltstone, and sometimes sandstone layers. The tuff also includes lenses of conglomerate containing chert and carbonate clasts.

Based on available geotechnical information from boreholes, Trandafir and Amini (2009) developed a generalized subsurface profile for the study region. This includes a 0.3-m thick topsoil at the surface underlain by glacial till with thicknesses ranging within 1-5 m (also reaching up to 10 m in some areas). Decomposed Norwood Tuff with thicknesses of 1.0 - 4.5 m underlies the glacial till and grades into fresh bedrock tuff at 7 – 12 m below the ground surface.

The structural history of the study area consists of thrust faulting and associated mountain building as part of the Sevier Orogeny, followed by normal faulting associated with the eastern edge of Basin and Range extension. The Willard and Ogden Thrust faults, active at approximately 120 Ma and 90 Ma,

respectively, were responsible for faulting and folding Paleozoic units and the formation of the Wasatch Range. Tertiary volcanism deposited the Norwood Tuff approximately 37 million years ago, covering the Cretaceous-aged deformation. Subsequent Cenozoic extension related to reactivation of thrust faults as normal faults resulted in the formation of Ogden and Morgan valleys.

Landslide Hazards

Landslide hazards in Northern Utah exist both on natural and man-made slopes. Landslides in this region are responsible for damage to residential homes, transportation corridors, and buried utility and sewer lines (Ashland, 2007). Landslides in completely decomposed Norwood Tuff have sheared home foundations and cracked residential walls (Figure 1.2a). Most landslides experience movement annually during spring and early summer snowmelt due to elevated groundwater levels and saturated soils. While this annual movement is generally not catastrophic, potentially damaging displacements can occur during unusually high precipitation or after several years of high snowpack, precipitation, and increased groundwater levels.

Landslide activity on cut slopes along the Snowbasin Access Road (State Highway 226) provides a case study for determining the failure threshold in shallow landslides comprised of Norwood Tuff. Previous mapping and reconnaissance surveys show that landslides affect approximately 35% of the cut slopes along the road (Trandafir and Amini, 2009). These landslides are

responsible for significant damage to State Highway 226 that requires yearly maintenance (Figure 1.2b).

Seismic Hazards

Earthquakes have the potential to reactivate previously existing landslides and even trigger new catastrophic failures. Landslide activity near Draper, Utah provides evidence for reactivation of pre-existing landslides due to surface-faulting events in the late Holocene (Ashland, 2008a). Data also suggest that earthquake-induced failures can occur during relatively dry periods (Ashland, 2008). The moment magnitude (M_w) 5.5 St. George earthquake in 1992 was responsible for the occurrence of the Springdale, Utah landslide (Jibson and Harp, 1995). This event also showed that despite a large distance from the epicenter and modest predicted displacements, increased pore pressures were sufficient to destabilize the sliding surface and cause greater movement than expected (Jibson and Harp, 1996).

The landslide study area in the present study is located on the western edge of the Rocky Mountain physiographic province and borders the eastern edge of the Basin and Range province. The Wasatch Fault Zone (WFZ) forms a boundary between these two provinces. This fault zone trends north-south and extends approximately 343 km along the western base of the Wasatch Mountain Range. The WFZ is comprised of 10 segments, each capable of rupturing independently and generating magnitude 7+ earthquakes. These earthquakes

pose a major threat to the expanding population and infrastructure located along the Wasatch Front.

The landslide area along the Snow Basin access road is located on the footwall side of the Weber Segment of the WFZ. The Weber Segment is one of five central segments that show evidence of multiple surface-faulting earthquakes in the last 6000 years (Duross, 2009). The end-to-end length of the segment is 56 km and the surface trace length is 61 km (Machette et al., 1991). The expected moment magnitude of an earthquake on the Weber Segment is 7.17 based on the fault-length empirical relationships presented by Wells and Coppersmith (1994).

Paleoseismology studies have used trenching data to constrain the age, recurrence interval, and displacement of earthquakes on the Weber Segment (Duross et al., 2009; Nelson et al., 2006; McCalpin et al., 1994; Forman et al., 1991). While each trench site yielded differing earthquake ages, the Utah Quaternary Fault Parameters Working Group determined the ages and uncertainties for the five most recent surface-faulting events on the Weber Segment. Based on these data, the consensus recurrence interval for the Weber Segment is 1.4 kyr with a 2-sigma error ranging from .5 to 2.4 kyr (Lund, 2005). Recent trench work determined that the most recent event occurred 490-630 cal yr BP (Duross et al., 2009). The estimated average surface displacement for the five most recent events ranges from 1.6-2.5 m (Duross et al., 2009).

Objective

The objective of this study is to determine peak ground acceleration thresholds that would trigger large, potentially damaging dynamic displacements of shallow landslides in completely decomposed Norwood Tuff during an earthquake. In addition this study will analyze the relationship between the earthquake energy of an earthquake and the displacements expected at the landslide site for dry and semisaturated conditions. The proposed approach employs field and laboratory geotechnical data with a Newmark sliding block formulation for assessing drained and undrained seismic slope displacements. The results of this study will be helpful in developing effective mitigation strategies against earthquake-induced shallow landslide hazards in completely decomposed Norwood Tuff.

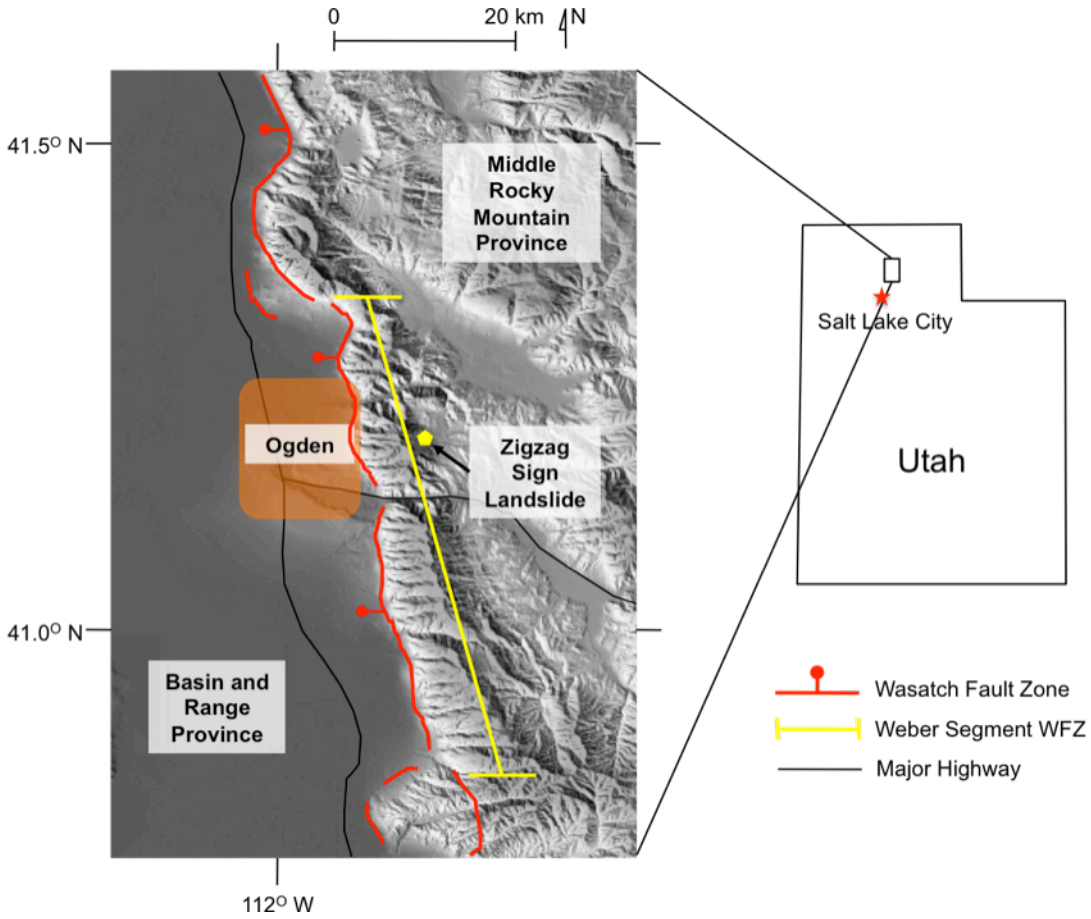

Figure 1.1. Regional study location.

Figure 1.2. Damage to residential and transportation corridors. a**.** Landslide scarp migration responsible for damage to a home foundation (photos provided by Utah Geological Survey). b. Shear zone development on the flank of a landslide located along the Snowbasin Access Road is responsible for road damage.

CHAPTER 2

GEOLOGIC ENGINEERING FEATURES OF THE ZIGZAG SIGN LANDSLIDE

Type of Movement, Materials, and Groundwater Conditions

Zigzag sign landslide may be regarded as a typical shallow landslide characterizing the failure mode of cut slopes in Norwood Tuff along the Snowbasin Access Road (Figure 2.1). The slide can be categorized as a slump-earthflow complex exhibiting translational movement along a planar sliding surface. The landslide experiences slow, down-slope movement and deformation during and immediately following spring snowmelt. Deformation features include a slump near the head scarp, formation of a secondary scarp near the center of the landslide, and a thrust system at the toe of the slide. The landslide surface is characterized by a hummocky topography with fractures and sag ponds encountered at various locations. Examination of borehole data combined with dynamic cone penetration tests conducted at the landslide location revealed that the slide mass, consisting of completely decomposed

Norwood Tuff, is underlain by a thinly bedded carbonate rock which is very stiff and dips parallel to the slope face (Trandafir and Amini, 2009).

The Utah Geological Survey has monitored groundwater conditions in the area (Ashland et al., 2008b). Results from monitoring the Green Pond Landslide and Bear Wallow Landslide, both located along Snow Basin Access Road, indicate an annual increase in groundwater levels following spring snow melt (Ashland et al., 2008b). This study also concludes that water tables are compartmentalized within the large landslide masses in the area due to low-permeability clays and internal shear zones. The carbonate layer underlying the zone of deformation in the Zigzag Sign landslide may potentially develop perched water tables within the decomposed Norwood Tuff material. As the water levels increase, the pore-water pressure increases and may induce slide mass deformations as driving forces overcome resisting forces within the landslide. During late spring and summer groundwater levels decrease due to water absorption by vegetation and a semiarid environment, thus reducing the likelihood of landslide deformations.

Slide Mass Geometry

The slide mass geometry was determined using a P-wave seismic refraction test of the deformed landslide, as well as geotechnical data from borehole and dynamic cone penetration tests. First an elevation profile was constructed using a handheld leveling scope. Subsequently, a 45-m long seismic refraction profile was developed using 45 4.5 Hz geophones spaced 1 m

apart and connected to a 16-bit seismograph. A sledgehammer impacting a metal plate at the ground surface was used as a source and 15 stacks of the sledgehammer were used for each shot. The profile was located along the landslide surface perpendicular to the head scarp and parallel to the direction of movement.

The data from the seismic refraction profile were processed using ProMAX2D Seismic Data Processing software. Because of the short profile length and closely spaced receivers, first arrival times were manually chosen for the direct wave of each of the 48 shots. The elevation profile and first arrival times were then imported into Matlab to determine the refraction interface and velocity profiles.

Results from the seismic refraction profile indicate that bedding is parallel to the slope surface. At approximately 3 – 5 m depth the P-wave velocities increase to greater than 1000 m/s, possibly indicating fresh Norwood Tuff below the sliding surface (Figure 2.2). This interpretation correlates with unpublished geotechnical borehole data that show a stiff, sandy clay at approximately 5 m depth. Slickensides present within this material indicate a potential sliding surface at the interface between decomposed Norwood Tuff and a stiff carbonate layer.

Geotechnical Characteristics

Disturbed samples of completely decomposed Norwood Tuff were used for laboratory index property testing whereas undisturbed specimens required for

triaxial testing were collected from the shear surface of Zigzag Sign landslide using thin-walled tube samplers (Trandafir and Amini, 2009). The undisturbed sampling procedure involved the application of a smooth thrust in order to insert the tube sampler into the Norwood Tuff material. The techniques used for laboratory index properties are described by Reddy (2002). Intact, initially wet samples of completely decomposed Norwood Tuff subjected to drying exhibited cracks that indicate the potential for swelling of this material upon wetting. Grain size analysis results show that the completely decomposed Norwood Tuff contains 82% sand and 18% fines (Figure 2.3). Additionally, Atterberg's limits tests provided a liquid limit (LL) of 37% and a plasticity index (PI) of 13%. The plastic limit (PL), was calculated using

$$PL = LL - PI \tag{1}$$

The plastic limit for completely decomposed Norwood Tuff is 25%. In the Unified Soil Classification System these test results classify the completely decomposed Norwood Tuff as clayey sand. The permeability of the clay was calculated using the cohesive index approach (Conforth, 2005):

$$CI = \frac{PI}{PL} \tag{2}$$

The cohesive index for completely decomposed Norwood Tuff is 0.52, yielding a coefficient of permeability for completely decomposed Norwood Tuff, $k = 5 \times 10^{-9}$ m/sec.

An X-Ray diffractometer available at the University of Utah was used to analyze the mineralogy of decomposed Norwood Tuff (Trandafir and Amini, 2009). X-Ray diffraction results indicate that smectite is the main clay mineral, whereas quartz and calcite were the two main nonclay minerals (Trandafir and Amini, 2009; Figure 2.4).

In-situ index properties for undisturbed samples of completely decomposed Norwood Tuff were previously determined, including a void ratio of 0.785, porosity of 44%, saturated unit weight of 19.1 kN/m^3, dry unit weight of 14.7 kN/m^3, and average specific gravity of 2.63 (Trandafir and Amini, 2009). The same study used a multistage consolidated-undrained triaxial compression test to determine the Mohr-Coulomb shear strength parameters of decomposed Norwood Tuff. The parameters derived include the effective cohesion intercept, $c' = 4.2$ kPa, and the effective friction angle, $\varphi' = 27^{O}$ (Trandafir and Amini, 2009).

Static Safety Factor and Finite-element Computed Static Stresses

Static conditions of the deformed Zigzag Sign landslide were modeled with Geostudio engineering software developed by Geo-Slope International, Ltd. The limit equilibrium method built into Slope/W module was utilized to study the static

slope stability. Other modules employed for this study include the finite-element based Seep/W for studying groundwater conditions, as well as Sigma/W for studying stress-deformation characteristics within the landslide mass. The model geometry used for each model was developed using a combination of seismic refraction, borehole, and dynamic cone penetration test data for the Zigzag Sign landslide.

Groundwater flow and pore-water pressures were modeled using the finite-element module, Seep/W, for the case of a perched ground water table within the slide mass. Boundary conditions for seepage analysis included a zero pressure head boundary at the water table location and an impervious boundary at the contact between the slide mass and bedrock. A steady-state flow analysis was subsequently performed in Seep/W in order to calculate the pore water pressures throughout the slide mass. Based on the finite-element analysis, the pore-water pressure at the sliding surface is approximately 18 kPa.

The Slope/W module, which is based on the method of slices, was used to study the static stability of the slope. Bedrock and slide mass material were the two regions modeled (Figure 2.5). The bedrock was considered impenetrable while the slide mass material was governed by the Mohr-Coulomb failure criterion. Material properties involved in modeling the slide mass included the unit weight of completely decomposed Norwood Tuff – 19.1 kN/m^3, the effective cohesion – 4.2 kPa, and the effective friction angle – 27^O (Trandafir and Amini, 2009). The Slope/W model employed an automatic search procedure to determine the exit point on the slip surface associated with the minimum safety

factor for the given slope configuration. For the deformed Zigzag Sign landslide model, a finite-element analysis of the landslide deformation pattern revealed the formation of a secondary scarp in the central portion of the landslide (Trandafir and Amini, 2009), which agrees with actual observations in the field. Janbu's method was used to calculate the static safety factors along the sliding surface for the slope with and without a groundwater table within the slide mass (Janbu, 1954). The safety factor (*FS*) for the drained, deformed slope is 1.36 (Figure 2.5a), thus indicating a stable slope under dry conditions. When the deformed slope experiences saturation due to development of a perched water table, the safety factor decreases to 1.15, still indicating a stable slope, but close to limit-equilibrium conditions (Figure 2.5b).

Finite-element modeling with the Sigma/W module was conducted in order to determine the static stress state within the slide mass. Three materials were used in the finite-element model, including the decomposed tuff adjacent to the slide mass, the slide mass material, and bedrock (Figure 2.6). The bedrock and decomposed tuff material were modeled as linear-elastic, while the slide mass material was modeled as an elasto-plastic material. Boundary conditions were applied to the sides and bottom of the landslide model. The side boundaries were defined as no horizontal displacements, whereas the base of the model was defined as a no horizontal and vertical displacement boundary.

The results from the finite-element analysis show the distribution of major and minor principal stresses within the slide mass (Figure 2.7). Node 162 in Figure 2.7 was selected as the point corresponding to the average height of the

slide and is thus representative for the average stresses (Figure 2.8). The finite-element computed total major and minor principal stresses at point A were 82 and 40 kPa, respectively (Figures 2.7a, 2.7b). The pore pressure obtained from the Sigma/W analysis at this location was 15 kPa (Figure 2.7c). The results from static finite-element modeling were used as initial stress conditions for an undrained cyclic triaxial test on completely decomposed Norwood Tuff that was conducted in order to determine the undrained cyclic shear resistance of this material (Figure 2.9).

Undrained Cyclic Triaxial Test on Completely Decomposed Norwood Tuff

An undrained cyclic triaxial compression test was performed to investigate the undrained shear behavior of saturated completely decomposed Norwood Tuff. The test was conducted on an undisturbed Norwood Tuff sample collected from the Zigzag Sign landslide near the main scarp (Trandafir and Amini, 2009). Prior to triaxial testing, the sample was saturated in the lab using back-pressure until a Skempton's B parameter greater than 0.95 (corresponding to a fully saturated sample) was achieved. The test specimen was subsequently subjected to anisotropic consolidation under effective vertical and horizontal stresses of 61 and 21 kPa, respectively. The sample was then subjected to 94 cycles of loading with a cyclic deviator stress amplitude of 48 kPa at a loading frequency of 1 Hz.

Results show an increase in pore pressure, with excess pore pressures reaching a maximum of 25 kPa after 60 cycles (Figure 2.10). As the axial strain

increased, the shear stress increased until the undrained maximum shear strength was achieved at 25.63 kPa (Figure 2.11). The effective stress path in Figure 2.12 shows a gradual shift toward the failure envelope due to an increase in pore water pressure with increasing number of loading cycles.

Figure 2.1. Zigzag Sign landslide located along the Snowbasin Access Road.

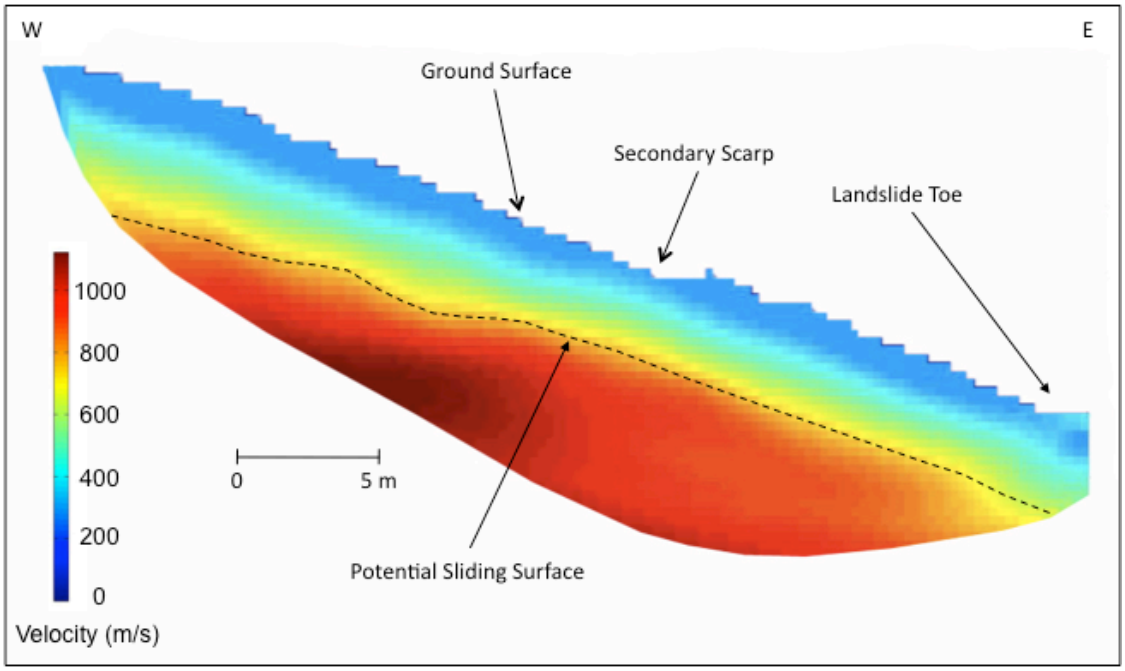

Figure 2.2. Seismic refraction velocity profile of the Zigzag Sign landslide.

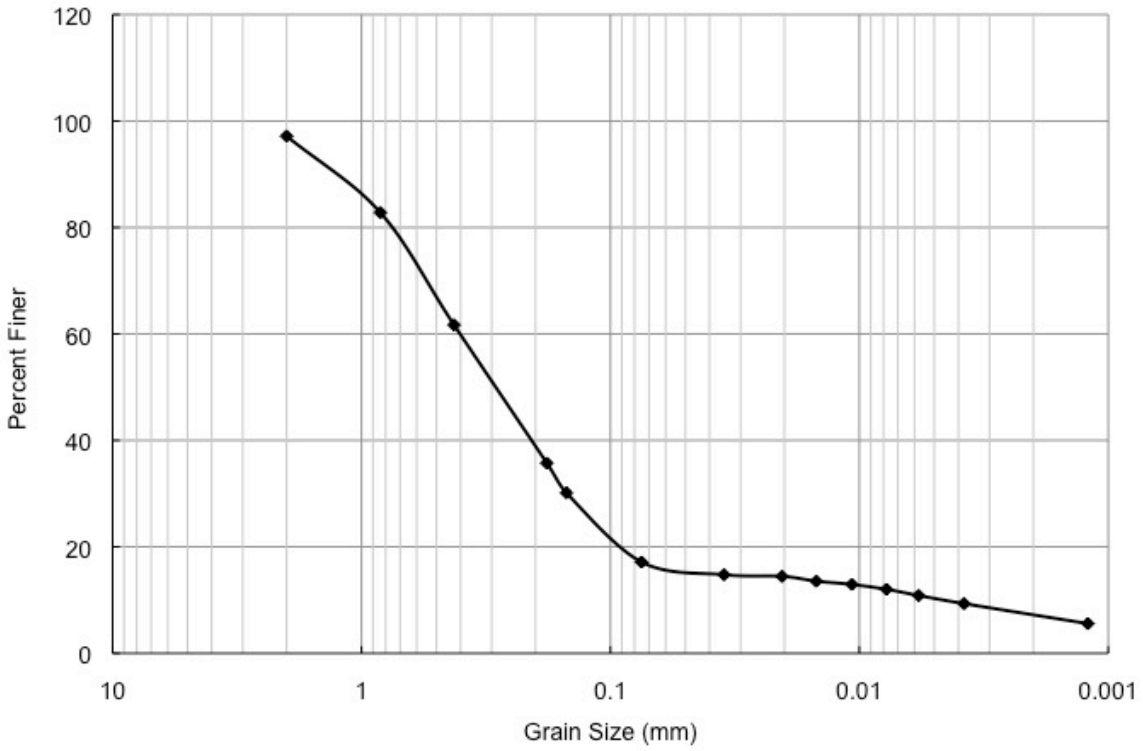

Figure 2.3. Completely decomposed Norwood Tuff grain size analysis.

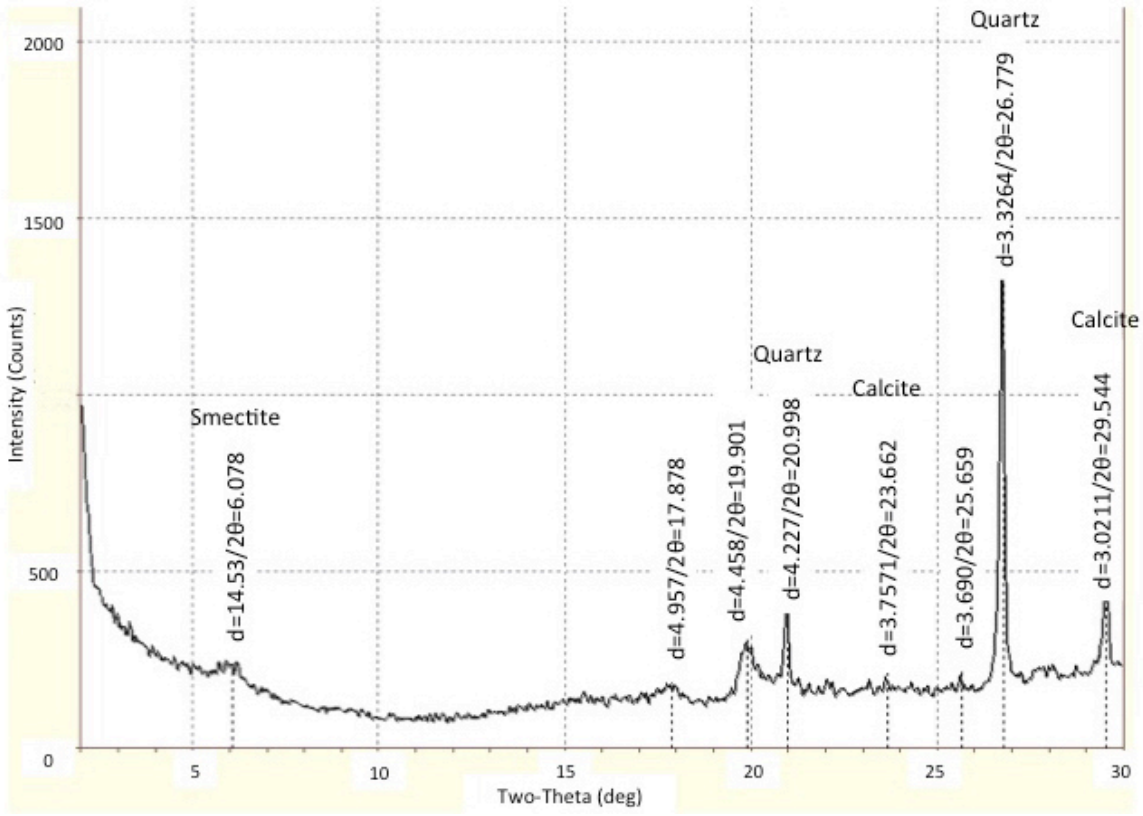

Figure 2.4. X-Ray diffraction results for completely decomposed Norwood Tuff.

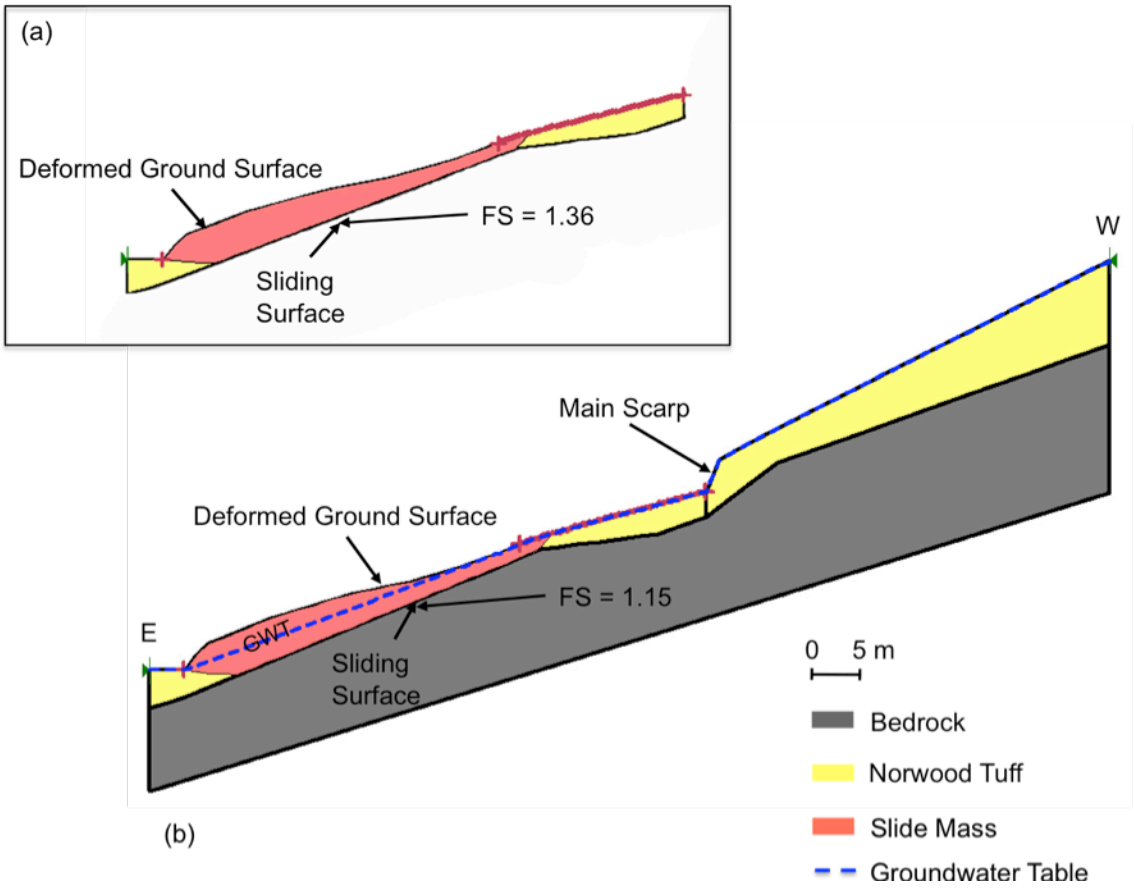

Figure 2.5. Static safety factors for the deformed Zigzag Sign landslide: a. dry slope, and b. slope with perched water table.

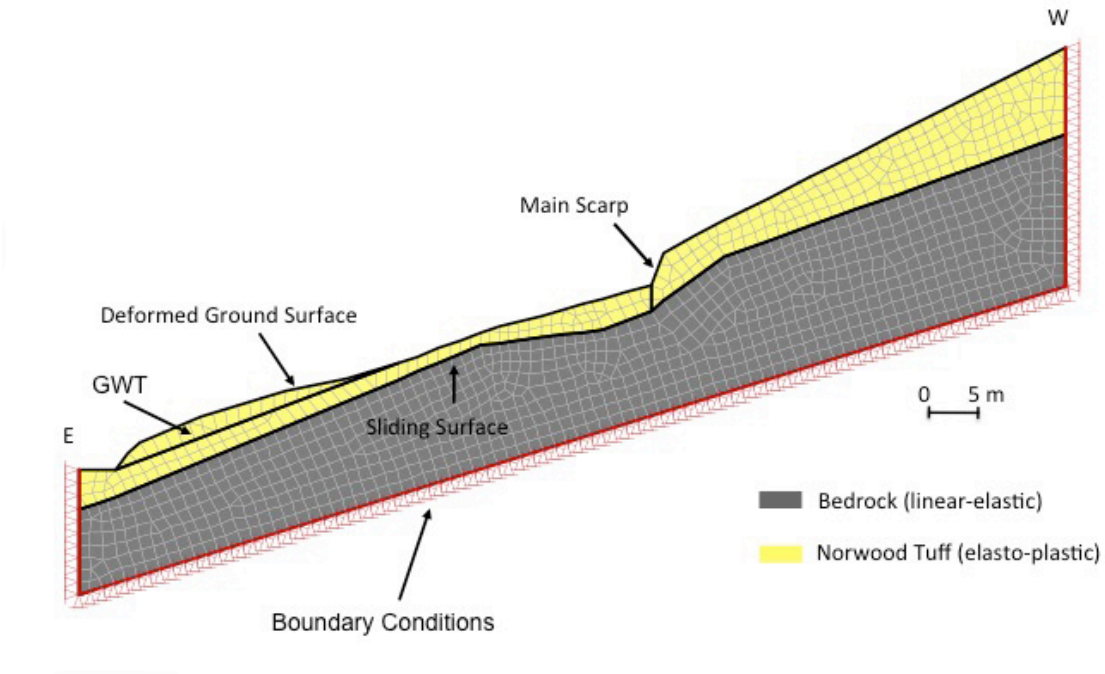

Figure 2.6. Finite-element mesh for the deformed Zigzag Sign landslide.

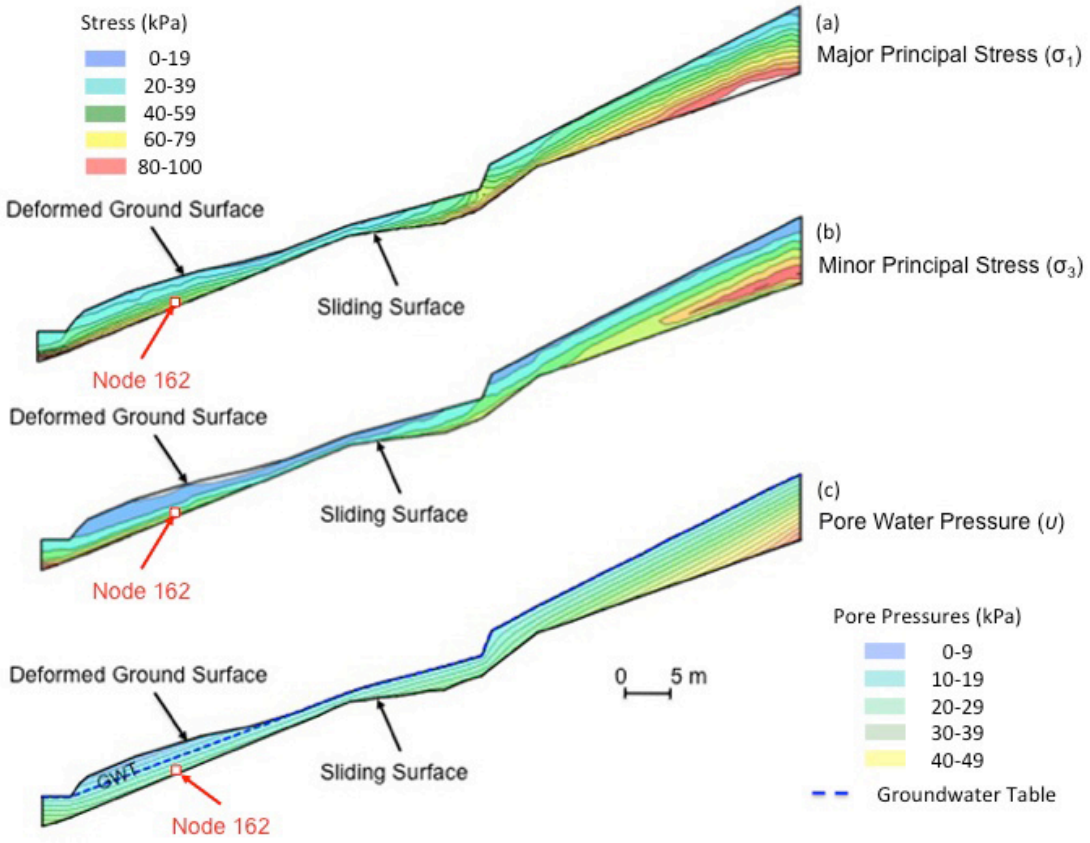

Figure 2.7. Finite-element analysis results: a. major principal stresses, b. minor principal stresses, and c. pore-water pressures.

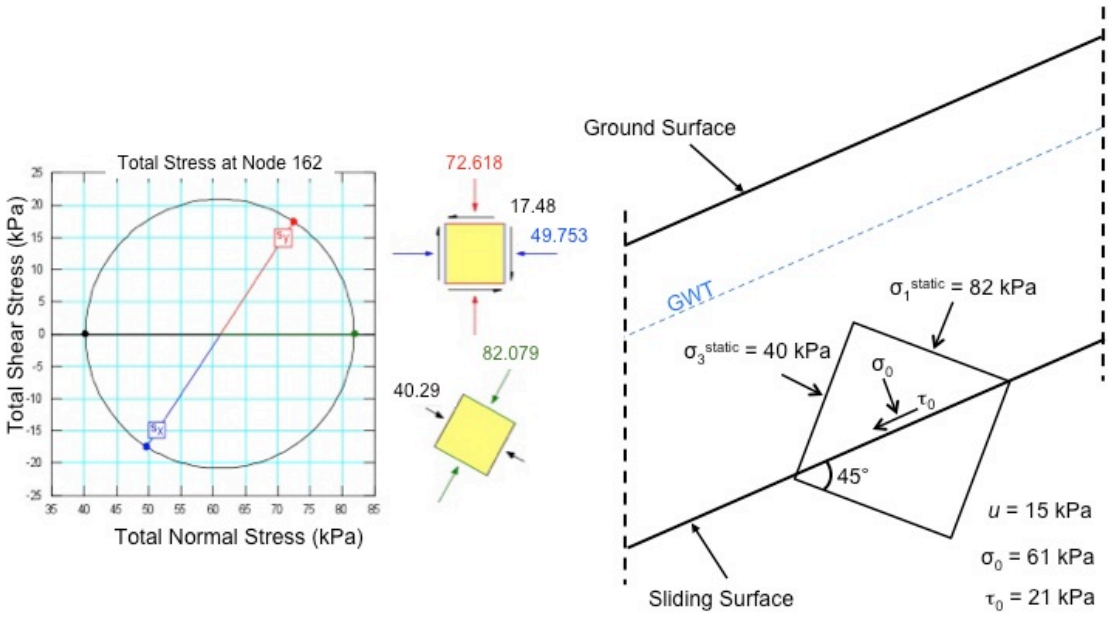

Figure 2.8. Total stress parameters obtained from Node 162, located along the sliding surface of the modeled Zigzag Sign landslide.

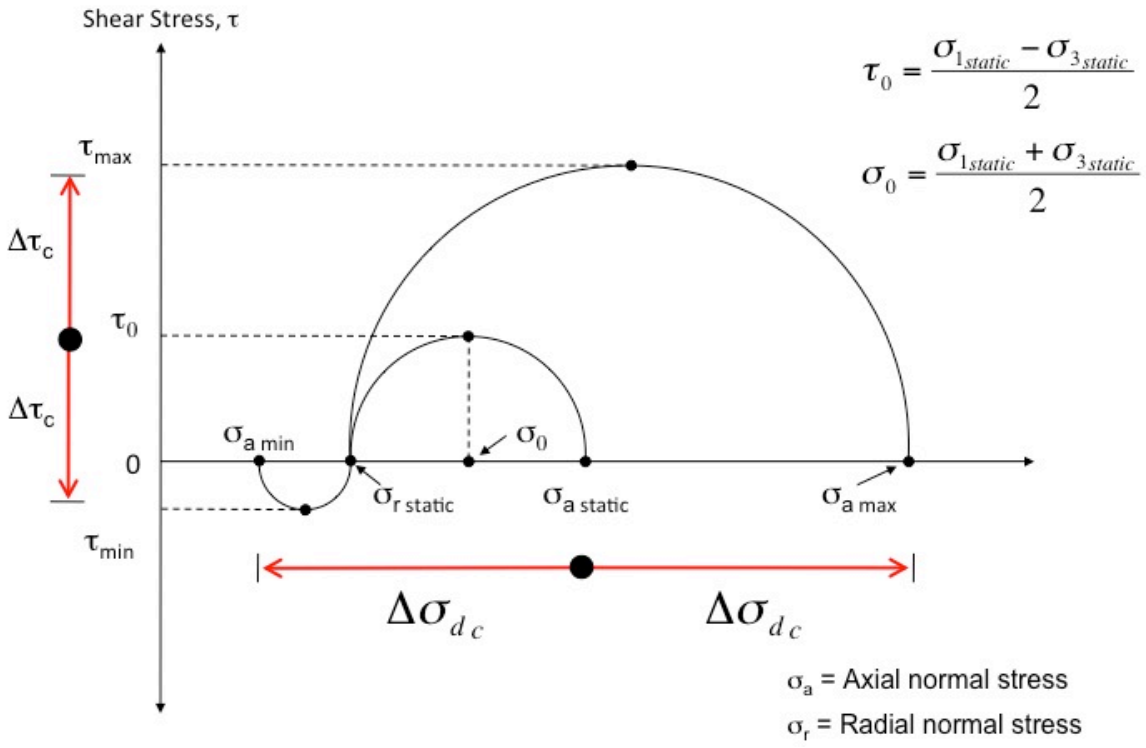

Figure 2.9. Cyclic triaxial test conditions on a sample of completely decomposed Norwood Tuff.

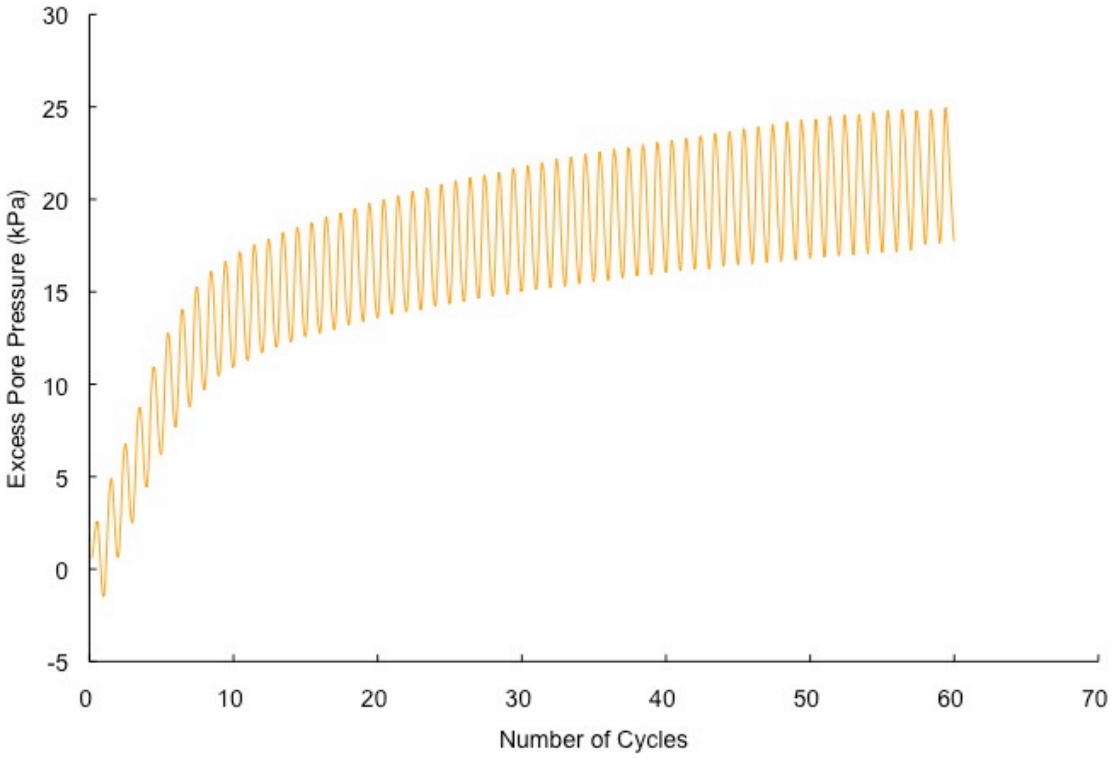

Figure 2.10. Excess pore pressure in relation to the number of cycles.

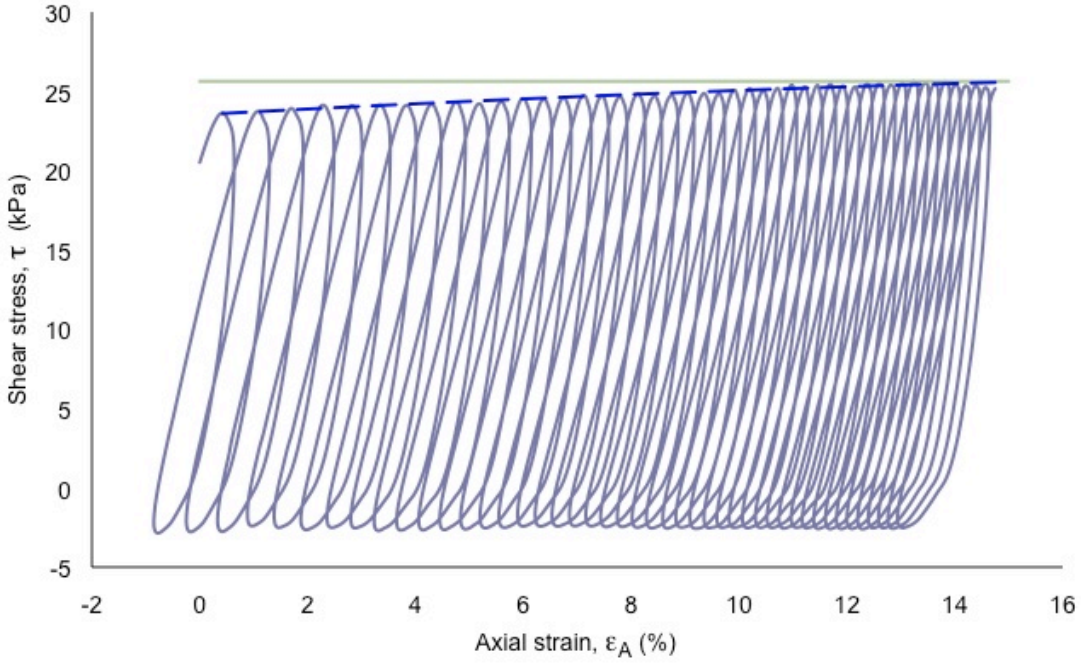

Figure 2.11. Shear stress in relation to axial strain.

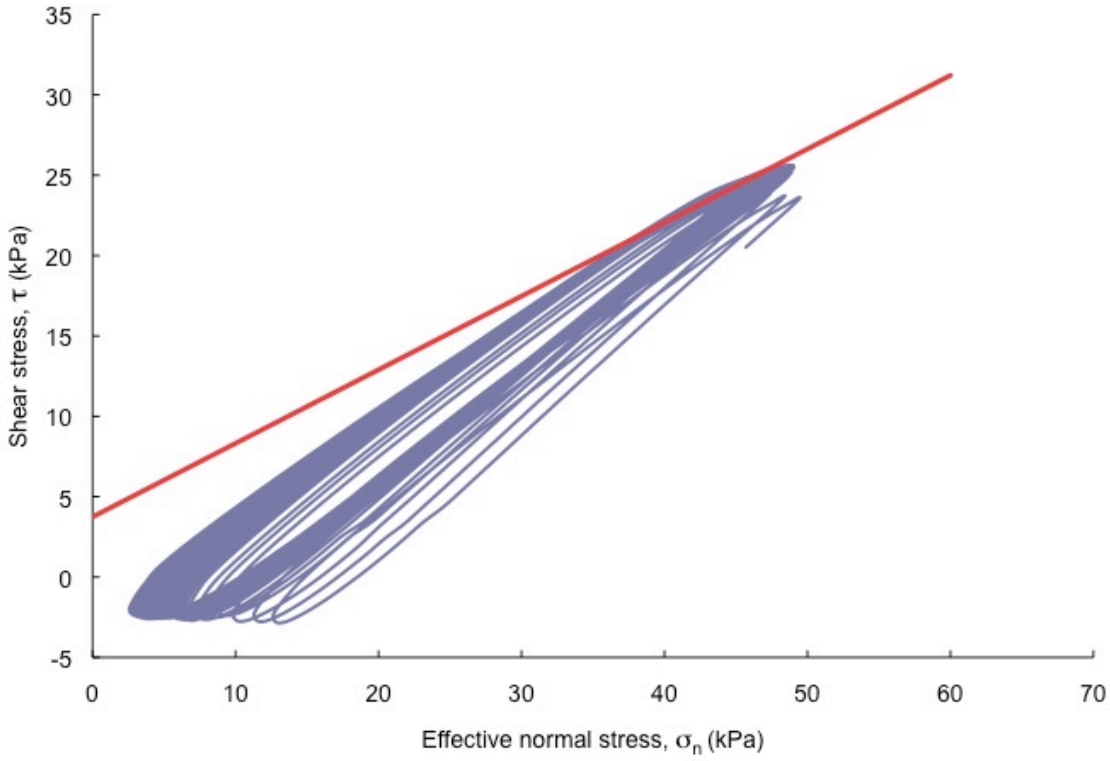

Figure 2.12. Effective stress path from the cyclic triaxial test.

CHAPTER 3

DYNAMIC DISPLACEMENT ANALYSIS OF THE ZIGZAG SIGN LANDSLIDE

This chapter addresses the earthquake response of Zigzag Sign landslide under various seismic events. The procedure for calculating permanent slope displacements involved determining the yield coefficient and constant of the equation of motion for drained and undrained conditions, respectively. Newmark displacements were then calculated using representative earthquakes obtained from the PEER online earthquake database. These analyses are described in the following sections.

Yield Coefficient Analysis

The seismic yield coefficient, k_y, characterizes the ability of a landslide to resist seismic displacements. In the present study the yield coefficient represents the minimum horizontal earthquake acceleration coefficient necessary to produce a factor of safety equal to one. In a Newmark sliding block analysis, any acceleration greater than the seismic yield acceleration will induce dynamic displacements within the slide mass. The yield coefficient for the Zigzag Sign

landslide was determined using a pseudo-static limit-equilibrium analysis for drained conditions because the real geometry and Mohr-Coulomb failure criterion were already known. An infinite-slope model was used to calculate the yield coefficient for the case of a perched ground water table because the initial stresses were changing and the undrained strength was averaged along the sliding surface.

The Slope/W module in the GeoStudio software suite was employed to determine the drained yield coefficient. The same geotechnical parameters used for the static safety factor analysis were also used in the yield coefficient evaluation for drained conditions. Pore-water pressures were ignored because the analysis was for drained conditions. A trial-and-error approach was employed to adjust the magnitude of the horizontal seismic load acting on the landslide mass until a safety factor equal to one was achieved. The corresponding seismic load associated with a safety factor of one provided the yield coefficient of the slide mass. Because the shear surface of the landslide was already known, the critical slip surface for each trial did not need to be determined. The analysis revealed a yield acceleration of 0.25*g* necessary to achieve a safety factor equal to one for the analyzed landslide in drained conditions. The yield coefficient in drained conditions is therefore 0.25. The constant of the equation of motion was also necessary to calculate dynamic displacements. The general equation of motion provides the relative acceleration of the slide mass:

$$\ddot{s} = C \cdot \left(a - k_y g\right) \tag{3}$$

where $\ddot{s}$ is the relative acceleration of the block, a is the amplitude of the acceleration pulse, g is the acceleration due to gravity, and C is a constant. This equation was modified to calculate the constant in drained conditions (Chugh, 1995):

$$\ddot{s} = \left(a - k_y g\right)\frac{\cos\left(\phi' - \beta\right)}{\cos\phi'} \tag{4}$$

where $\frac{\cos\left(\phi' - \beta\right)}{\cos\phi'}$ represents the constant used to calculate dynamic displacements. In this equation ϕ' represents the effective friction angle and β is the slope inclination. Using ϕ' = 27° and β = 22°, the equation of motion constant in drained conditions is C^d = 0.93.

The yield coefficient of the slide mass for undrained conditions was determined using the undrained shear strength from undrained cyclic triaxial testing on saturated completely decomposed Norwood Tuff. The undrained yield coefficient was calculated according to the following equation developed by Trandafir and Sass (2005) and based on the infinite slope approach:

$$k_y^{\ u} = \left(\frac{\tau_r}{\tau_o} - 1\right)\tan\beta \tag{5}$$

where τ_r represents the undrained shear strength, τ_o represents the driving shear stress, and β represents the slope inclination.

Using a driving shear stress of 20.9 kPa, a shear strength of 25.63 kPa, and a slope inclination of 22°, a yield coefficient of 0.09 was calculated for undrained conditions. The constant of the equation of motion was then calculated using

$$C^u = \cos\beta \tag{6}$$

The undrained constant C^u = 0.93 was calculated using a slope inclination of 22°.

Input Seismic Records

Since no large earthquakes on the Weber Segment of the Wasatch Fault have been yet recorded instrumentally, example earthquakes from around the world were employed to simulate the seismic response of the Zigzag Sign landslide. A search was conducted for normal faulting earthquake records with special consideration for recording stations located on the footwall side. The parameters used to locate records that have similar characteristics to the Weber Segment and the study area included earthquakes with magnitudes ranging from M_0 = 6.7 to 7.7, rupture distance ranging from 0 to 15 km, and rock site conditions similar to NEHRP site class B with V_s30 values ranging from 760 m/s to 1500 m/s. V_s30 values represent the average shear wave velocity expected in

the upper-most 30 meters of the crust. Using these parameters, Dr. Bob Youngs (AMEC Geomatrix) employed NGA empirical ground motion models to determine the expected spectral response for a hypothetical rupture of the Weber Segment.

A search was conducted utilizing the Pacific Earthquake Engineering Research Center (PEER) NGA Database to find event records with similar spectral responses. Six earthquake events, each including fault parallel and fault normal components, were chosen and scaled to match as closely as possible the target spectral acceleration (Figure 3.1). Three earthquake records were from normal-faulting events and three were nonnormal-faulting events. Six seismic wave forms characterized with a wide range of Arias intensities were also selected to correlate Arias intensity values with displacement and earthquake acceleration thresholds associated with large, potentially destructive landslide movements (Trandafir and Sassa, 2005). The unscaled acceleration-time histories for each of these events, plus another six seismic waveforms characterizing various earthquakes throughout the world, were then used to calculate the expected permanent displacements in the Zigzag Sign landslide. An example acceleration-time history is shown in Figure 3.2.

Computed Seismic Displacements

A Newmark sliding block analysis was employed to calculate permanent seismic displacements of the Zigzag Sign landslide under various horizontal input accelerograms. The assumptions for this method are as follows (Newmark, 1965):

1. The slide mass is assumed to be a rigid block resting on an inclined plane with no internal deformation;
2. The slide mass deforms plastically along a single slip surface;
3. Accelerations act in the direction of initial movement at the center of gravity of the slide mass;
4. The slide mass material does not lose strength during shaking.

For the purposes of our study vertical accelerations were ignored and the seismic yield coefficient remained constant during the deformation. When an acceleration exceeds the seismic yield coefficient the slide mass moves relative to the slip plane. The relative acceleration of the block can be calculated using the equation

$$\ddot{s} = \left(a - k_y g\right)\cos\beta \tag{7}$$

where $\ddot{s}$ is the relative acceleration of the block parallel to the slip plane, a is the amplitude of the acceleration pulse, k_y is the yield coefficient, g is the acceleration due to gravity, and β is the inclination of the slope. The displacement of the block during the same duration can be calculated by integrating the relative acceleration twice:

$$\dot{s}\left(t + \Delta t\right) = \dot{s}\left(t\right) + \frac{\ddot{s}\left(t\right) + \ddot{s}\left(t + \Delta t\right)}{2}\Delta t \tag{8}$$

$$s(t+\Delta t) = s(t) + \dot{s}(t)\Delta t + \frac{2\ddot{s}(t) + \ddot{s}(t+\Delta t)}{6}\Delta t^2 \quad (9)$$

The finite-difference based numerical integration scheme characterizing the Newmark sliding block procedure was built into a computer code utilized in dynamic displacement calculations.

The program required five input parameters to calculate the permanent dynamic displacement for an earthquake event. These included, in order, the yield coefficient, the equation of motion constant, the duration of the seismic record, the time interval of the seismic record, and the scaling factor. This approach does not account for expected changes in duration and frequency content with amplitude. Each acceleration-time history was scaled to various values of the peak earthquake acceleration within 0.1 – 1.0*g* using 0.1*g* increments. Each event was used to calculate dynamic displacements for drained and undrained conditions using both positive acceleration factors and negative acceleration factors. The analysis thus involved over 800 permanent dynamic displacements representative of the dynamic response of the Zigzag Sign landslide in completely decomposed Norwood Tuff. The dynamic displacement progression produced for an example calculation is shown in Figure 3.3.

Peak Ground Acceleration Threshold Methodology

With the dynamic displacements calculated, it was necessary to determine the critical peak ground acceleration required for producing potentially damaging

dynamic displacements in a landslide comprised of Norwood Tuff. For each earthquake event, the peak acceleration coefficient of the scaled record (k_m) was plotted against the corresponding calculated permanent displacement (s_p) on a logarithmic scale (Figure 3.4). Such a plot allows us to distinguish between peak earthquake accelerations associated with relatively small permanent displacements and peak earthquake acceleration values that may trigger large, potentially damaging slope movements. The intersection between the tangent to the asymptotic portion of the s_p-k_m curve and the horizontal axis provides the peak ground acceleration threshold ($k_m^c g$) for earthquake-induced large, potentially damaging displacements. Peak acceleration values greater than the peak earthquake acceleration threshold were considered unsafe because the s_p-k_m curve increased asymptotically, thus indicating a potential for large damaging landslide displacements for very small changes in the peak earthquake acceleration beyond this threshold.

The relationship between the critical peak ground acceleration threshold and the amount of energy released by the earthquake was subsequently analyzed. The Arias intensity parameter was selected as a measure of the amount of energy released by each event in this study. The Arias intensity parameter represents the total energy per unit weight absorbed by an idealized set of oscillators during an earthquake event (Arias, 1970). This parameter incorporates the amplitude and duration of the ground motion, as well as all frequencies of the recorded motion. The following equation was used to calculate the Arias intensity for each earthquake record:

$$I_a = \frac{\pi}{2g}\int_0^{t_s} a(t)^2\,dt \tag{10}$$

where I_a is the Arias intensity and t_s is the duration of the earthquake record. The calculation is the sum of the squared acceleration values from a time-acceleration history and the units are $\frac{m}{s}$.

The Arias intensity values were then normalized using the peak earthquake acceleration of the seismic records in order to obtain a unique parameter characterizing a specific seismic record, independent of the scaling factors used in the analysis

$$\bar{I}_A = \frac{I_A}{(a^2_{\max})} \tag{11}$$

where I_A represents the Arias intensity calculated for a specific earthquake accelerogram, *a(t)*, characterized by a peak earthquake acceleration $a_{\max} = k_m g$ and a duration t_s.

The units for the normalized Arias intensity are $\frac{s^3}{m}$. The six seismic waveforms were scaled using a maximum acceleration of 0.9*g* while the six earthquake records from the PEER database were scaled using a maximum acceleration of 0.53*g*. The normalized Arias intensity values were calculated for

the positive and negative orientations of each time-acceleration history and used to associate the earthquake energy released with the critical peak ground acceleration (Table 3.1, Table 3.2). For the analyzed input earthquakes, $\bar{I}_A$ varied from 1.83 to 63.15 $\frac{s^3}{m}$.

Peak Ground Acceleration Threshold Results

For dry conditions the threshold peak earthquake acceleration used in the dynamic displacement analysis ranged from 0.55*g* to 0.70*g*. The average value of the peak earthquake acceleration threshold for a dry slope comprised of Norwood Tuff is 0.63*g*, with a standard deviation equal to 0.04*g* (Figure 3.5).

The threshold peak earthquake acceleration necessary to trigger large, potentially damaging landslide displacements for undrained conditions varied between 0.47 and 0.61*g*. The peak earthquake acceleration coefficient required to trigger damaging displacements for undrained conditions is lower than that of a dry slope and has an average of 0.53*g*, with a standard deviation of 0.03*g* (Figure 3.6).

The difference between computed permanent undrained (s_u) and drained (s_d) landslide displacements was subsequently analyzed. The displacement difference (s_u-s_d) was determined for each seismic waveform scaled to a peak ground acceleration of 0.26*g*, representing the peak ground acceleration expected for Zigzag Sign landslide based on Next Generation Attenuation models. The difference of these values was analyzed in relation with normalized Arias intensity as shown in Figure 3.7. For the selected normal-faulting

earthquake records matching the design response spectrum characterizing the Weber segment of the Wasatch Fault and associated with normalized Arias intensity values within 11.27 – 23.93 $\frac{s^3}{m}$, the computed permanent displacement difference (s_u-s_d) ranges from 4 – 13 cm.

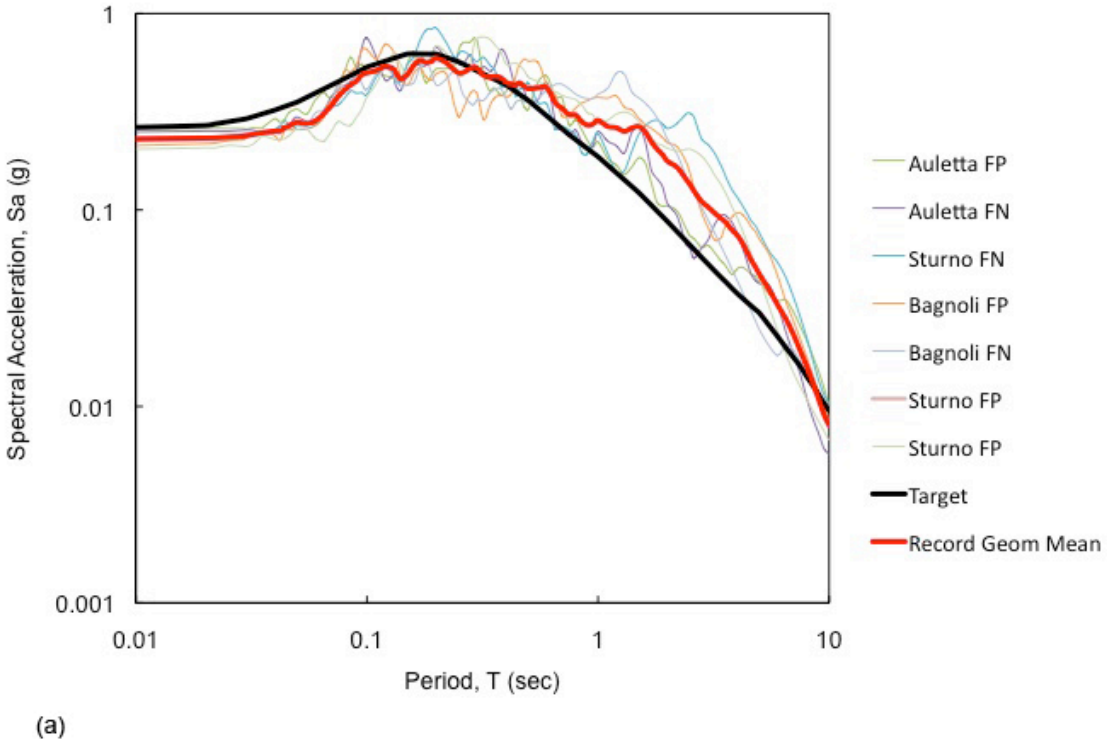

Figure 3.1. Target and record geometric mean spectral accelerations generated by input parameters similar to those expected for the Weber Segment of the Wasatch Fault Zone: **a.** Scaled spectral responses for normal-faulting records, **b.** Scaled spectral responses for nonnormal-faulting records.

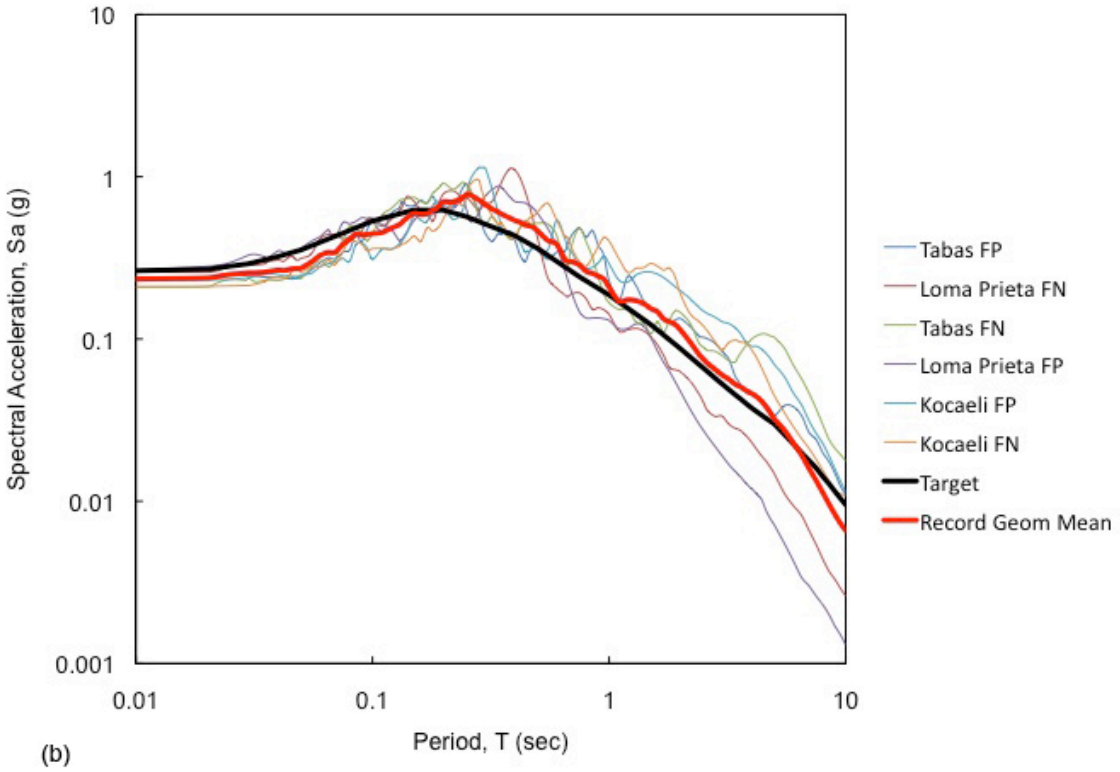

Figure 3.1 continued

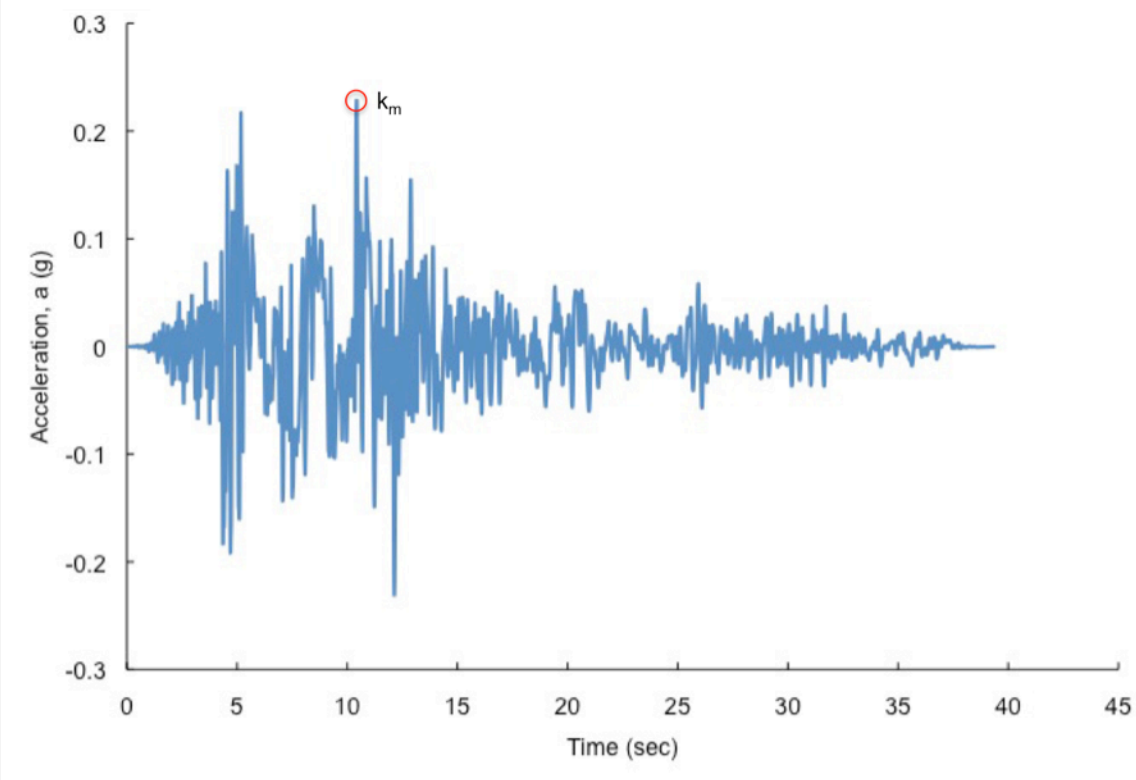

Figure 3.2. Example unscaled input horizontal ground motion generated at the Sturno, Italy station by the M6.9 1980 Irpinia, Italy earthquake (k_m = 0.26g).

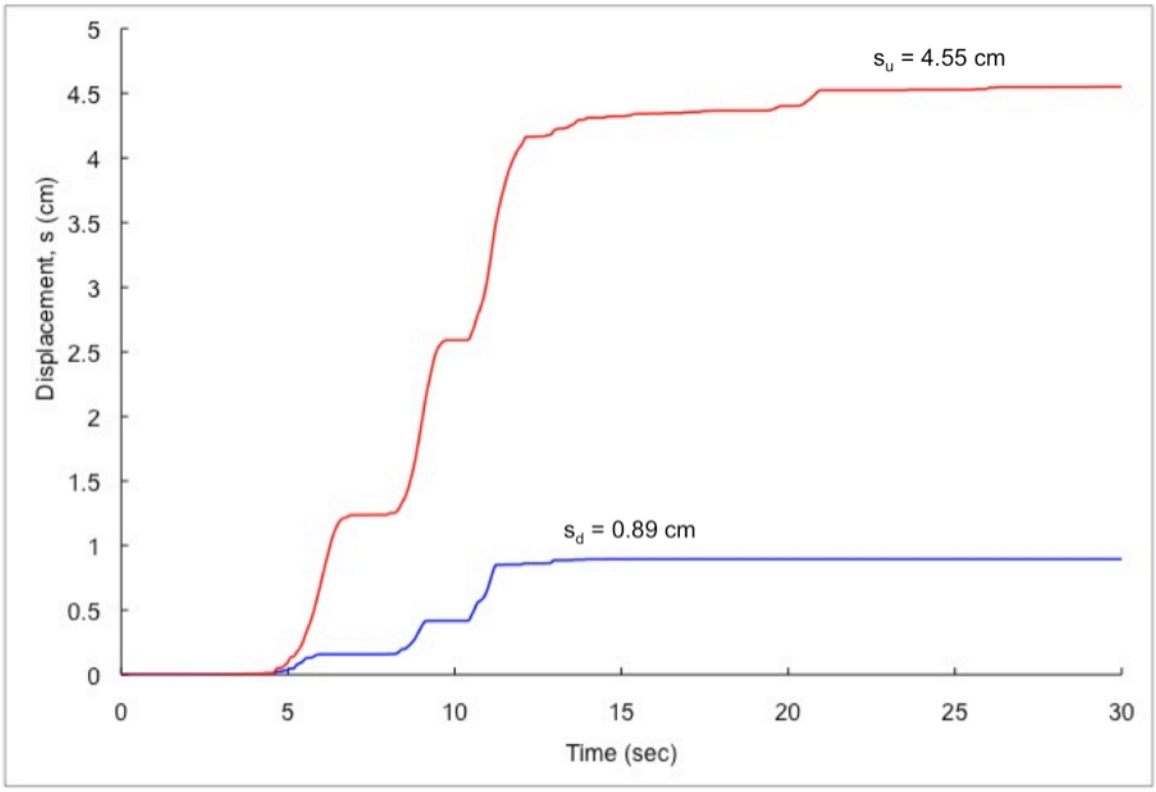

Figure 3.3. Example horizontal displacement progression in Norwood Tuff material for drained (s_d) and undrained (s_u) conditions based on positive accelerations generated by the 1980 M6.9 Irpinia, Italy earthquake recorded at Sturno, Italy (k_m = 0.26g).

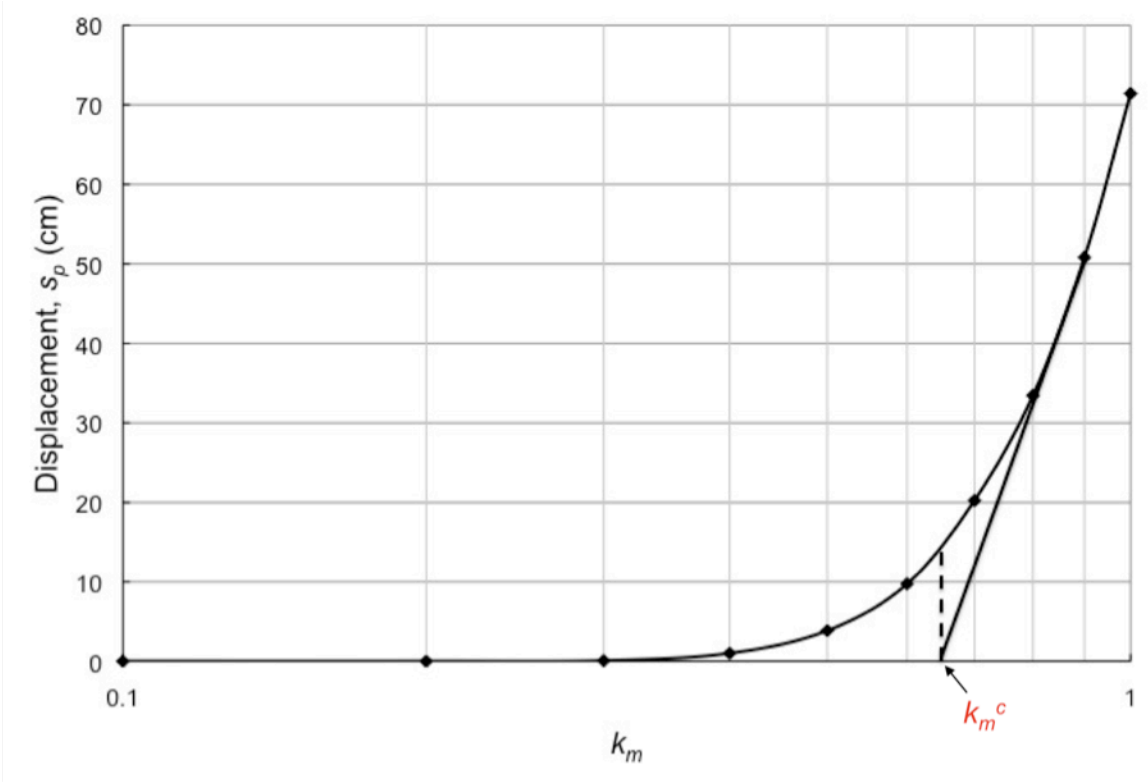

Figure 3.4. Method for determining the peak acceleration threshold and associated permanent displacement in Norwood Tuff material for an individual earthquake record.

Table 3.1: Normalized Arias Intensities for the positive orientation of each input acceleration-time history.

Earthquake	Date	Earthquake Magnitude (M_w)	Style of Faulting	Component	Normalized Arias Intensity (m/s)
Gilroy	5/14/02	4.9	Reverse -Oblique	67	5.03
Gilroy	5/14/02	4.9	Reverse -Oblique	157	4.38
Kobe, Japan	1/17/95	6.9	Reverse	270	10.49
Chuetsu, Japan	10/23/04	6.9	Reverse	180	17.21
Taiwan	9/20/99	7.6	Reverse	270	63.15
Loma Prieta, USA	10/18/89	6.93	Reverse -Oblique	63	15.91
Loma Prieta, USA	10/18/89	6.93	Reverse -Oblique	153	14.08
Chuetsu, Japan	10/23/04	6.9	Reverse	270	13.01
El Salvador	1/13/01	7.6	Reverse -Oblique	180	52.4
Taiwan	9/20/99	7.6	Reverse	180	21.78
Sturno, Italy	11/23/80	6.9	Normal	0	17.41
Sturno, Italy	11/23/80	6.9	Normal	270	16.58
Bagnoli, Italy	11/23/80	6.9	Normal	0	14.42
Bagnoli, Italy	11/23/80	6.9	Normal	270	21.96
Auletta, Italy	11/23/80	6.9	Normal	0	23.93
Auletta, Italy	11/23/80	6.9	Normal	270	11.27
Tabas, Iran	9/16/78	7.35	Reverse	270	19.3
Tabas, Iran	9/16/78	7.35	Reverse	0	16
Kocaeli, Turkey	8/17/99	7.51	Strike-Slip	90	24.21
Kocaeli, Turkey	8/17/99	7.51	Strike-Slip	180	20.94

Table 3.2: Normalized Arias Intensities for the negative orientation of each input acceleration-time history.

Earthquake	Date	Earthquake Magnitude (Mw)	Style of Faulting	Component	Normalized Arias Intensity (m/s)
Gilroy, USA	5/14/02	4.9	Reverse-Oblique	67	1.83
Gilroy, USA	5/14/02	4.9	Reverse-Oblique	157	2.2
Kobe, Japan	1/17/95	6.9	Reverse	270	11.47
Chuetsu, Japan	10/23/04	6.9	Reverse	180	12.03
Taiwan	9/20/99	7.6	Reverse	270	12.36
Loma Prieta, USA	10/18/89	6.93	Reverse-Oblique	63	13.39
Loma Prieta, USA	10/18/89	6.93	Reverse-Oblique	153	17.21
Chuetsu, Japan	10/23/04	6.9	Reverse	270	21.78
El Salvador	1/13/01	7.6	Reverse-Oblique	180	63.15
Taiwan	9/20/99	7.6	Reverse	180	52.4
Sturno, Italy	11/23/80	6.9	Normal	0	17.04
Sturno, Italy	11/23/80	6.9	Normal	270	18.52
Bagnoli, Italy	11/23/80	6.9	Normal	0	11.82
Bagnoli, Italy	11/23/80	6.9	Normal	270	18.09
Auletta, Italy	11/23/80	6.9	Normal	0	16.05
Auletta, Italy	11/23/80	6.9	Normal	270	18.85
Tabas, Iran	9/16/78	7.35	Reverse	270	22.1
Tabas, Iran	9/16/78	7.35	Reverse	0	17.41
Kocaeli, Turkey	8/17/99	7.51	Strike-Slip	90	25.92
Kocaeli, Turkey	8/17/99	7.51	Strike-Slip	180	16.83

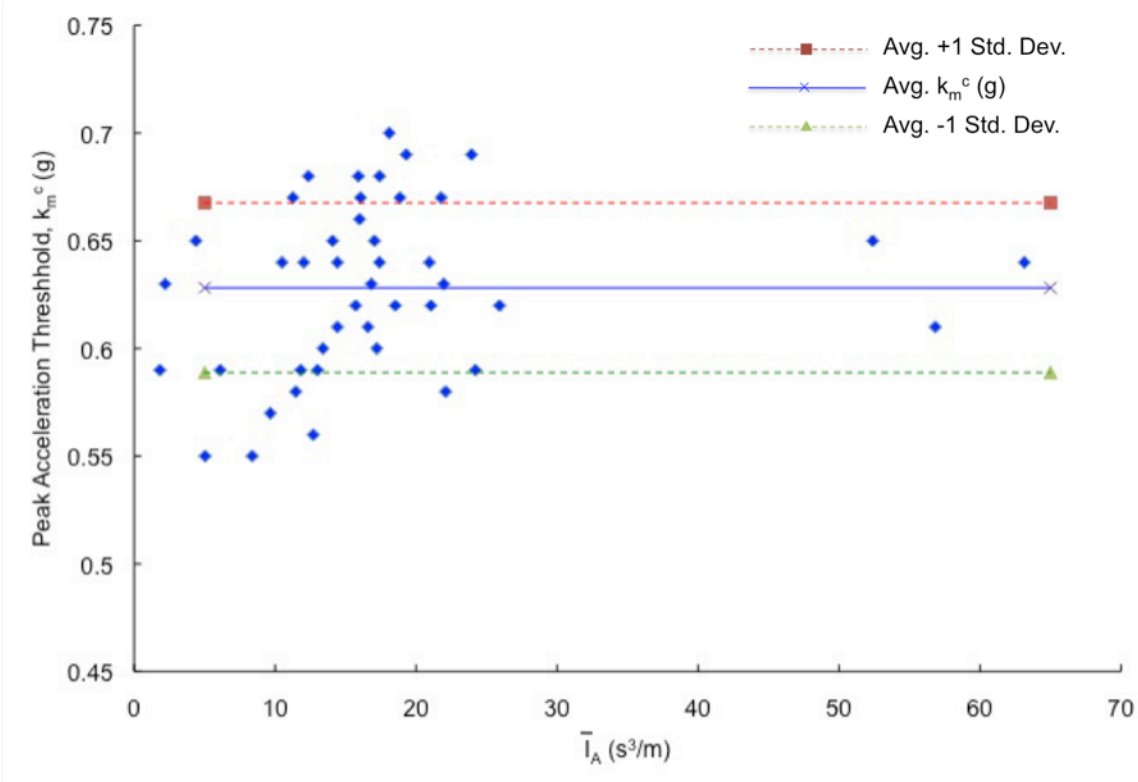

Figure 3.5. Coefficient of peak earthquake acceleration required to trigger large landslide movements in relation to Arias intensity for the case of a dry slope.

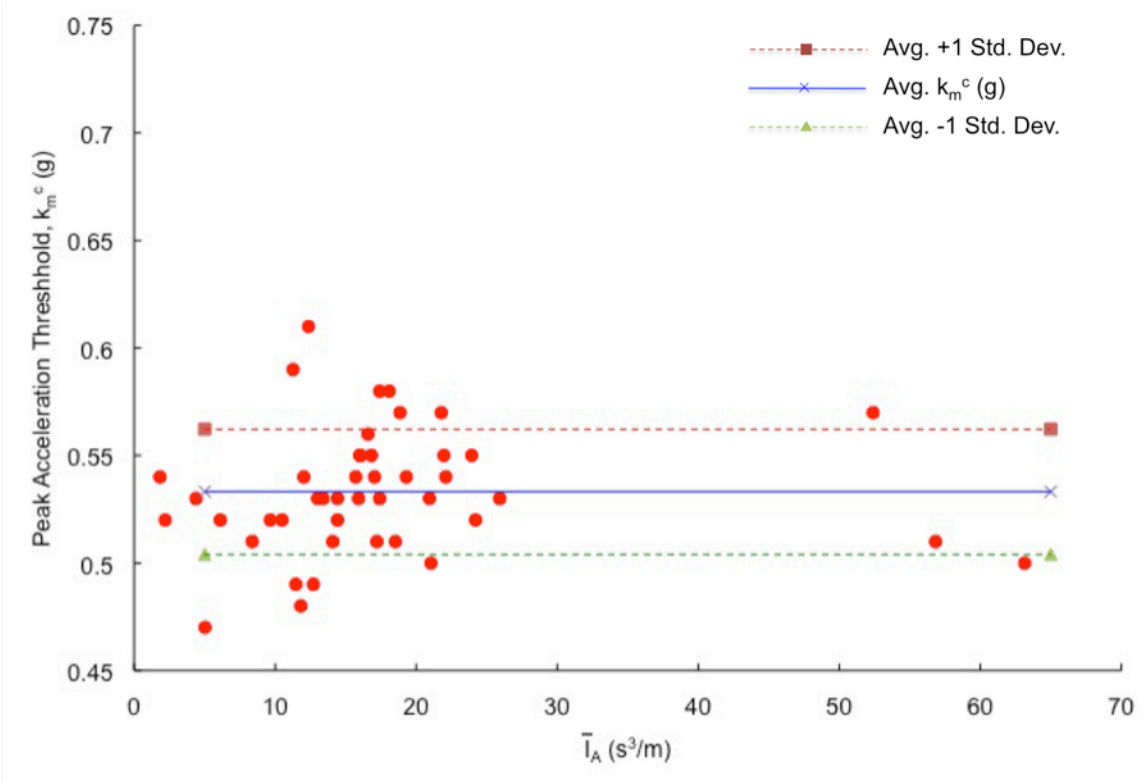

Figure 3.6. Coefficient of peak earthquake acceleration required to trigger large landslide movements in relation to Arias intensity for the case of a perched water table above the sliding surface.

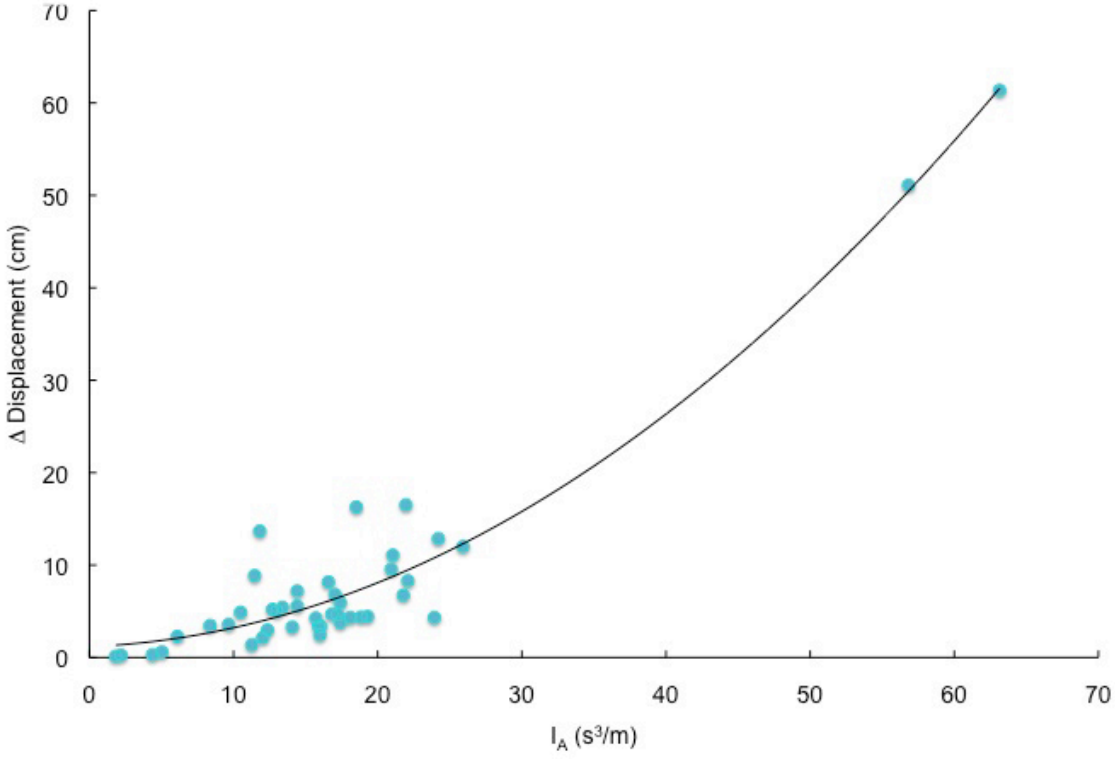

Figure 3.7. Displacement difference between drained and undrained conditions in relation to normalized Arias Intensity for each seismic waveform scaled to a peak ground acceleration of 0.26*g*.

CONCLUSIONS

Results of the dynamic displacement analysis indicate that for a given earthquake event, a greater peak earthquake acceleration is necessary to trigger displacements in unsaturated shallow landslides in completely decomposed Norwood Tuff compared to the case of a saturated slide mass. The critical peak ground acceleration was not dependent on the energy of the earthquake. Peak acceleration values greater than 0.55*g* can potentially trigger large displacements in shallow landslides in dry completely decomposed Norwood Tuff. Saturated slopes, or slopes with perched ground water tables located in completely decomposed Norwood Tuff will experience dynamic displacements with lower peak ground accelerations relative to dry slopes. Peak acceleration values greater than 0.47*g* can potentially trigger large displacements in partially saturated slopes or slopes with perched water tables.

The critical coefficient of peak ground acceleration was not dependent on the energy of the earthquake. The energy released by the earthquake does though affect the difference between computed permanent undrained (s_u) and drained (s_d) landslide displacements. There is a nonlinear increase in the permanent displacement difference (s_u-s_d) with increasing normalized Arias intensity. The potential for large, potentially damaging displacements therefore

increases in undrained conditions, relative to dry conditions, as the amount of energy released by the earthquake increases. Regardless of the amount of energy released, earthquakes that occur in relatively wet months associated with increased pore-water pressures are expected to trigger larger displacements than events that occur in dry months. This conclusion is significant for the study area because seasonal fluctuations in pore-water pressure are an important aspect of slope stability in northern Utah and the timing of an earthquake could have a great effect on the potential for large, damaging displacements for landslides in Norwood Tuff. Slopes are more susceptible to large dynamic displacements in the spring and early summer months when precipitation and snow melt occur. Slopes are less susceptible to potentially damaging dynamic displacements when water levels decrease during late summer, fall, and winter months.

APPENDIX A

UNSCALED INPUT ACCELEROGRAMS

Appendix A includes each unscaled input accelerogram used for the dynamic displacement analysis of completely decomposed Norwood Tuff. Normal and non normal-faulting accelerograms were located on the PEER online database and provided by Dr. Bob Youngs. The input accelerograms were selected by matching as closely as possible the scaled spectral response with the expected spectral response of an earthquake on the Weber Segment of the WFZ. The seismic wave forms were selected to correlate Arias intensity values with displacement and earthquake acceleration thresholds associated with large, potentially destructive landslide movements (Trandafir and Sassa, 2005).

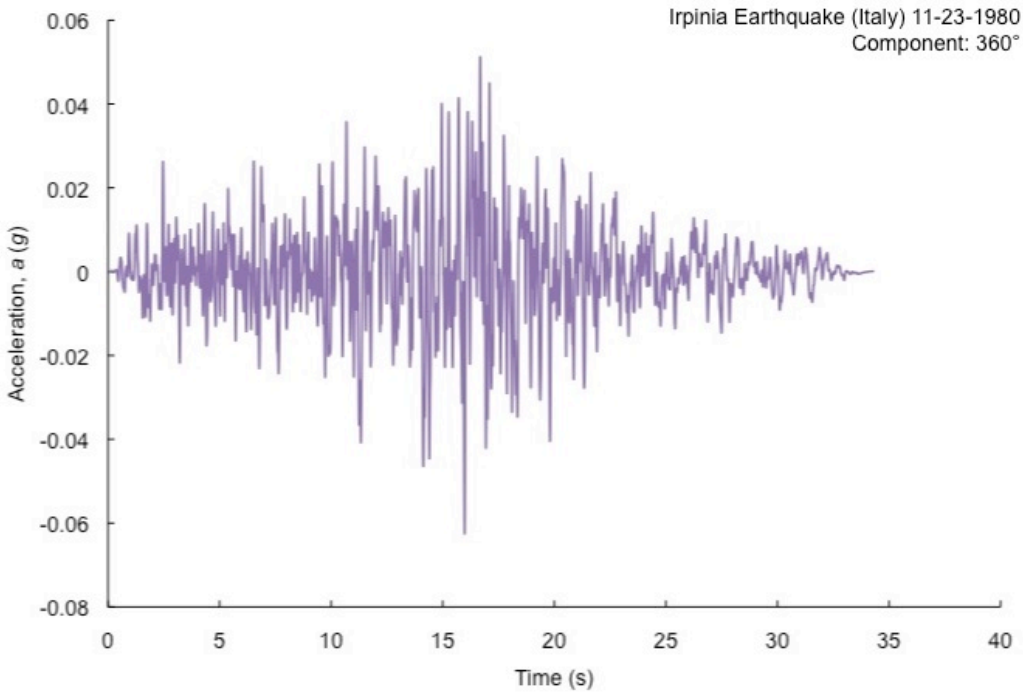

Figure A.1. Normal-faulting accelerograms.

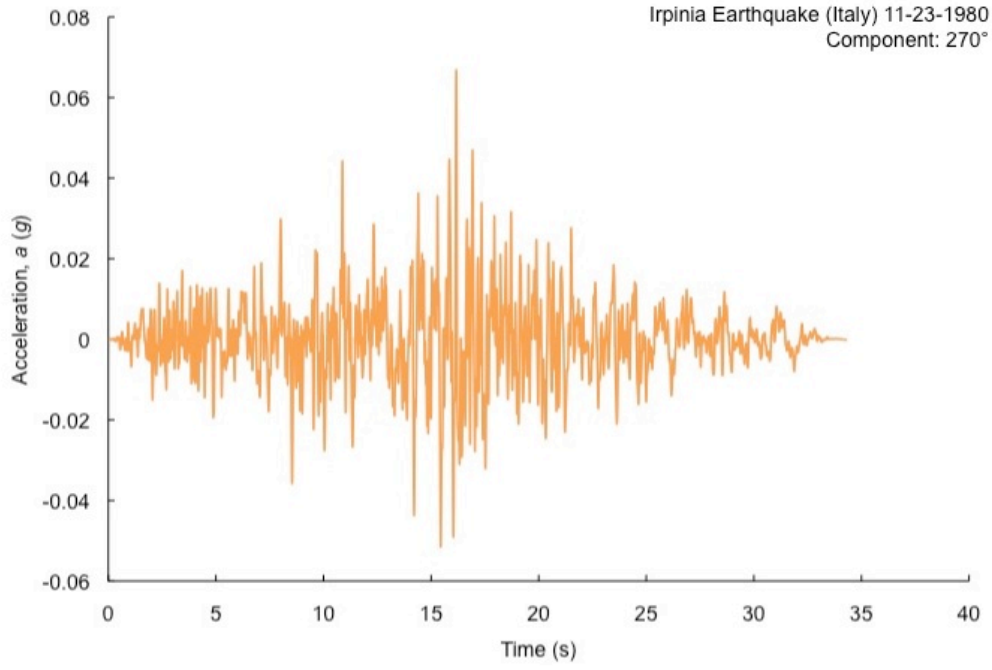

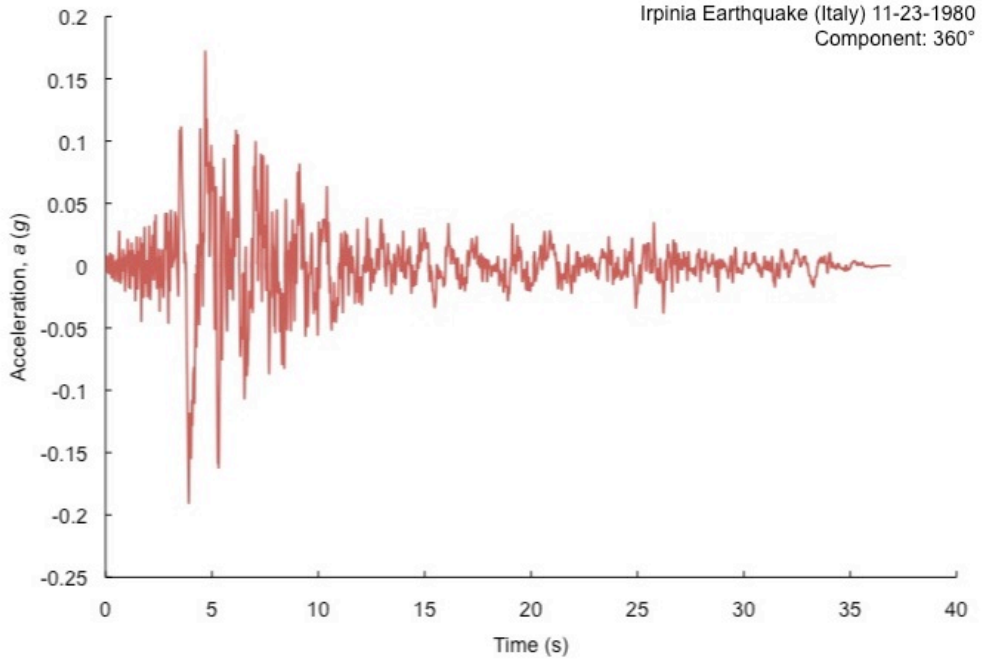

Figure A.1 continued

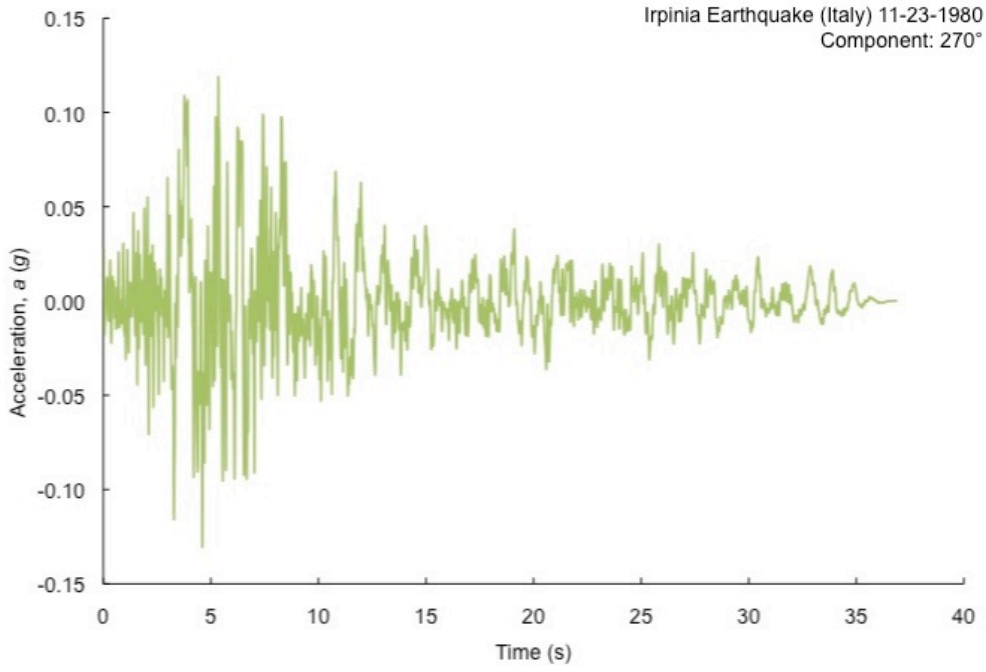

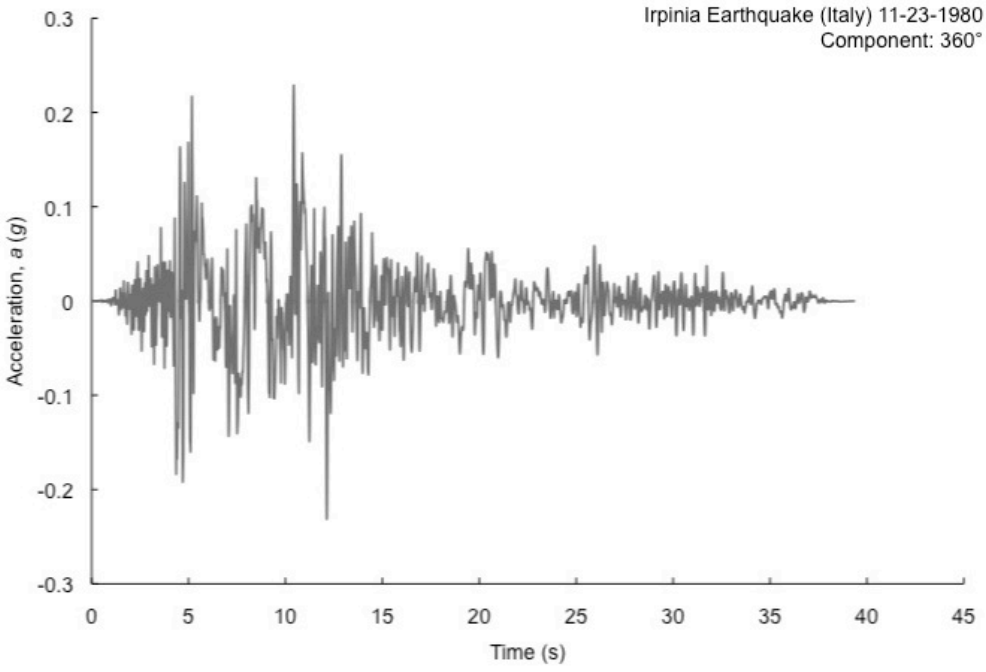

Figure A.1 continued

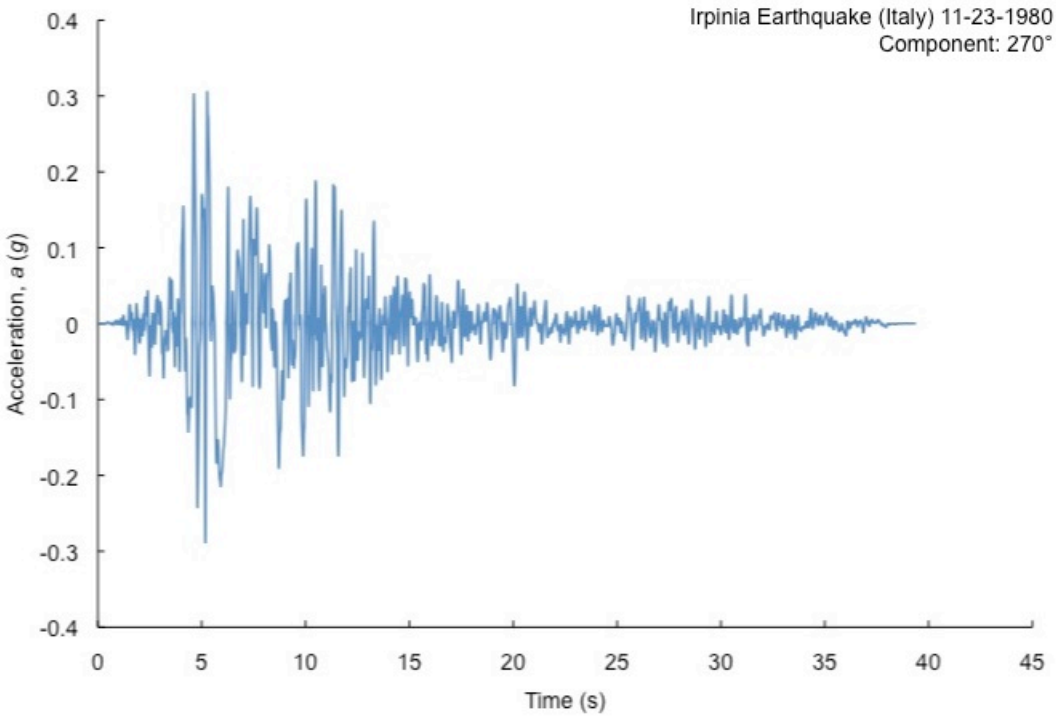

Figure A.1 continued

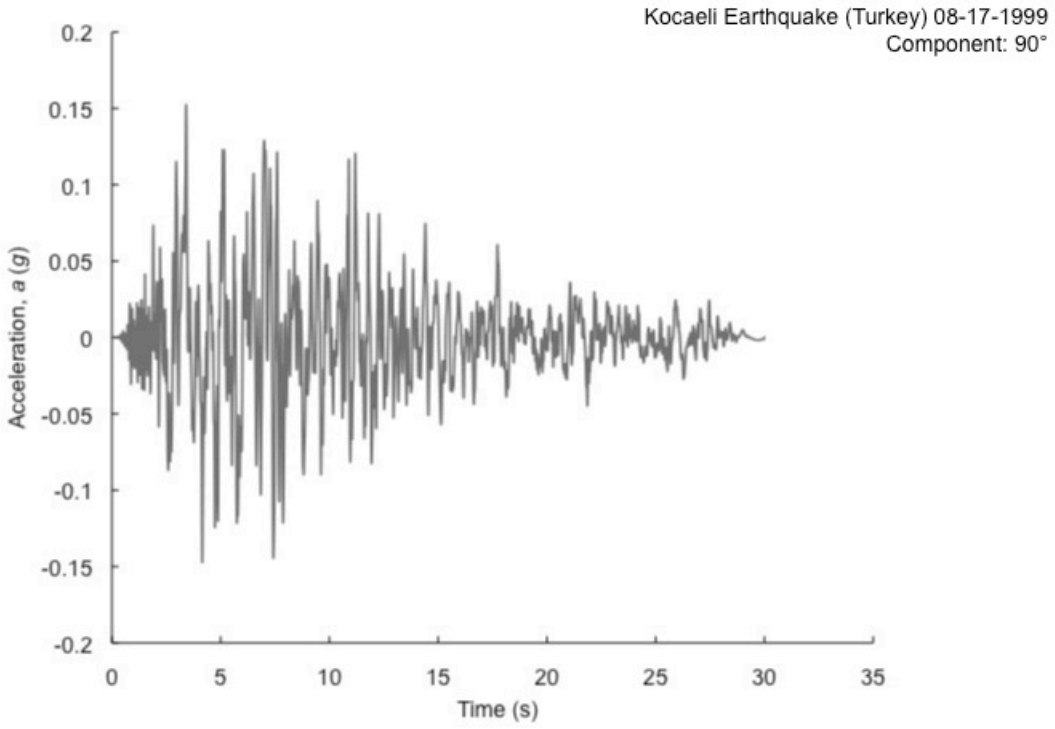

Figure A.2. Nonnormal-Faulting accelerograms.

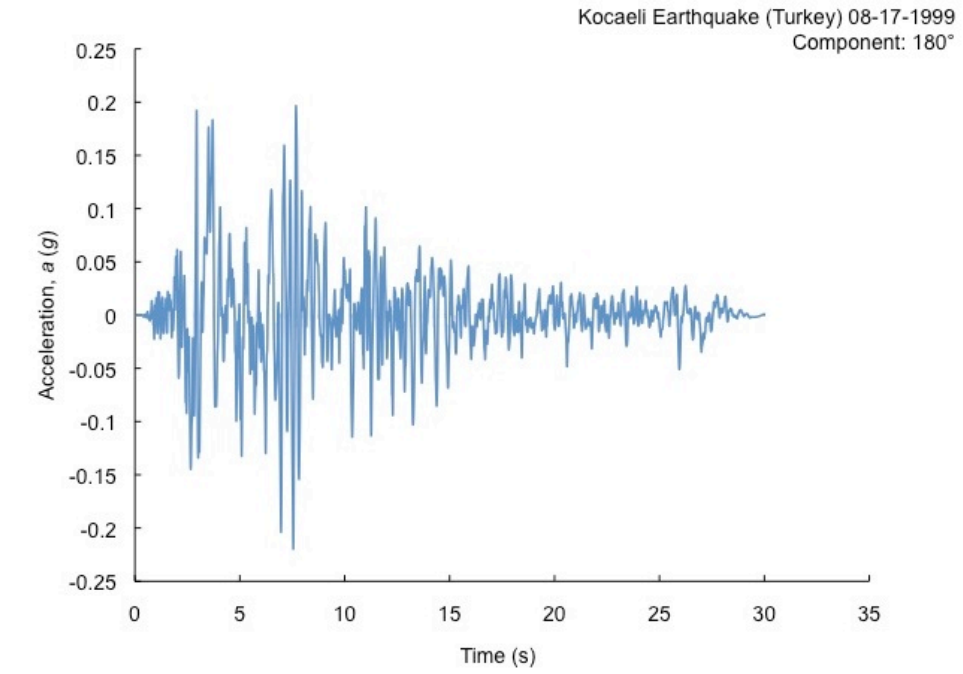

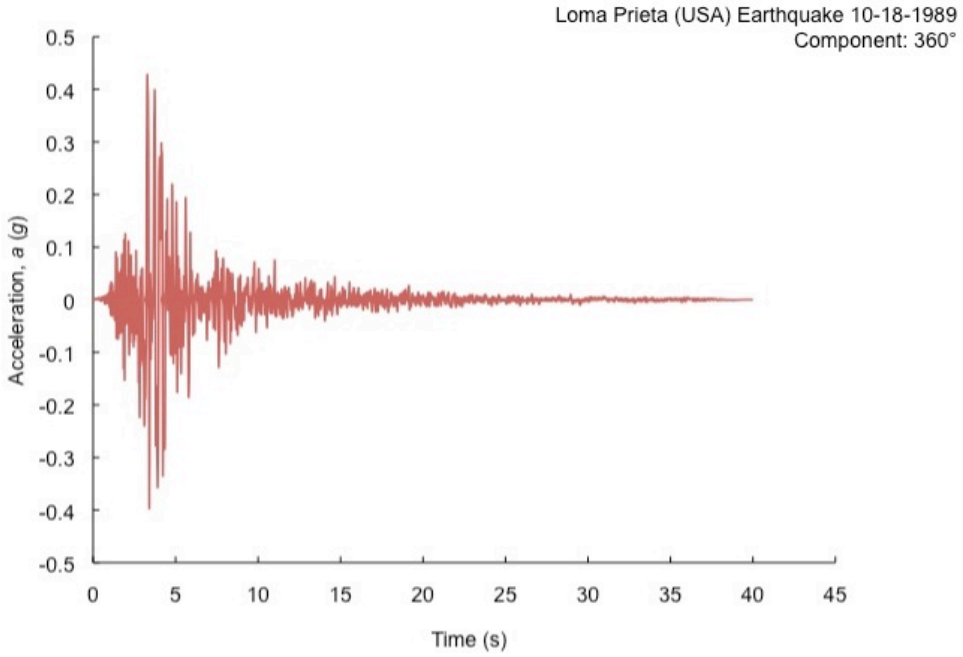

Figure A.2 continued

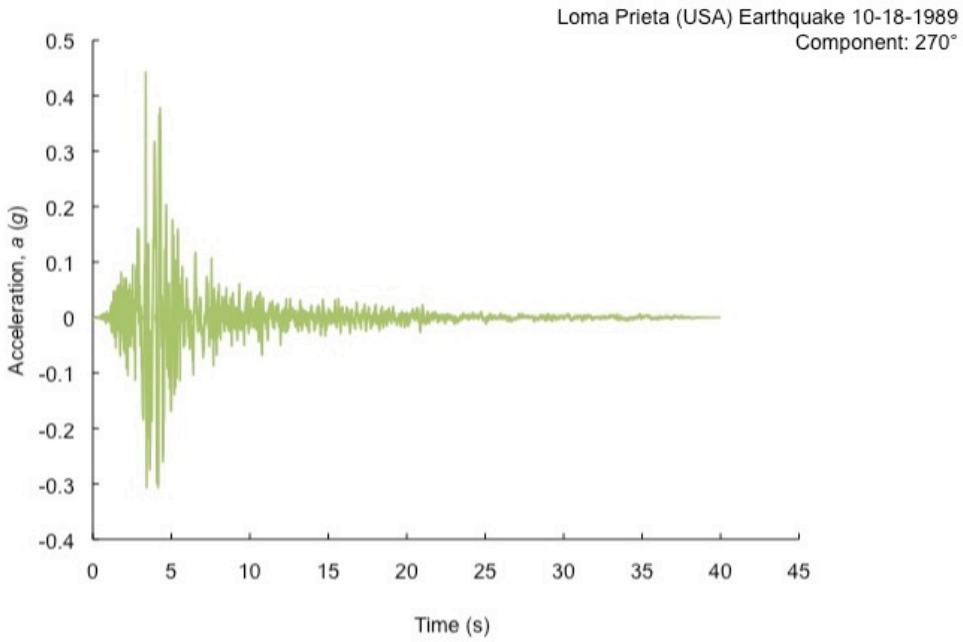

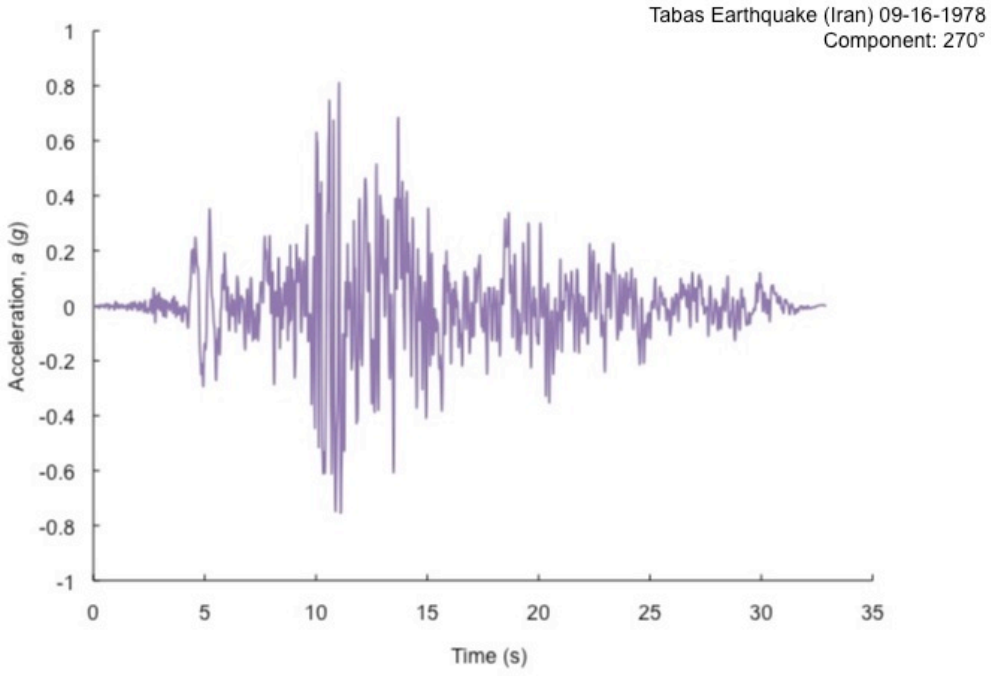

Figure A.2 continued

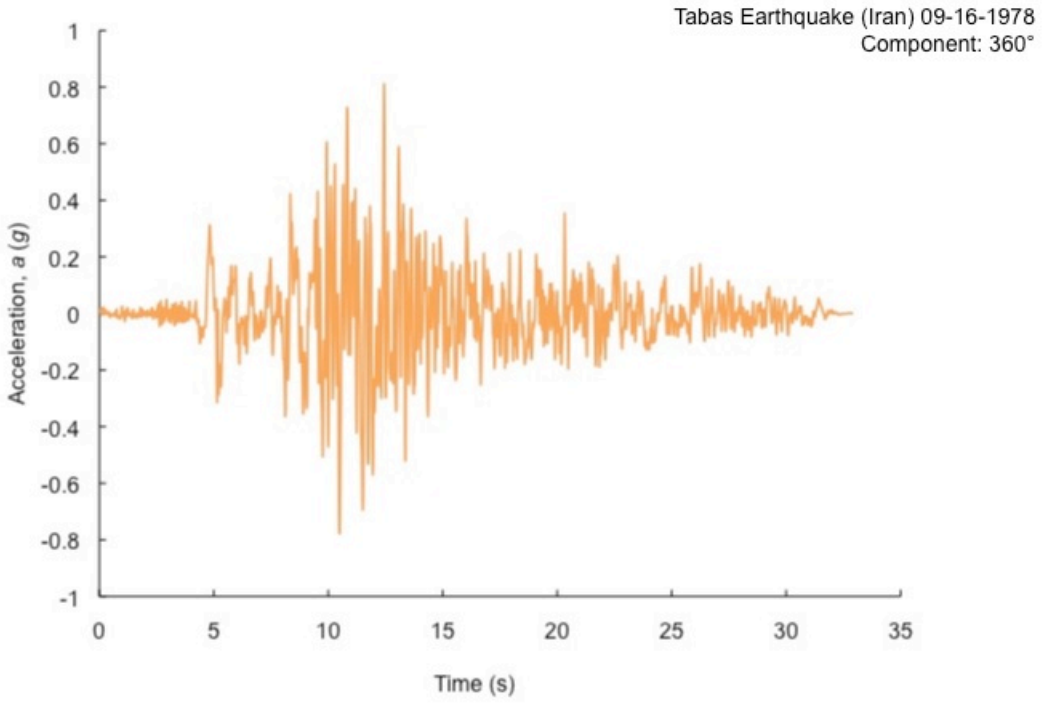

Figure A.2 continued

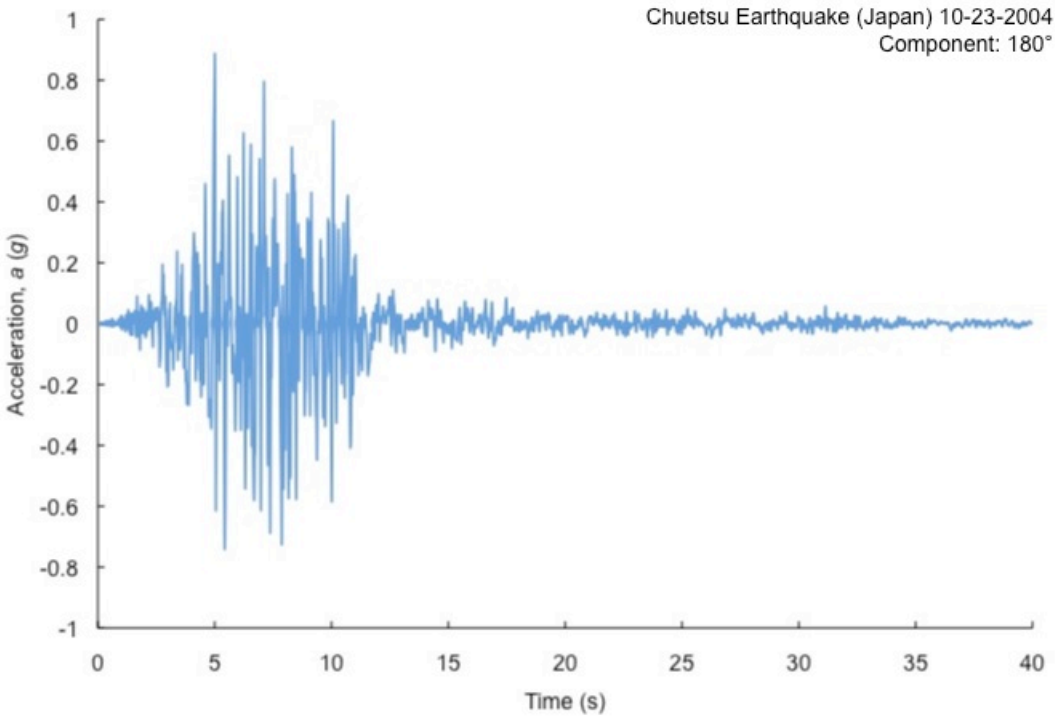

Figure A.3. Seismic waveforms.

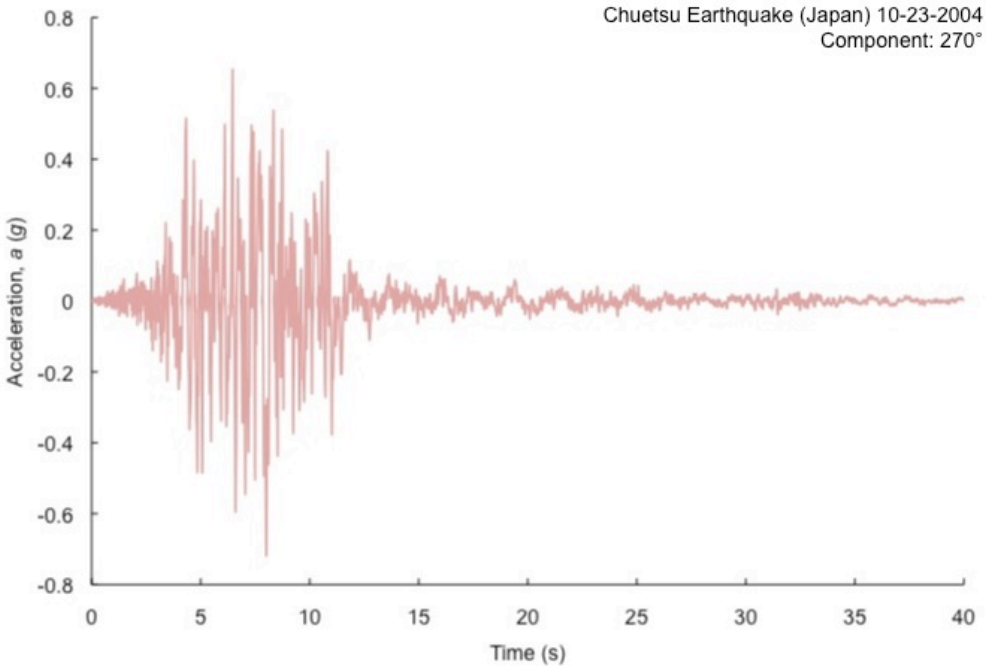

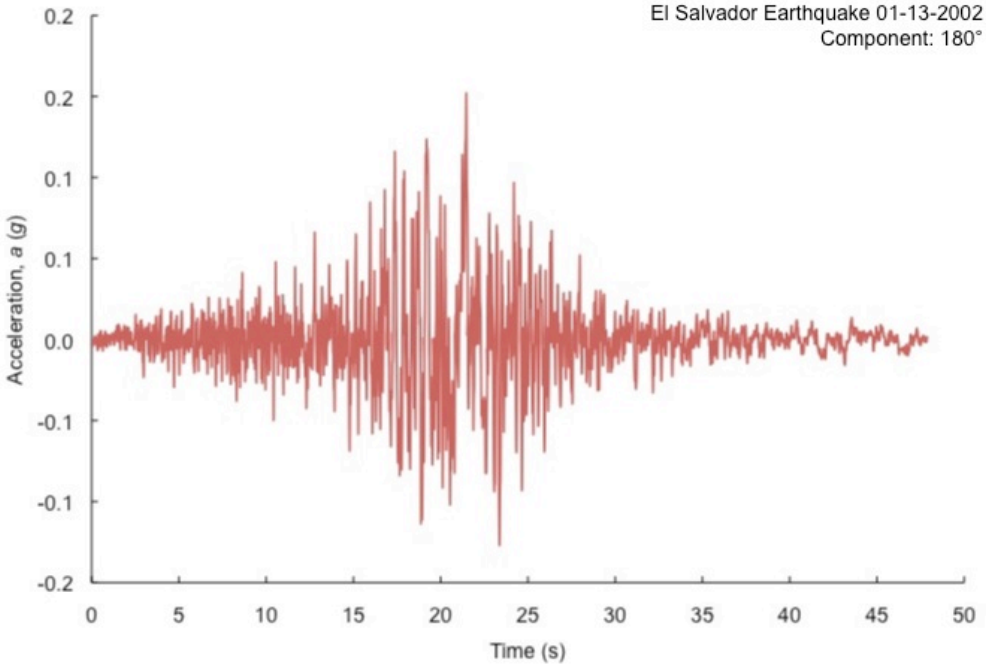

Figure A.3 continued

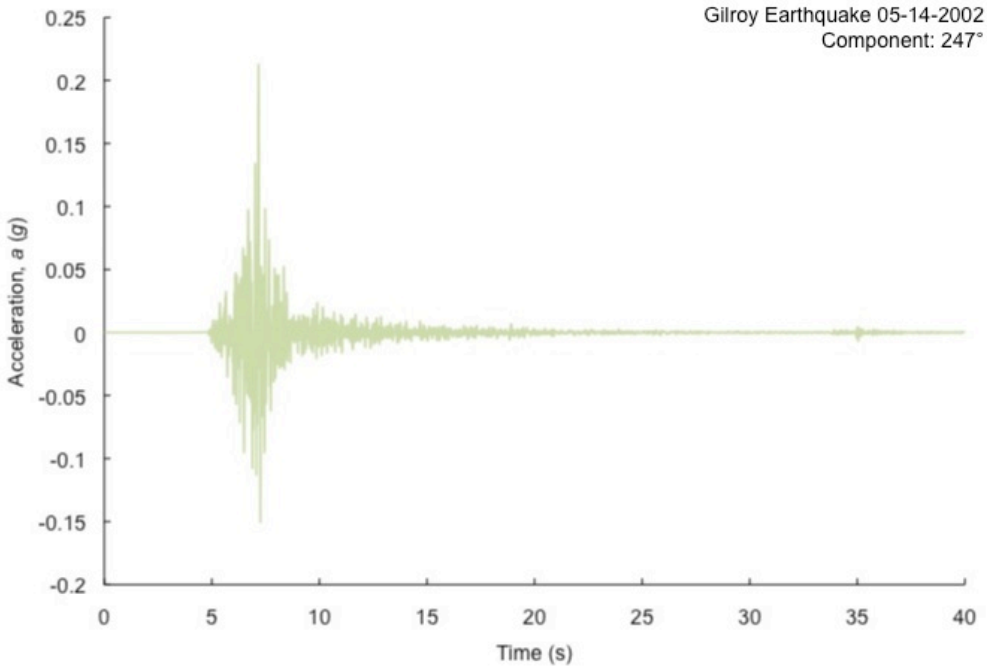

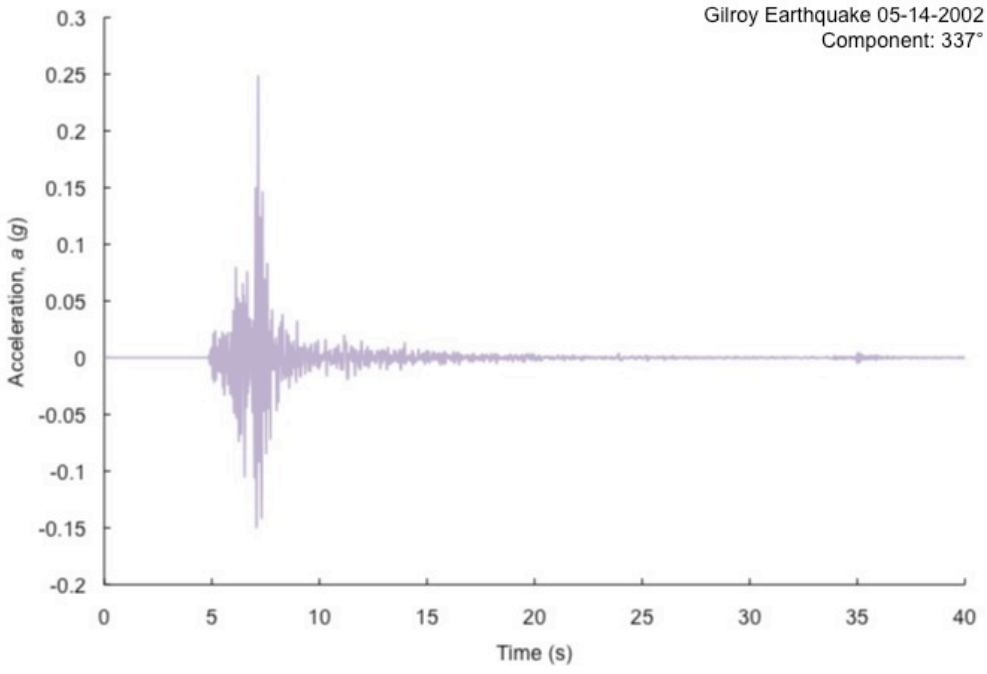

Figure A.3 continued

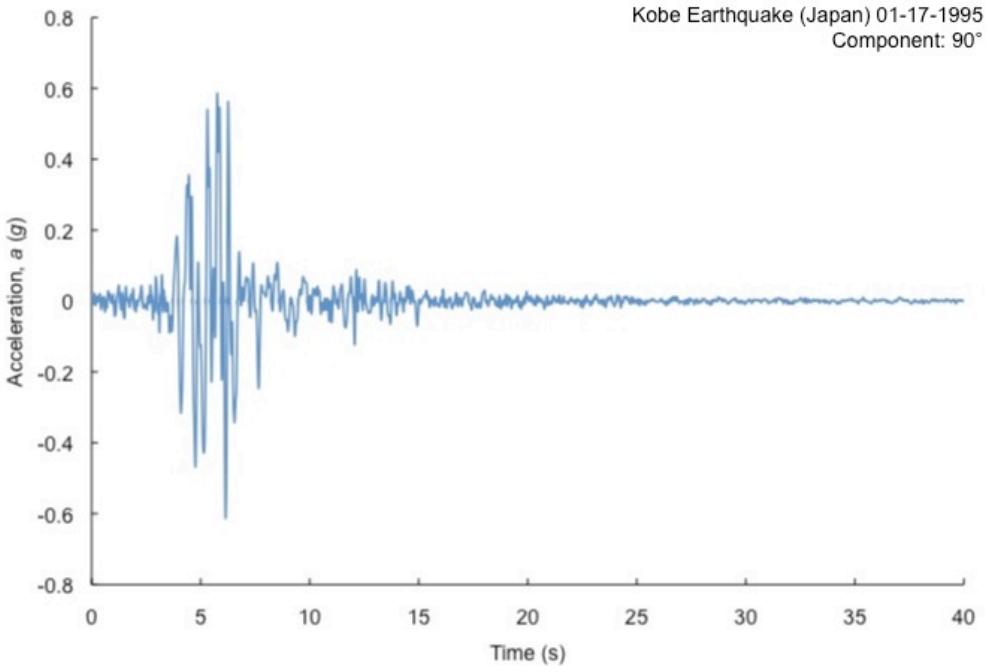

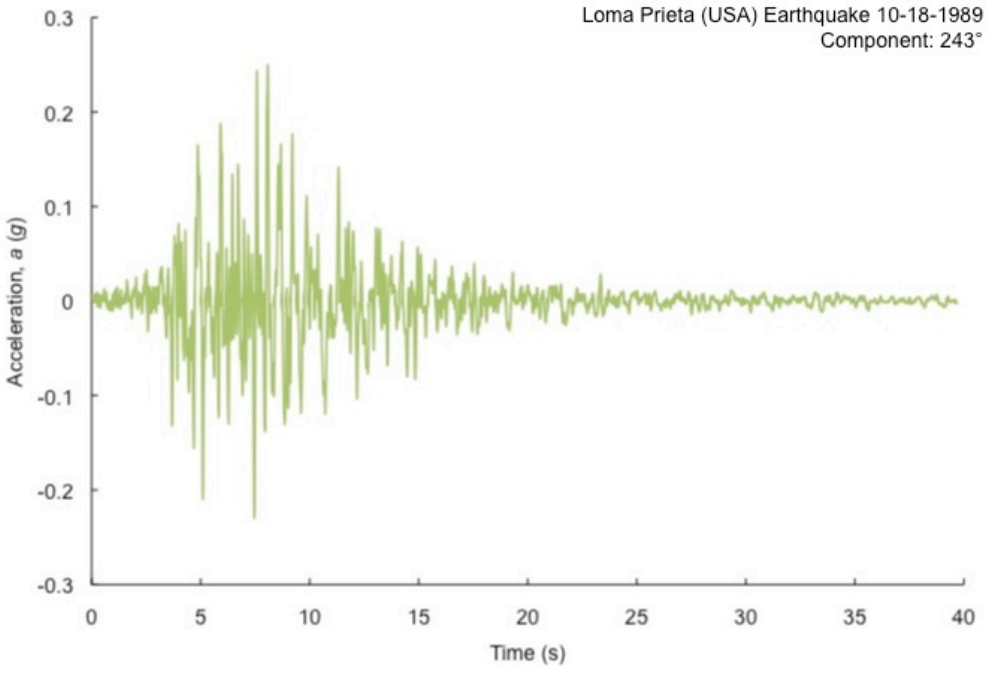

Figure A.3 continued

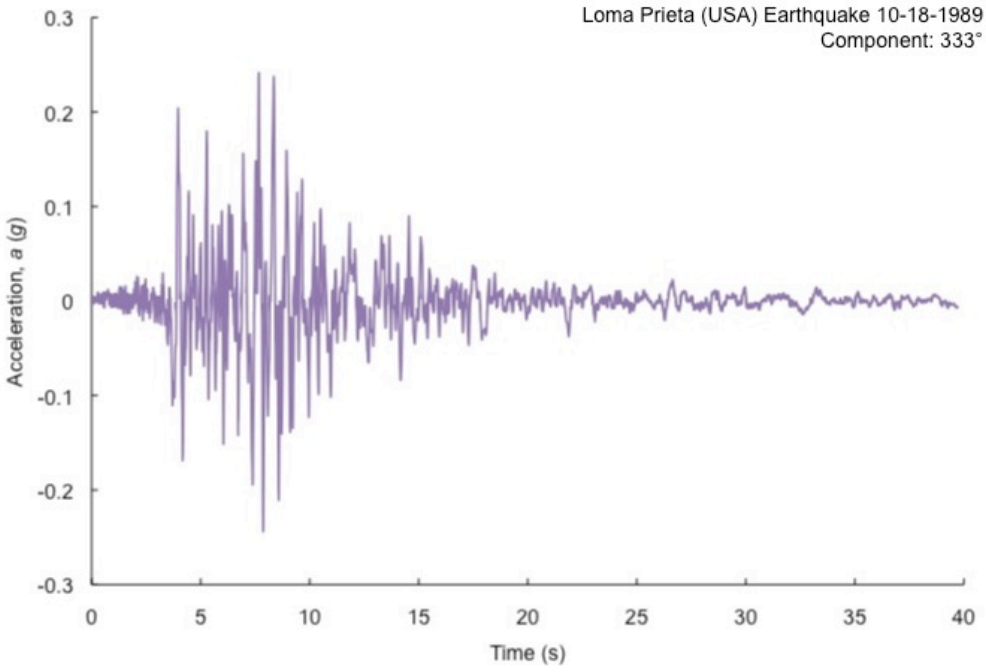

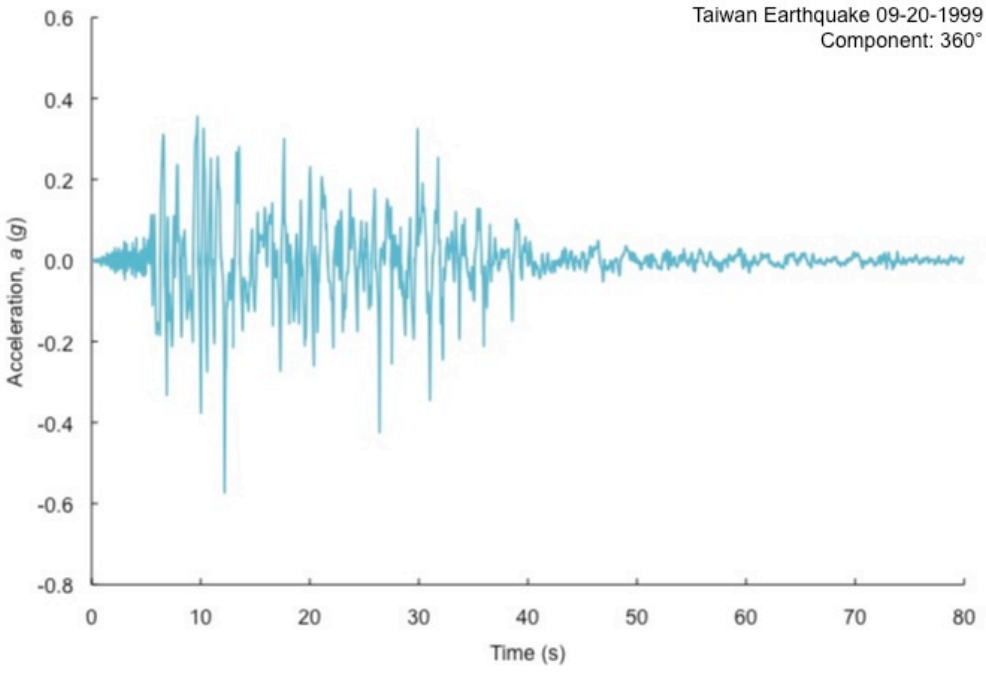

Figure A.3 continued

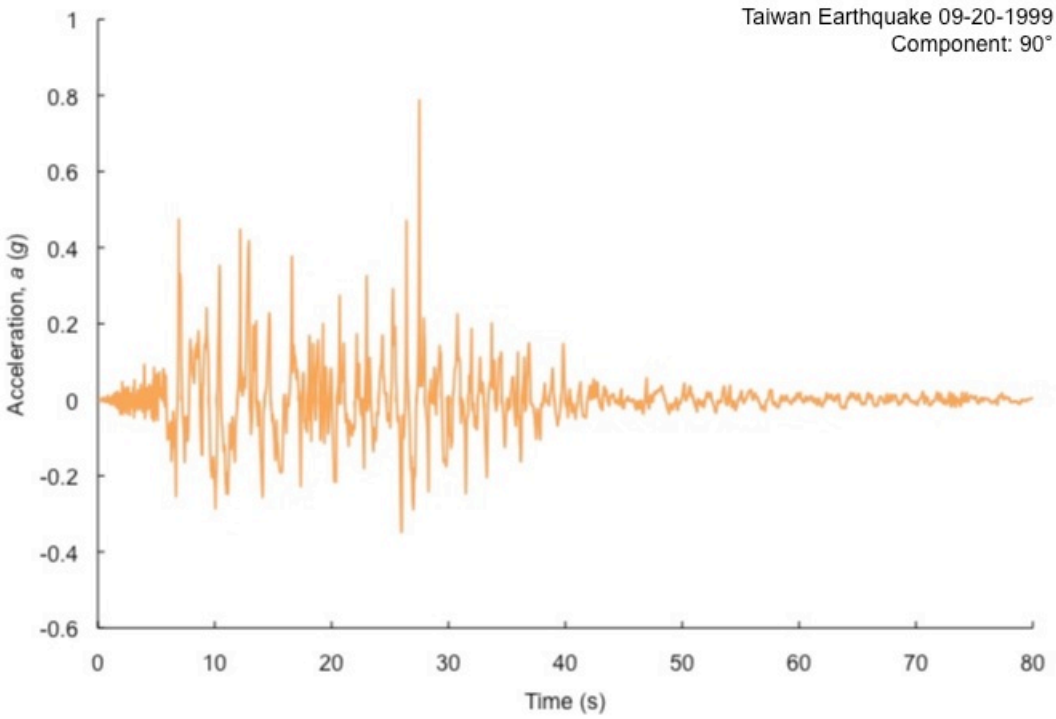

Figure A.3 continued

APPENDIX B

METHODOLOGY FOR DETERMINING THE CRITICAL COEFFICIENT FOR PEAK GROUND ACCELERATION

Appendix B includes plots used to determine the critical coefficient for peak ground acceleration to potentially trigger damaging seismic displacements in slopes comprised of completely decomposed Norwood Tuff. Each plot shows the relationship between the coefficients for peak ground acceleration (k_m) on a log scale and their corresponding calculated permanent displacements for each seismic record. Plots were produced for dry and partially saturated conditions, as well as the positive and negative orientation of each accelerogram.

The intersection between the tangent to the asymptotic portion of the s_p-k_m curve and the horizontal axis provides the peak ground acceleration threshold (k_m^c, g) for earthquake-induced large, potentially damaging displacements. Peak acceleration values greater than this threshold may be considered unsafe due to an asymptotic increase in permanent seismic displacements with increasing k_m.

Normal-Faulting Earthquakes in Dry Conditions

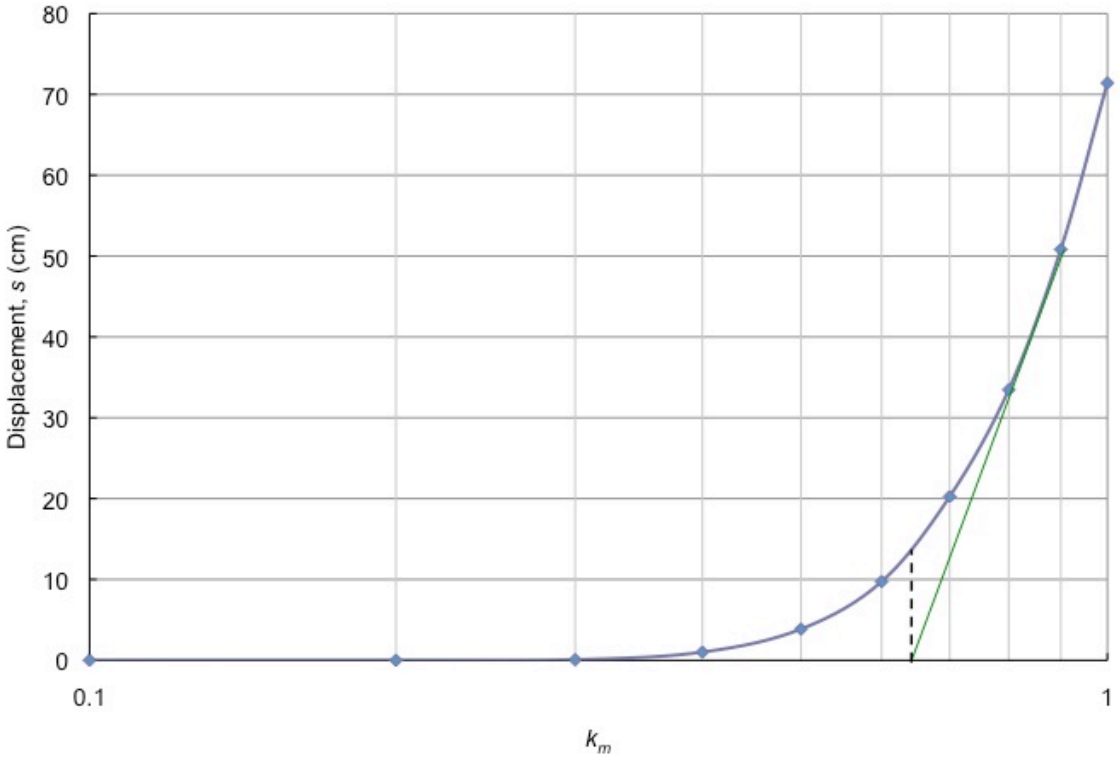

B.1. Permanent displacement calculated for the negative orientation of the fault-normal component accelerogram generated at Auletta, Italy.

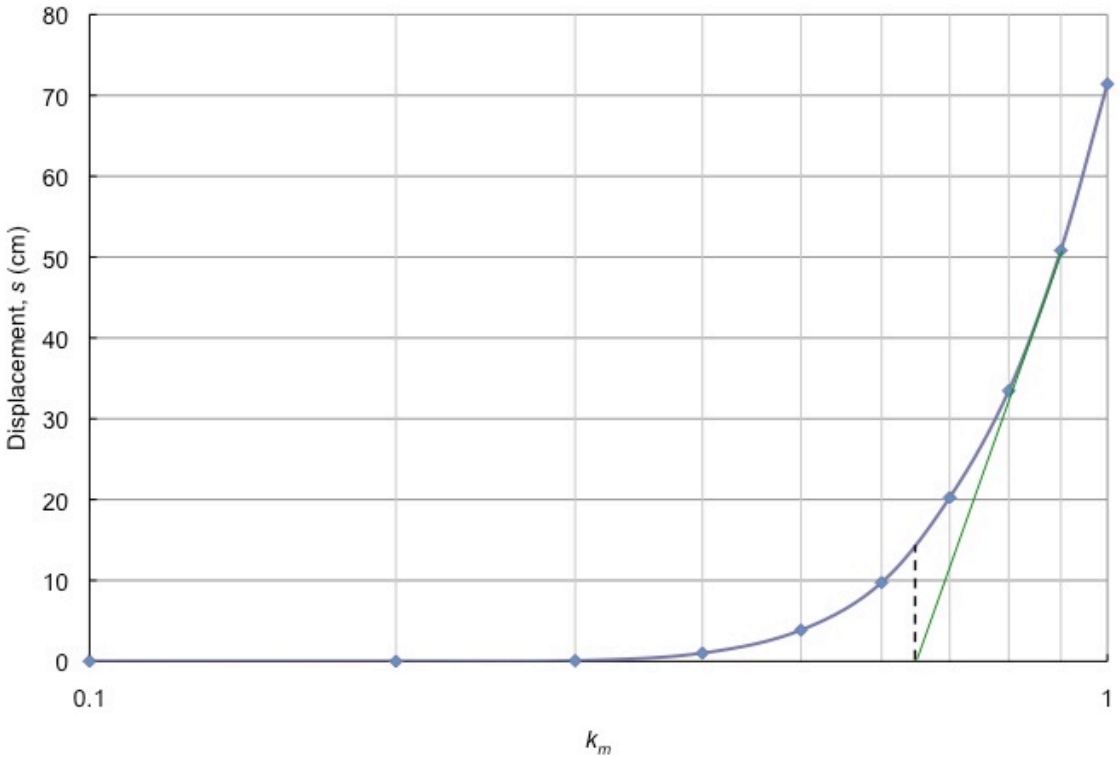

B.2. Permanent displacement calculated for the positive orientation of the fault-normal component accelerogram generated at Auletta, Italy.

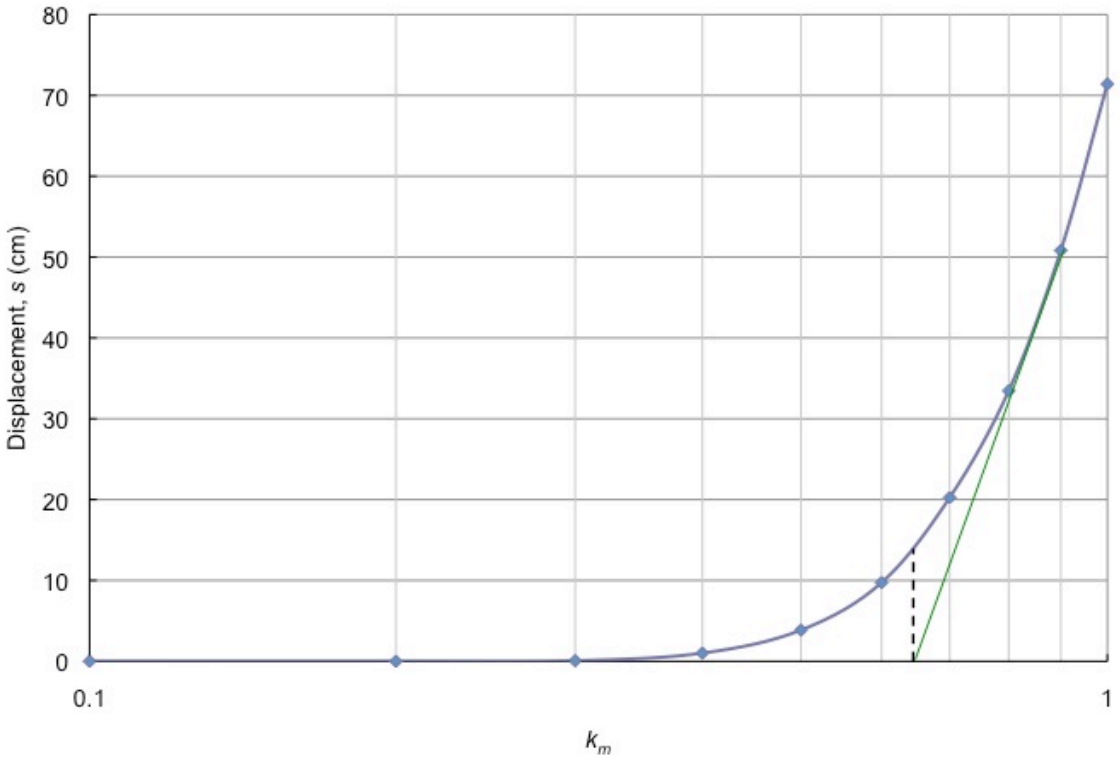

B.3. Permanent displacement calculated for the negative orientation of the fault-parallel component accelerogram generated at Auletta, Italy.

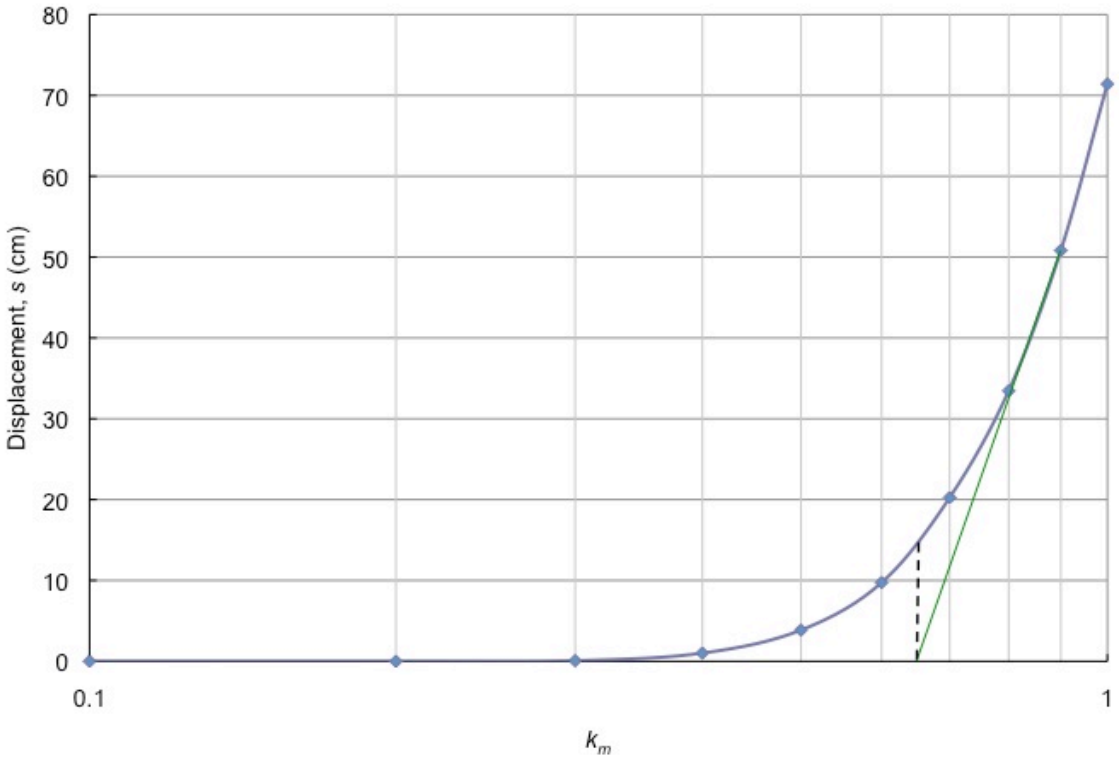

B.4. Permanent displacement calculated for the positive orientation of the fault-parallel component accelerogram generated at Auletta, Italy.

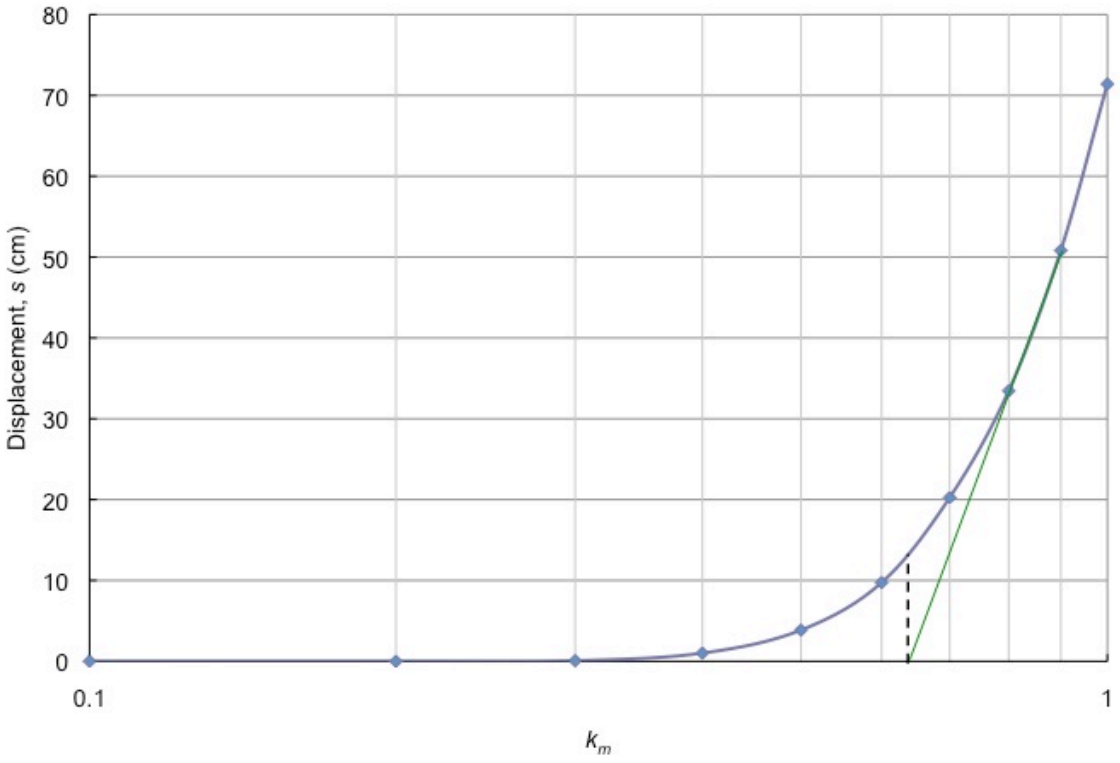

B.5. Permanent displacement calculated for the negative orientation of the fault-normal component accelerogram generated at Bagnoli, Italy.

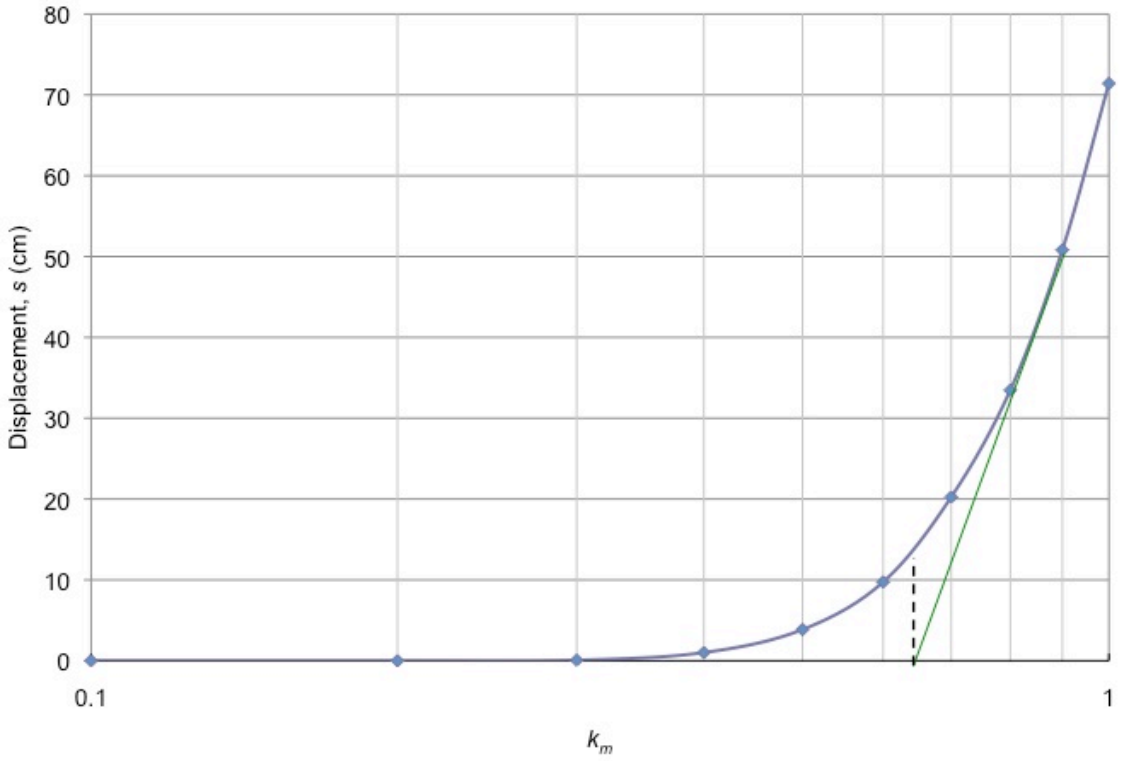

B.6. Permanent displacement calculated for the positive orientation of the fault-normal component accelerogram generated at Bagnoli, Italy.

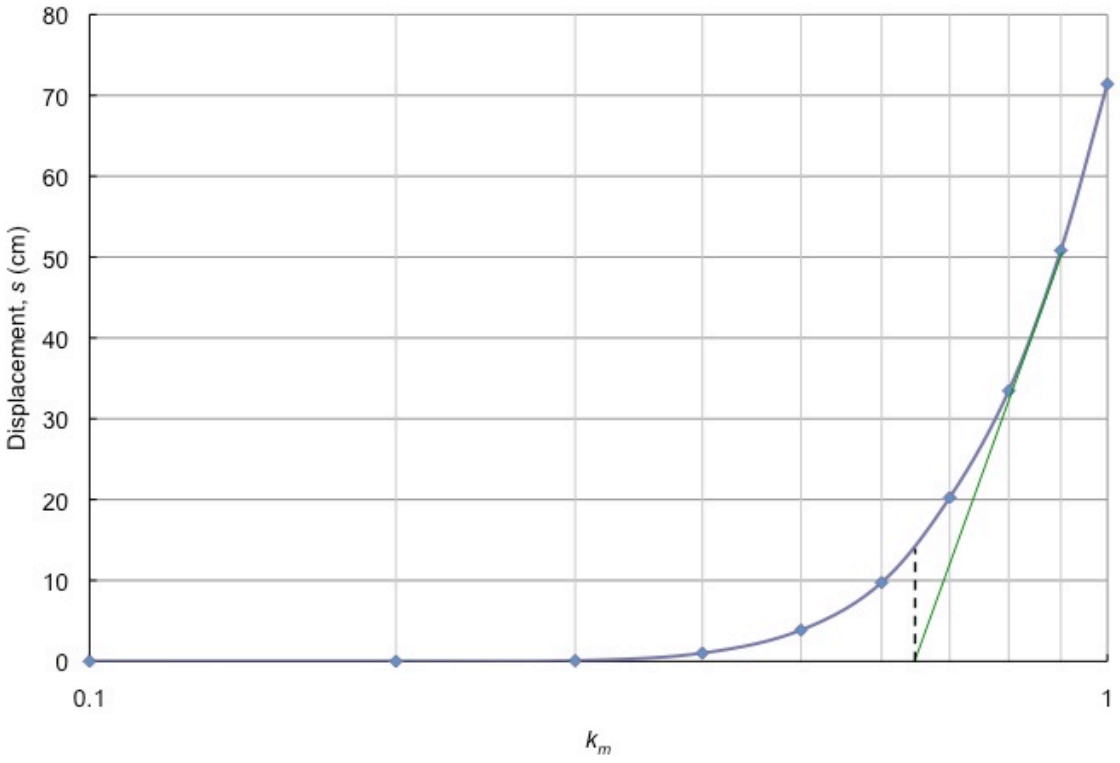

B.7. Permanent displacement calculated for the negative orientation of the fault-parallel component accelerogram generated at Bagnoli, Italy.

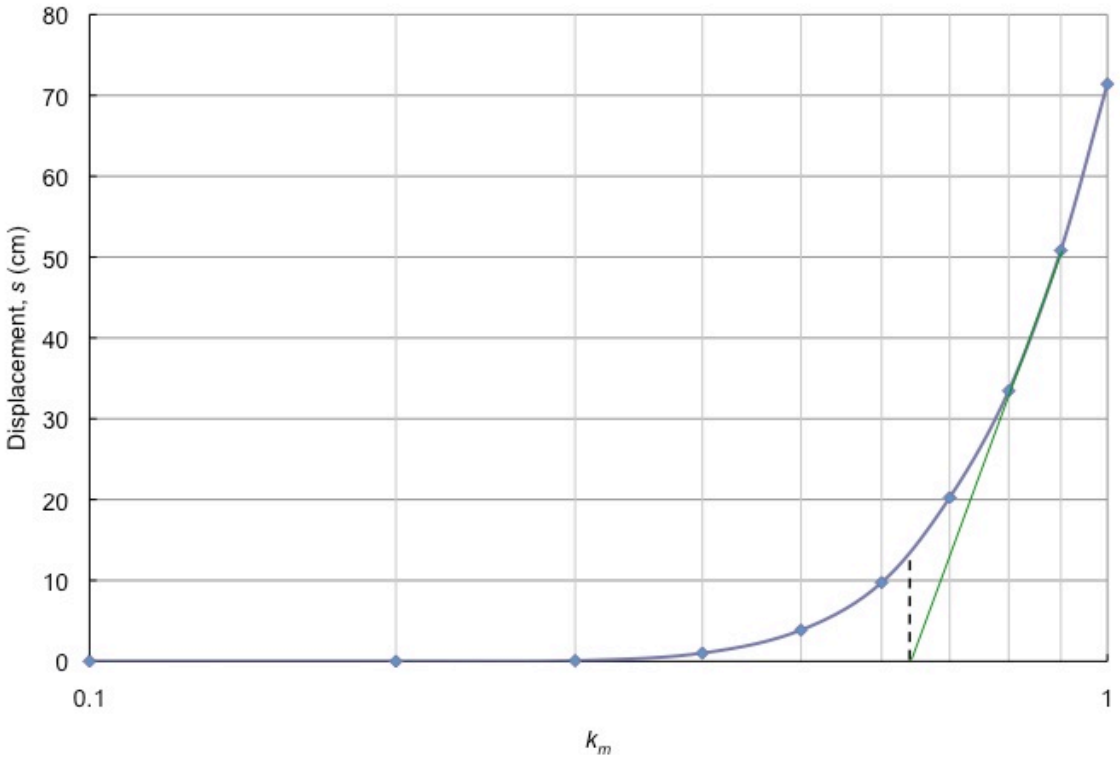

B.8. Permanent displacement calculated for the positive orientation of the fault-parallel component accelerogram generated at Bagnoli, Italy.

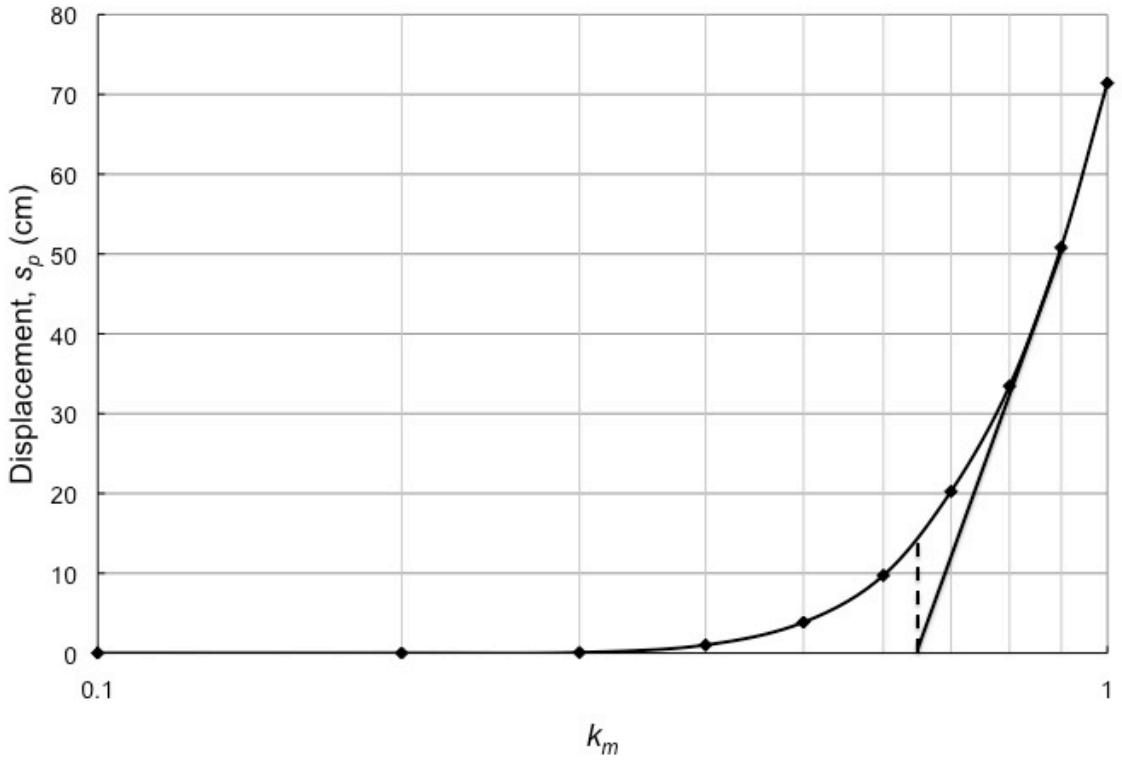

B.9. Permanent displacement calculated for the negative orientation of the fault-normal component accelerogram generated at Sturno, Italy.

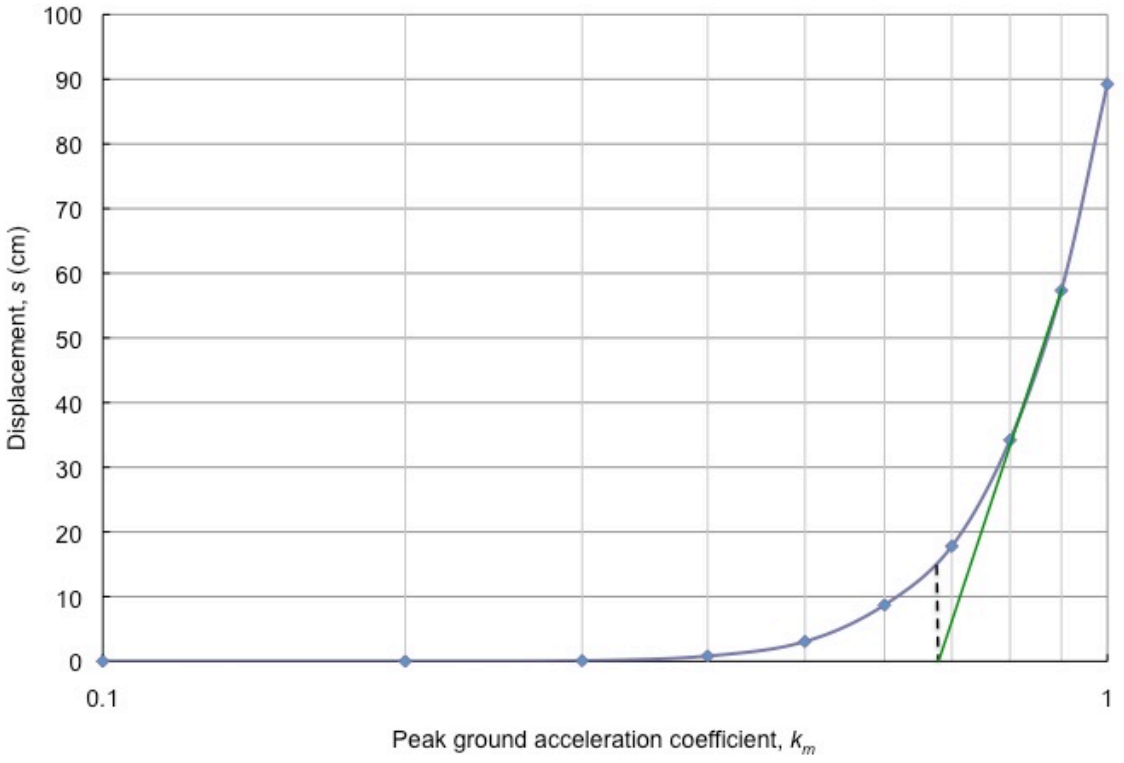

B.10. Permanent displacement calculated for the positive orientation of the fault-normal component accelerogram generated at Sturno, Italy.

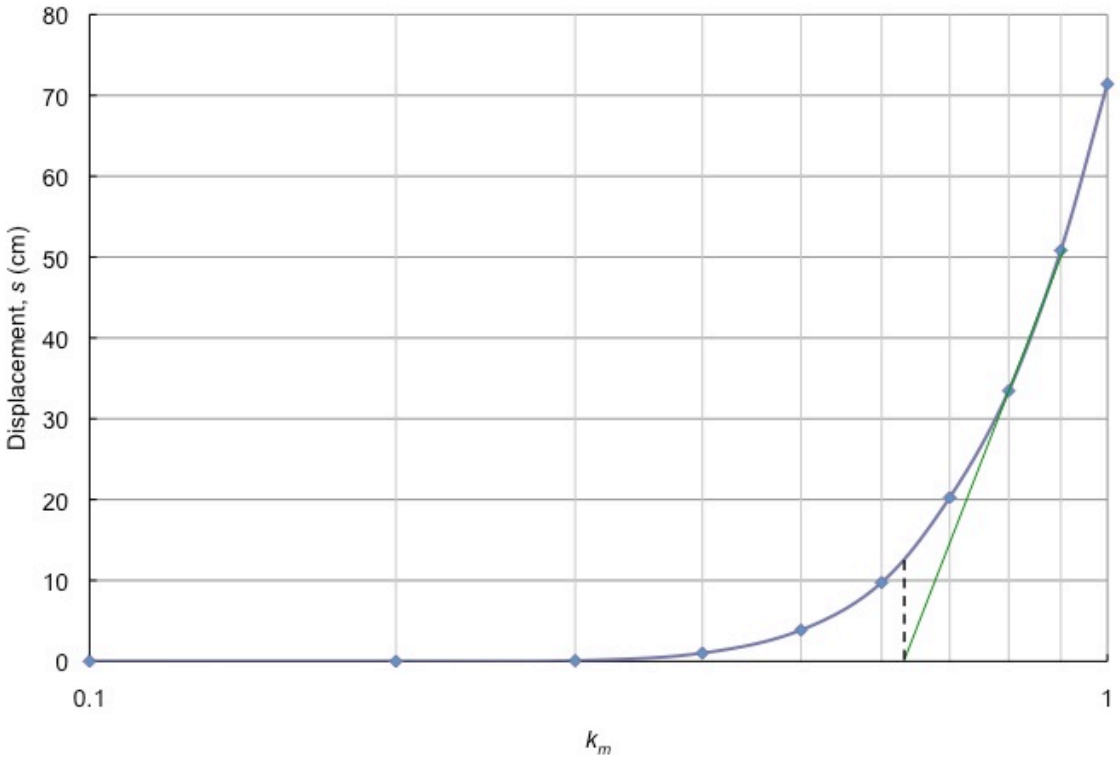

B.11. Permanent displacement calculated for the negative orientation of the fault-parallel component accelerogram generated at Sturno, Italy.

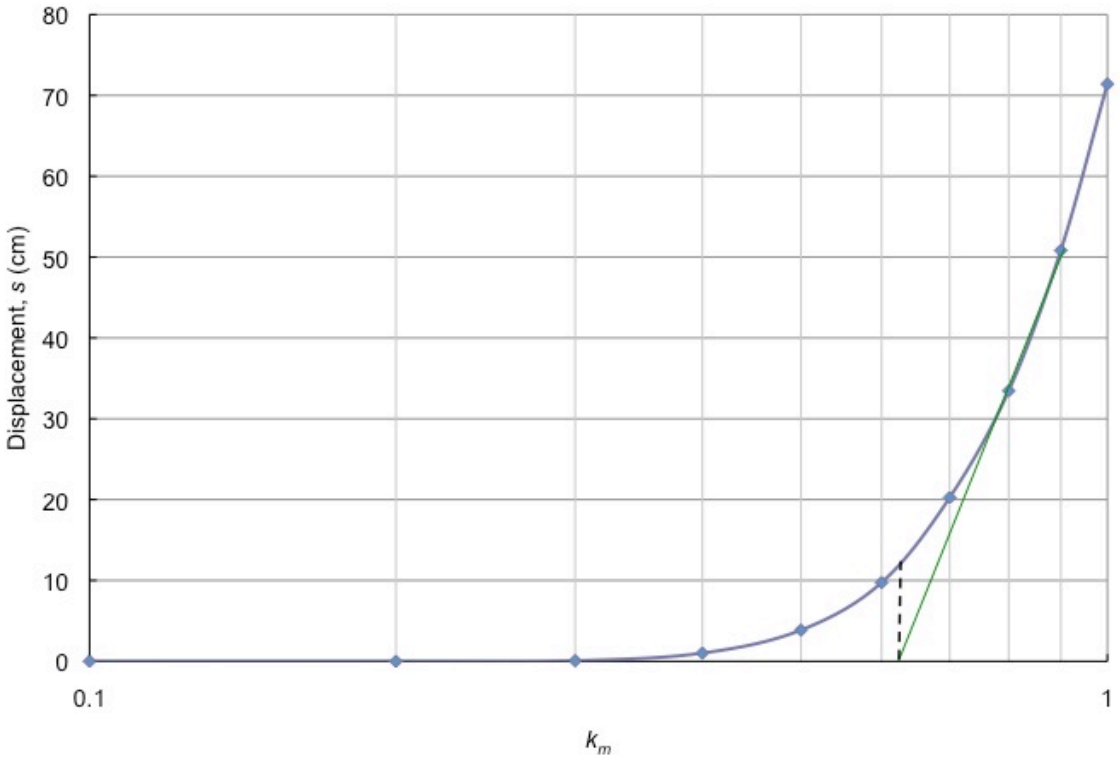

B.12. Permanent displacement calculated for the positive orientation of the fault-parallel component accelerogram generated at Sturno, Italy.

Nonnormal-Faulting Earthquakes in

Dry Conditions

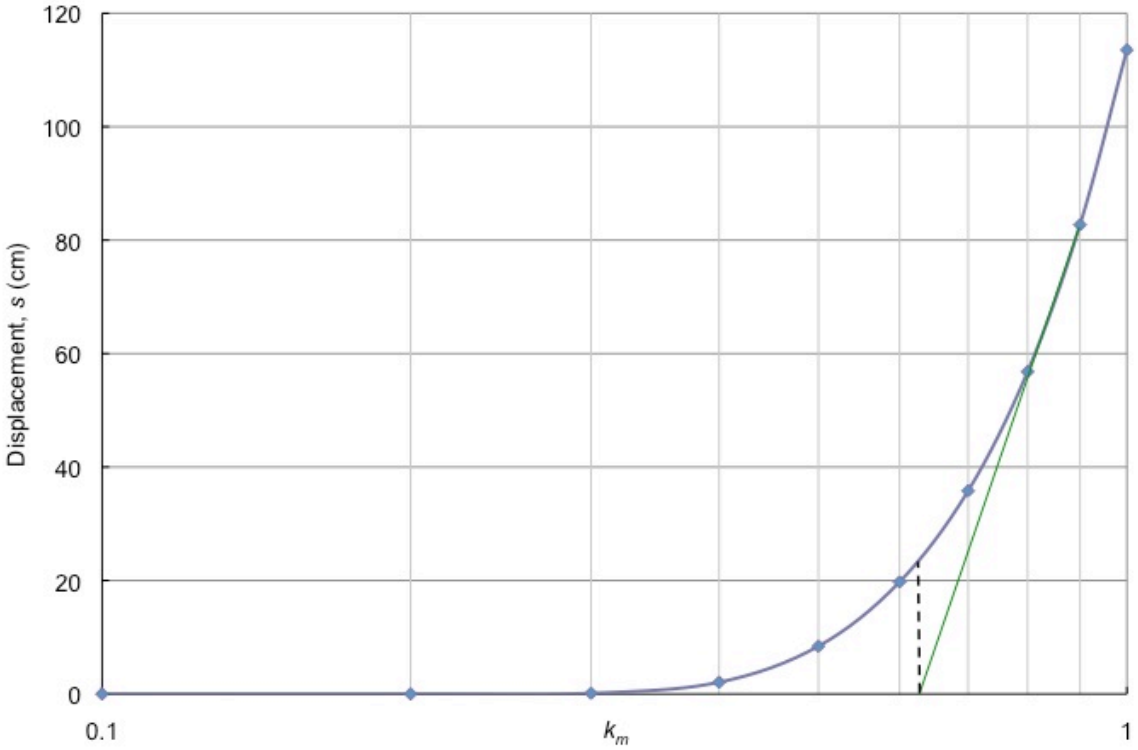

B.13. Permanent displacement calculated for the negative orientation of the fault-normal component accelerogram generated at Kocaeli, Italy.

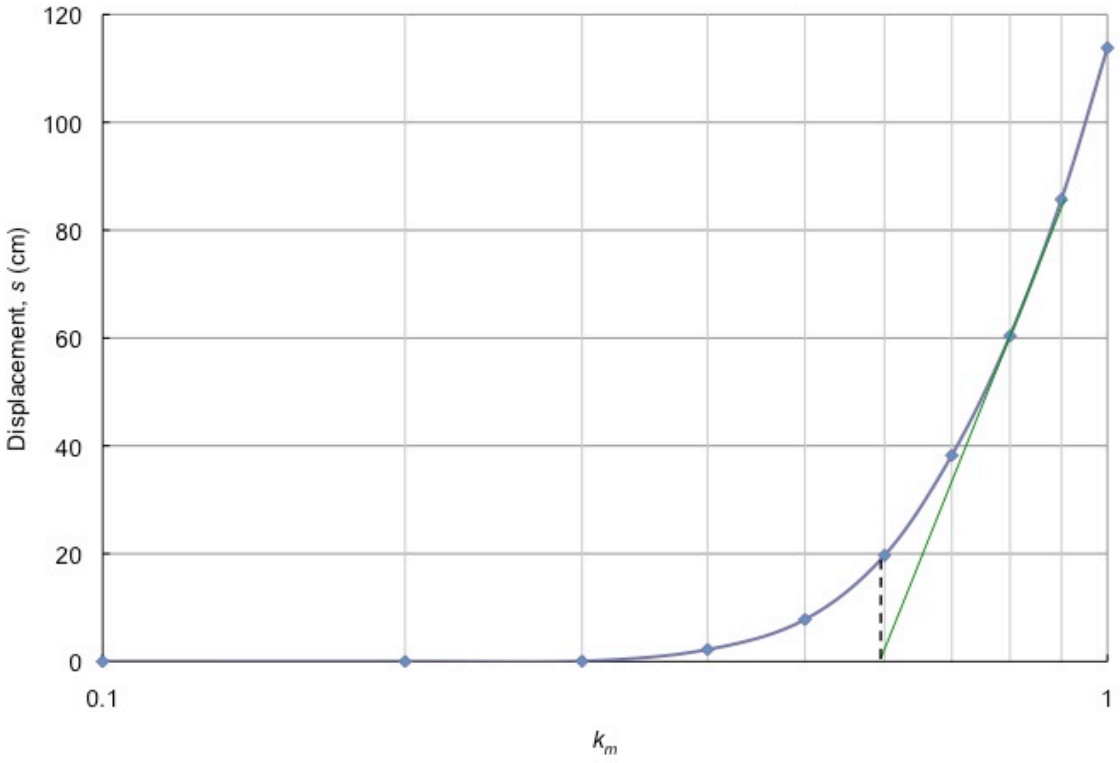

B.14. Permanent displacement calculated for the positive orientation of the fault-normal component accelerogram generated at Kocaeli, Italy.

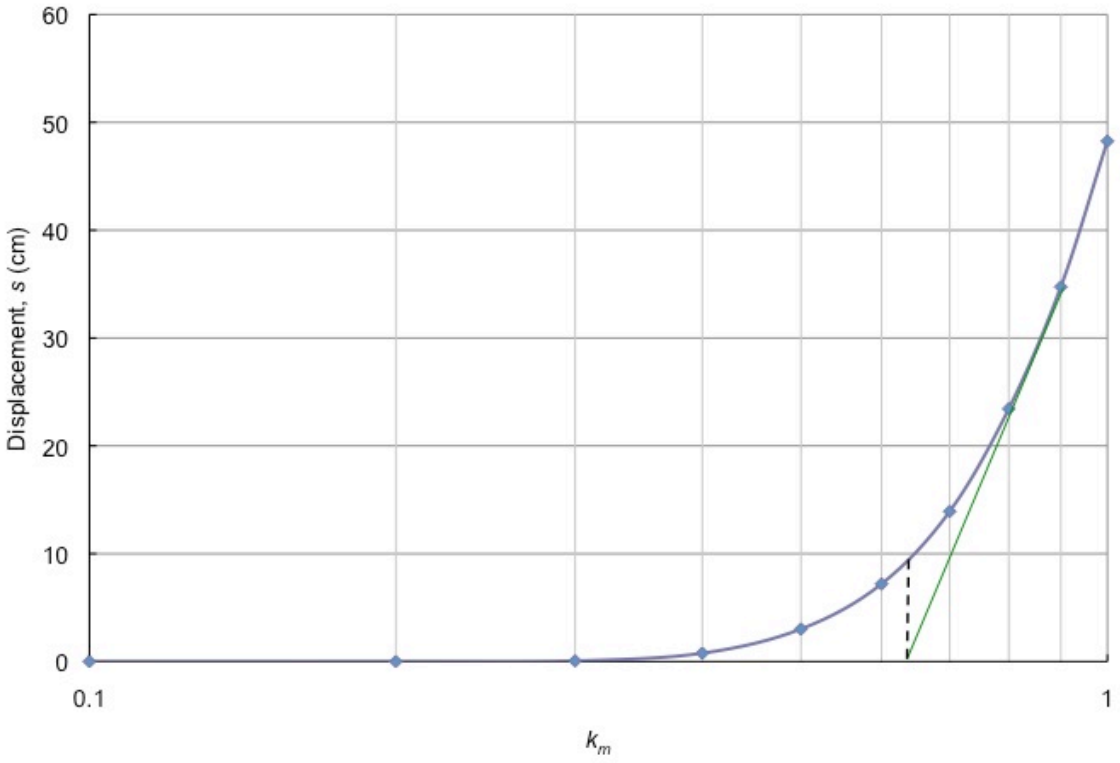

B.15. Permanent displacement calculated for the negative orientation of the fault-parallel component accelerogram generated at Kocaeli, Italy.

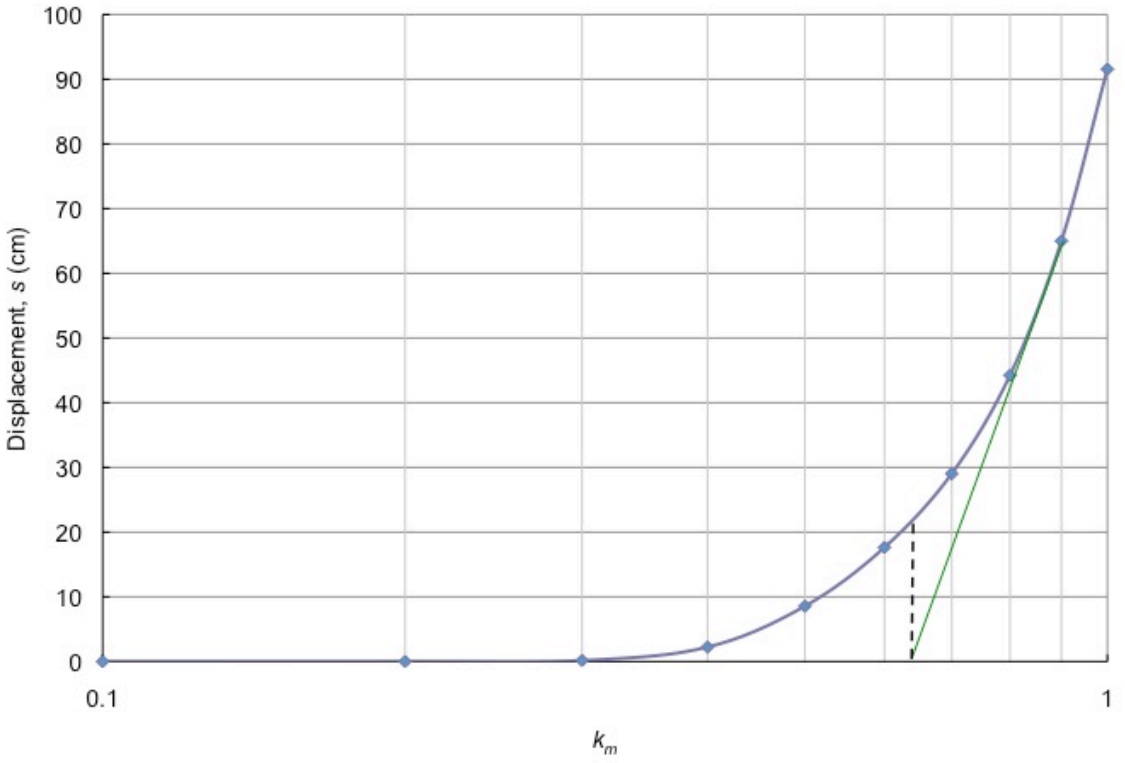

B.16. Permanent displacement calculated for the positive orientation of the fault-parallel component accelerogram generated at Kocaeli, Italy.

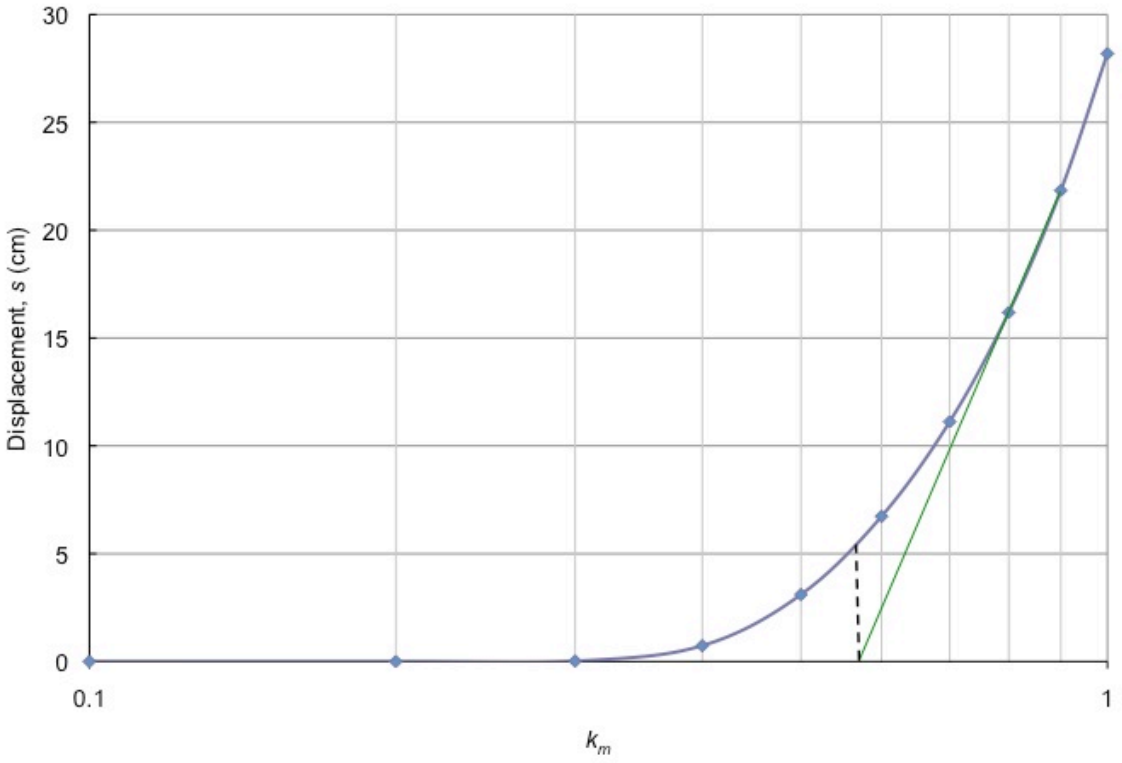

B.17. Permanent displacement calculated for the negative orientation of the fault-normal component accelerogram generated at Loma Prieta, USA.

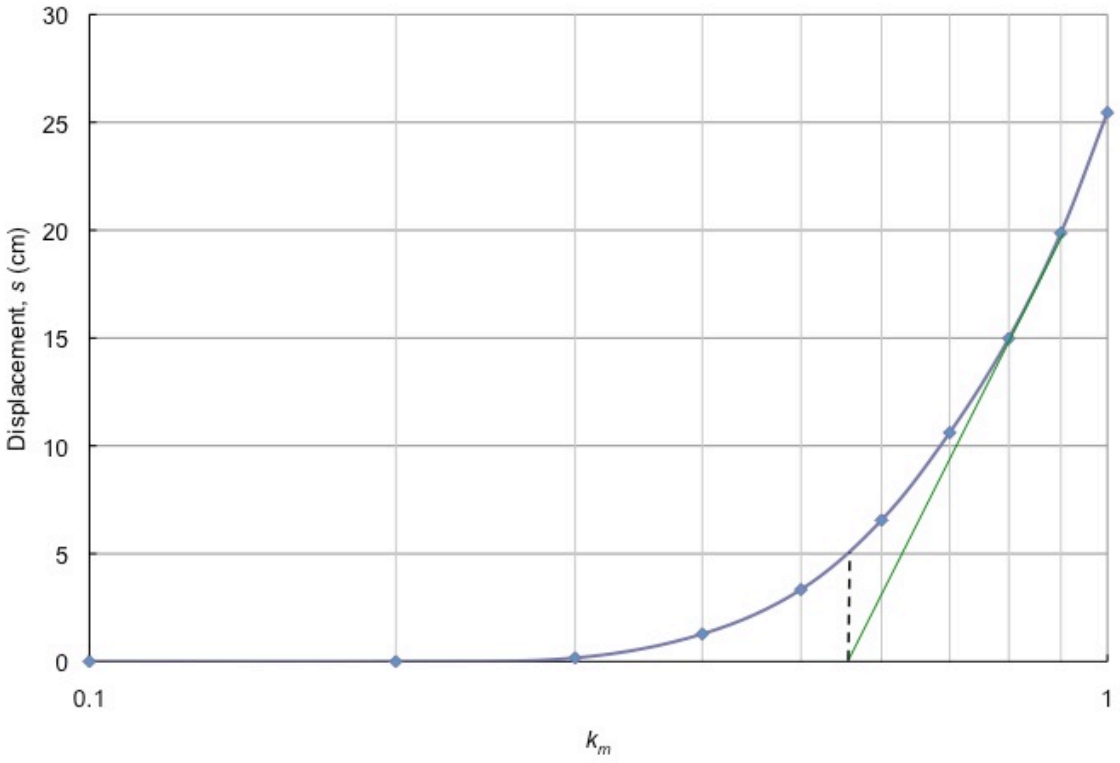

B.18. Permanent displacement calculated for the positive orientation of the fault-normal component accelerogram generated at Loma Prieta, USA.

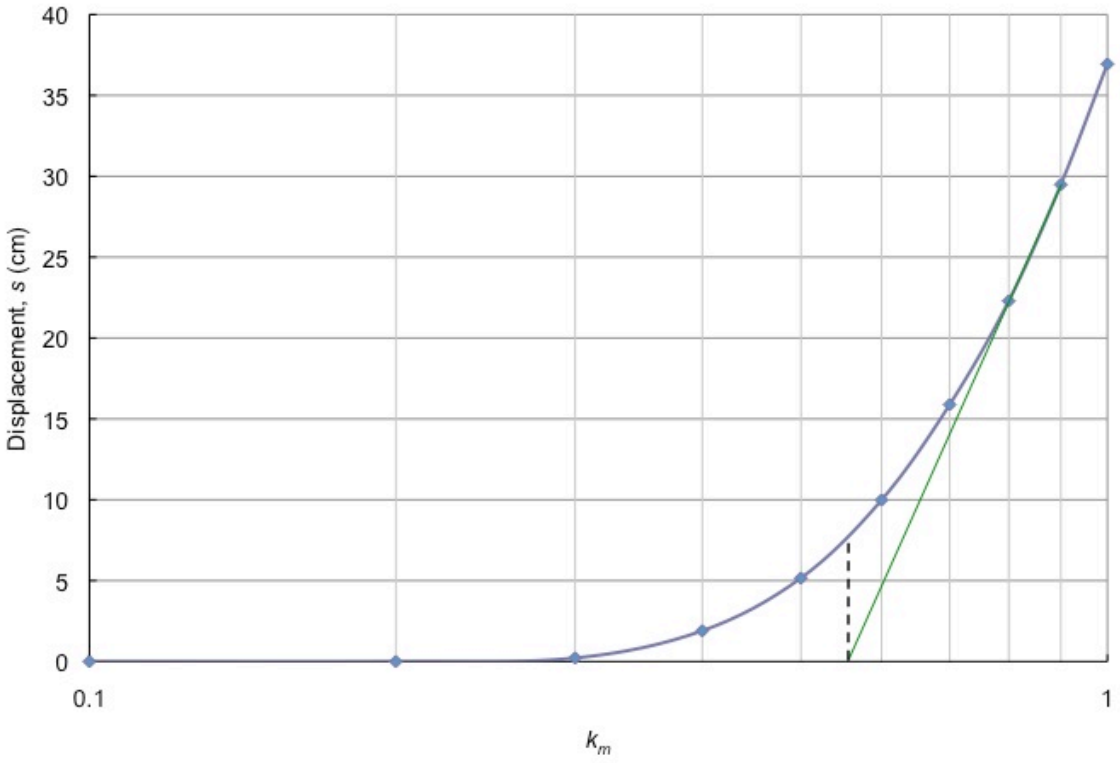

B.19. Permanent displacement calculated for the negative orientation of the fault-parallel component accelerogram generated at Loma Prieta, USA.

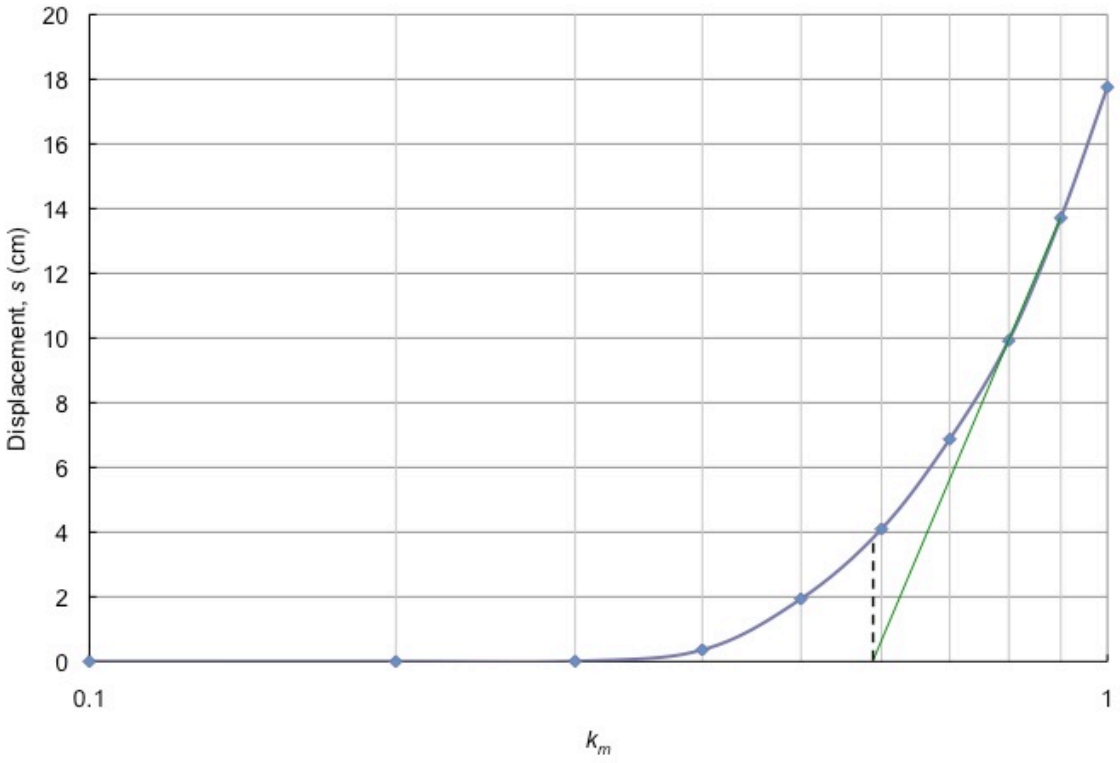

B.20. Permanent displacement calculated for the positive orientation of the fault-parallel component accelerogram generated at Loma Prieta, USA.

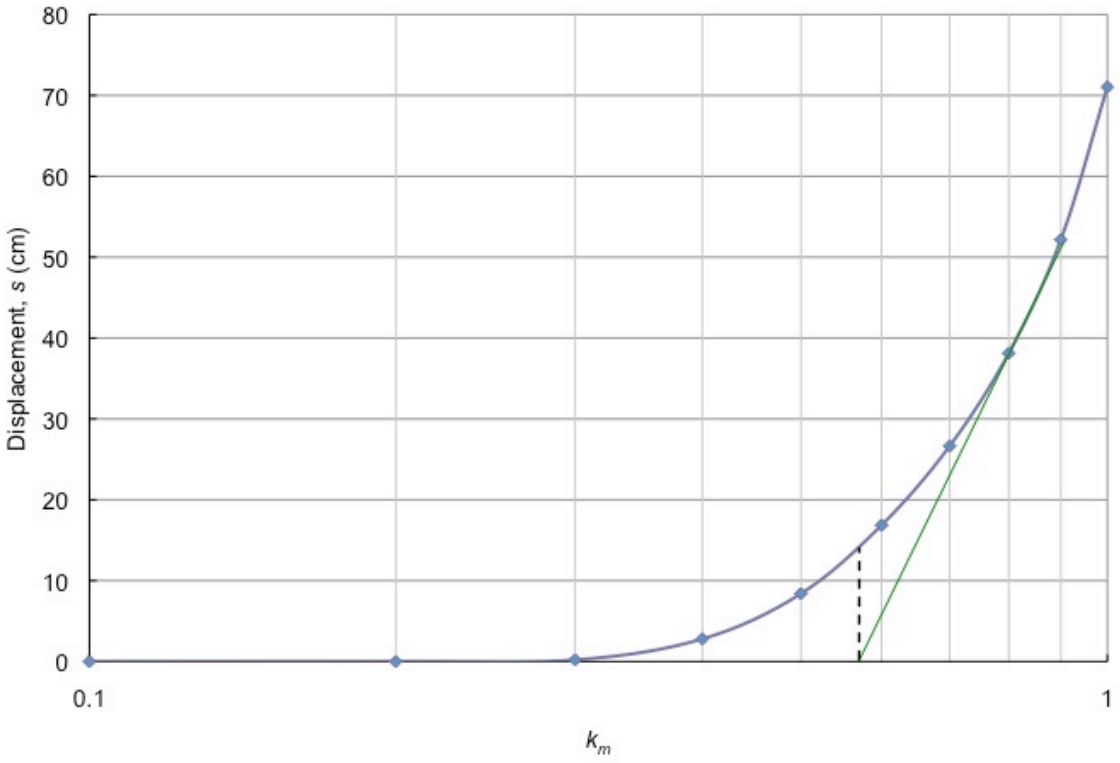

B.21. Permanent displacement calculated for the negative orientation of the fault-normal component accelerogram generated at Tabas, Iran.

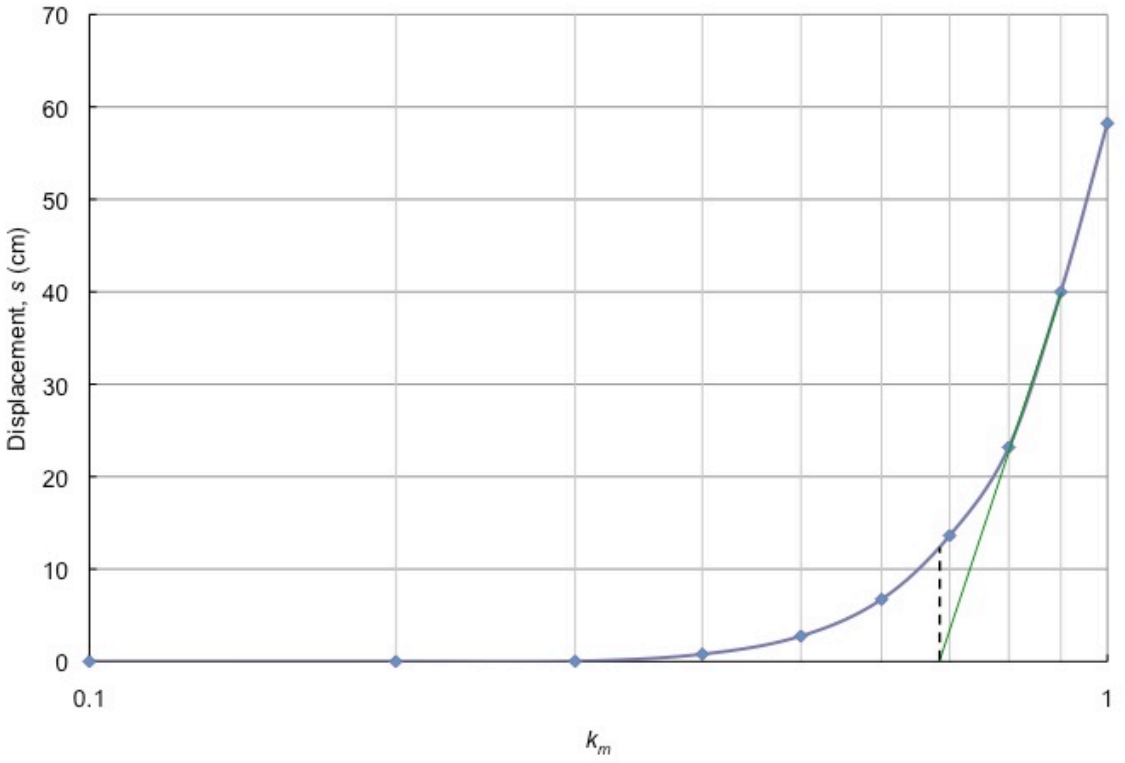

B.22. Permanent displacement calculated for the positive orientation of the fault-normal component accelerogram generated at Tabas, Iran.

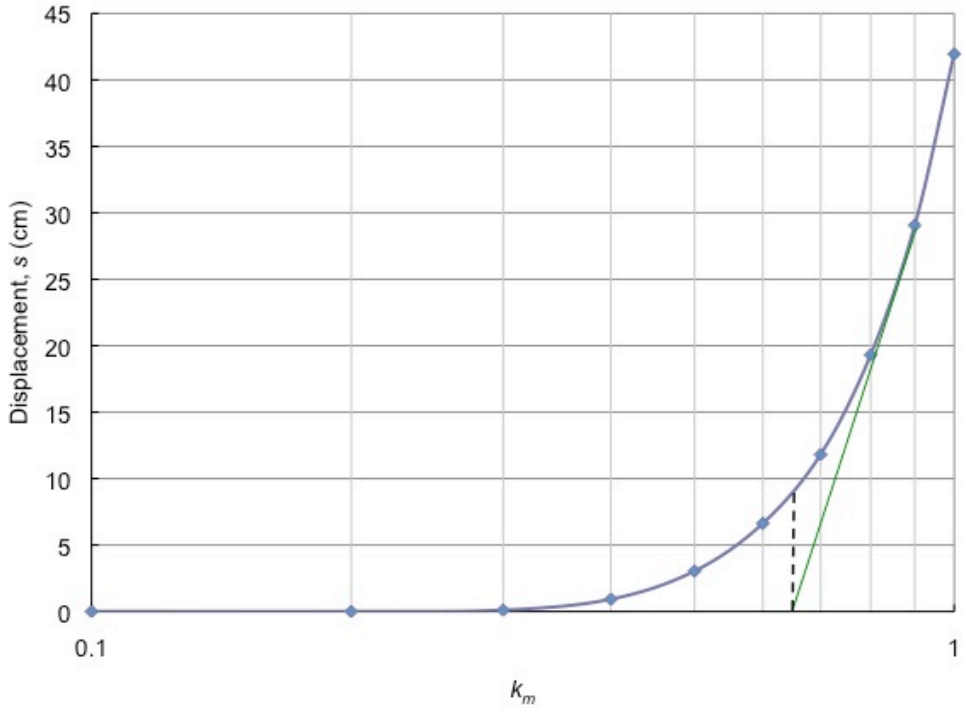

B.23. Permanent displacement calculated for the negative orientation of the fault-parallel component accelerogram generated at Tabas, Iran.

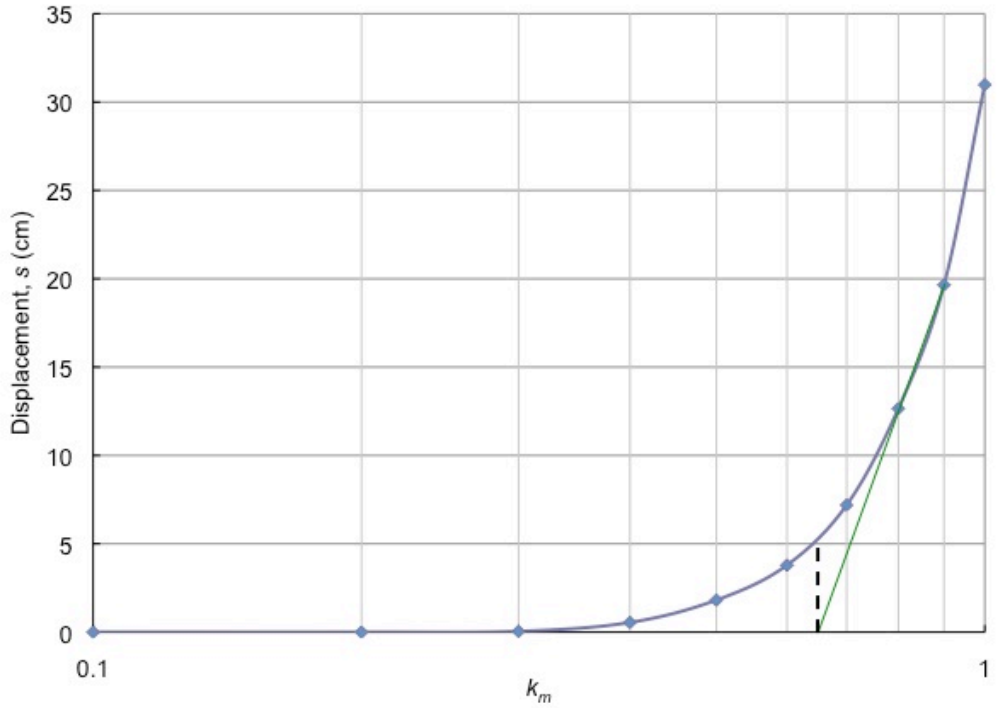

B.24. Permanent displacement calculated for the positive orientation of the fault-parallel component accelerogram generated at Tabas, Iran.

Seismic Waveforms in Dry Conditions

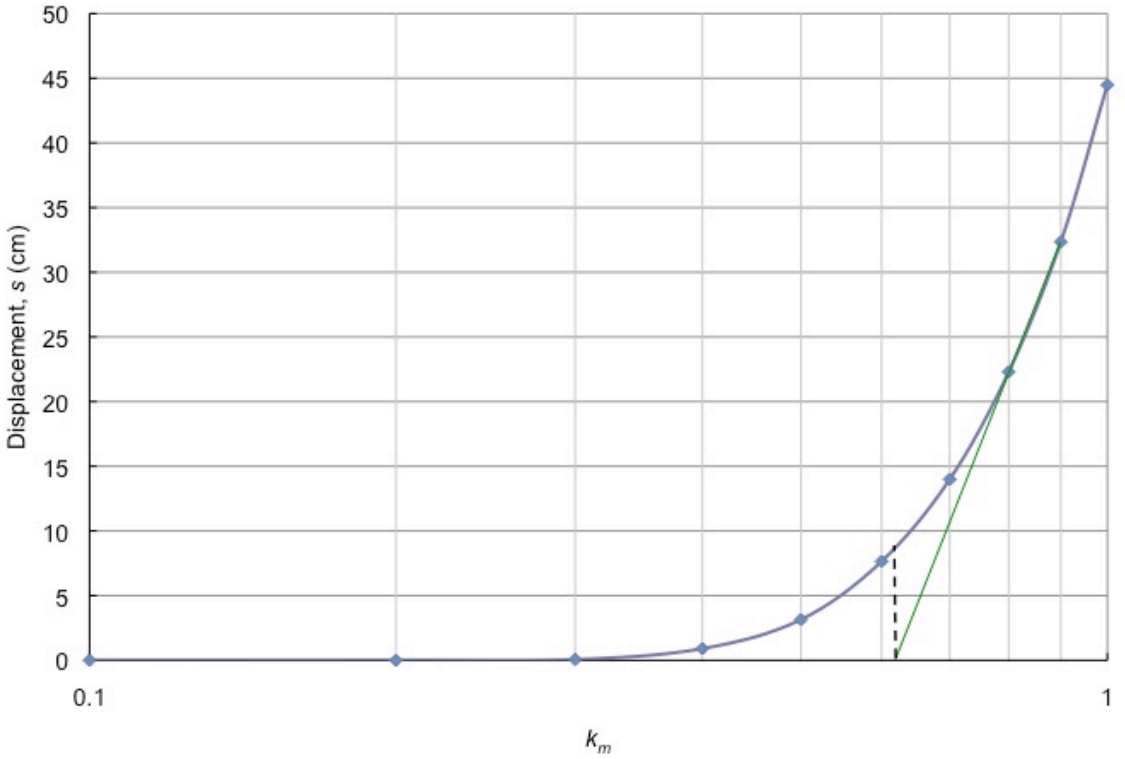

B.25. Permanent displacement calculated for the negative orientation of the fault-normal component accelerogram generated at Chuetsu, Japan.

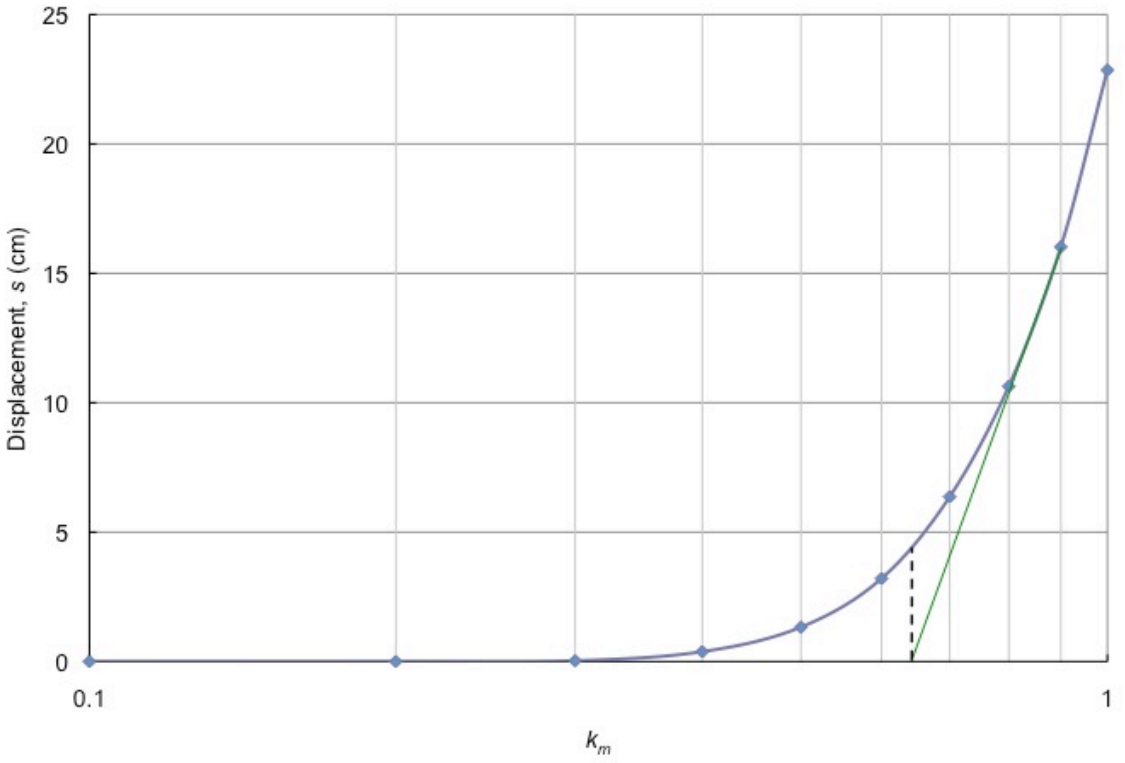

B.26. Permanent displacement calculated for the positive orientation of the fault-normal component accelerogram generated at Chuetsu, Japan.

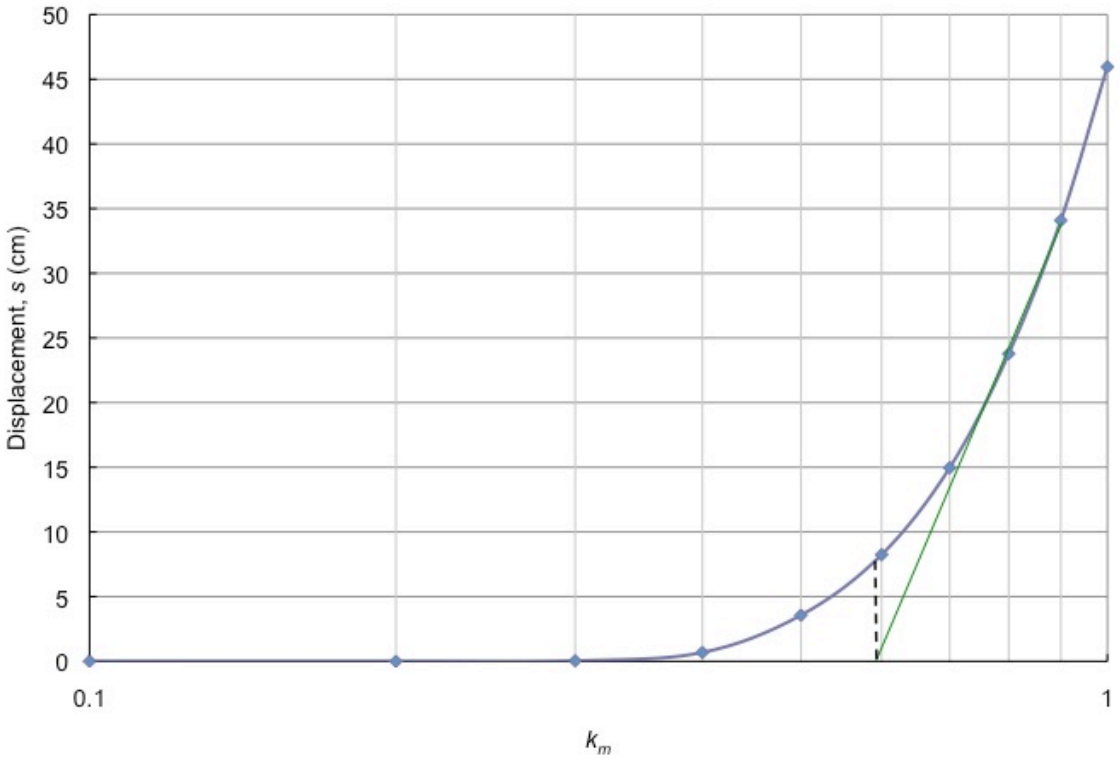

B.27. Permanent displacement calculated for the negative orientation of the fault-parallel component accelerogram generated at Chuetsu, Japan.

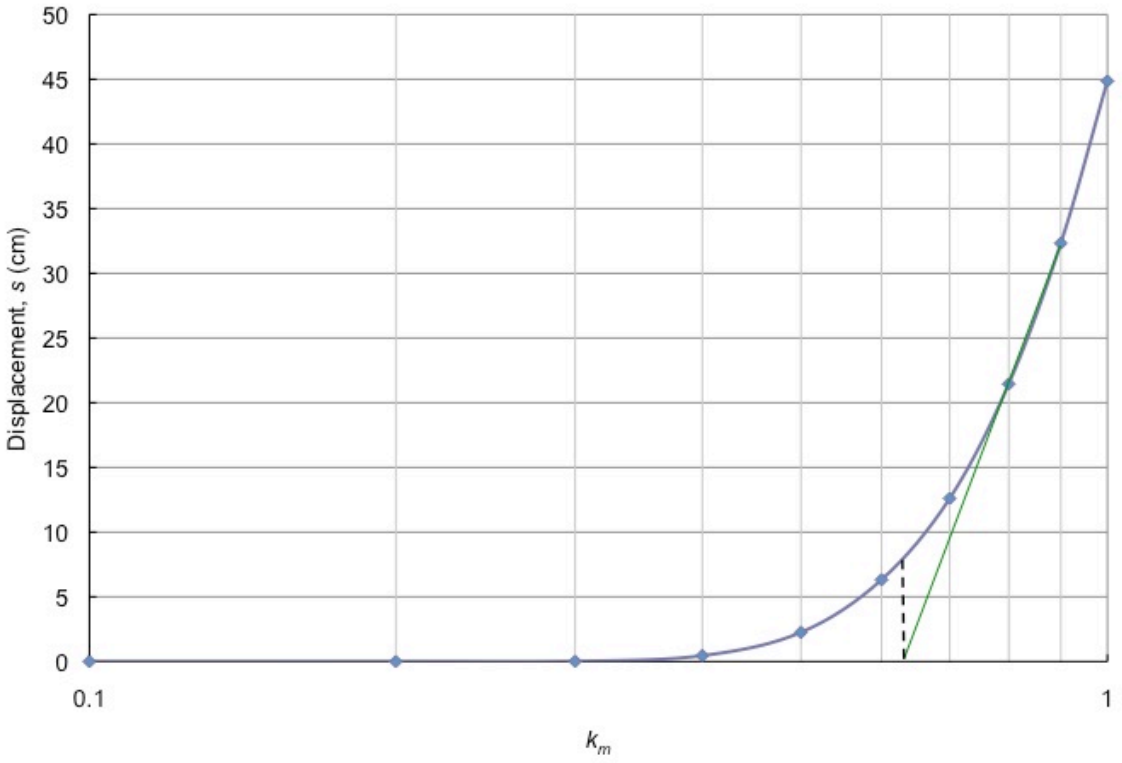

B.28. Permanent displacement calculated for the positive orientation of the fault-parallel component accelerogram generated at Chuetsu, Japan.

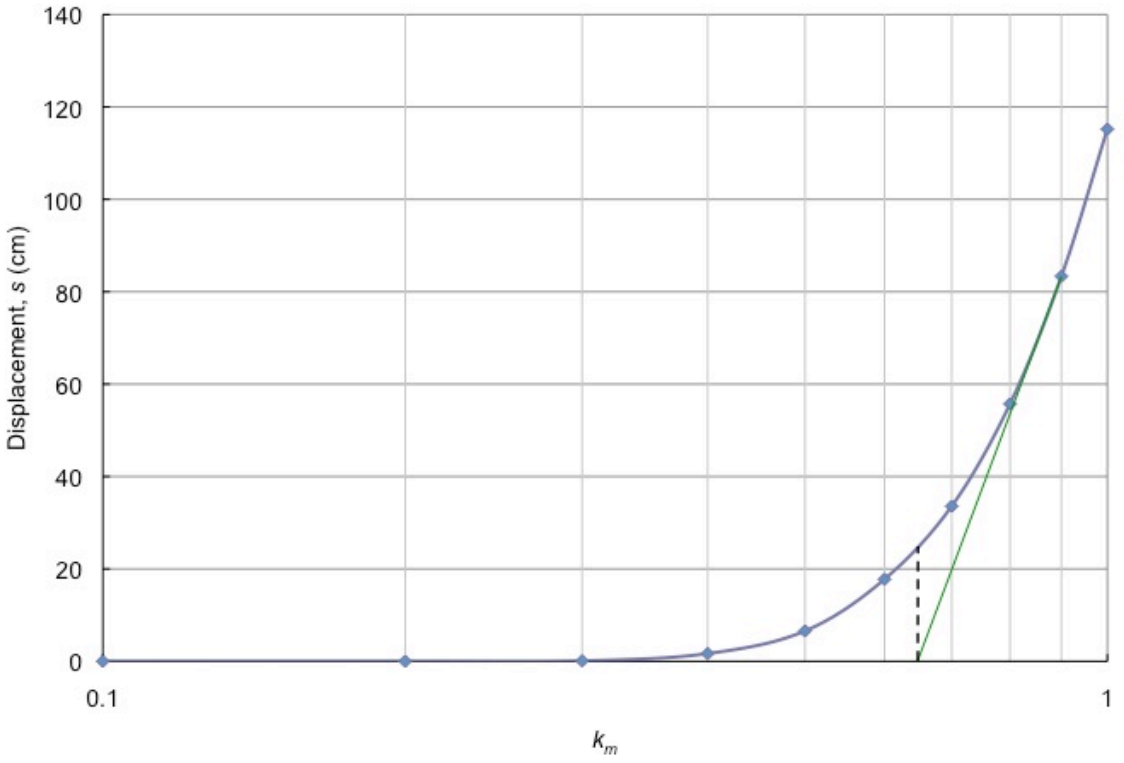

B.29. Permanent displacement calculated for the negative orientation of the fault-normal component accelerogram generated at El Salvador.

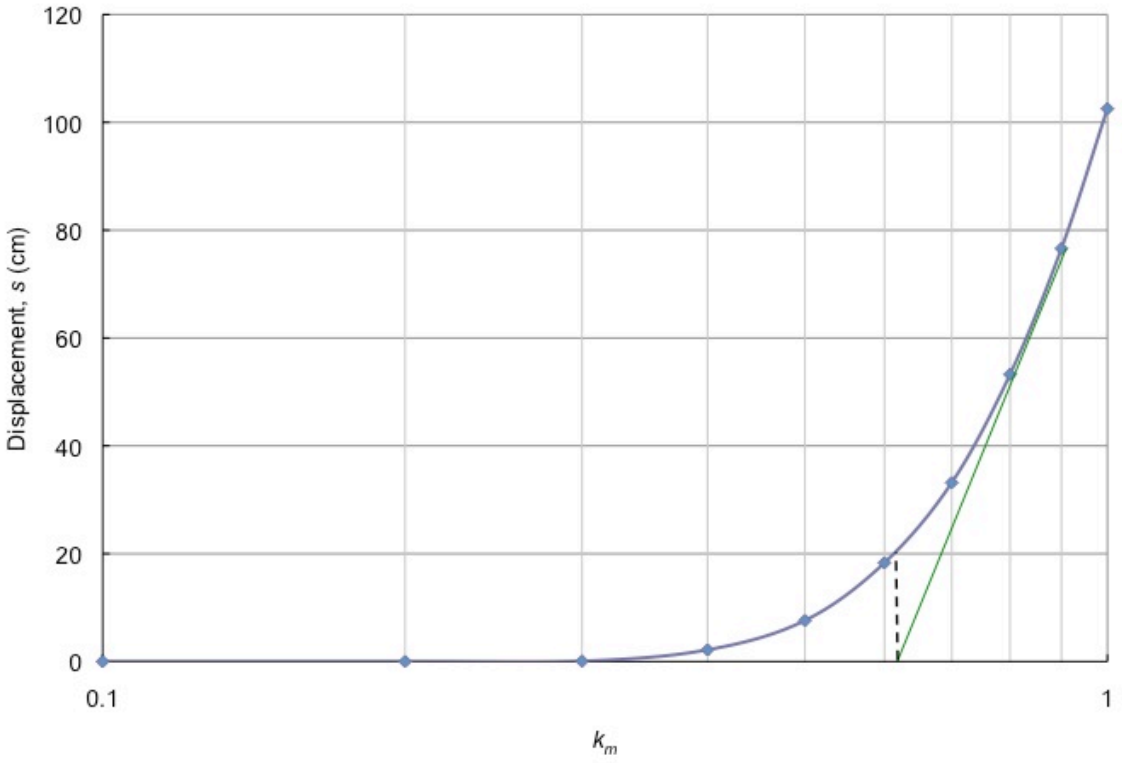

B.30. Permanent displacement calculated for the positive orientation of the fault-normal component accelerogram generated at El Salvador.

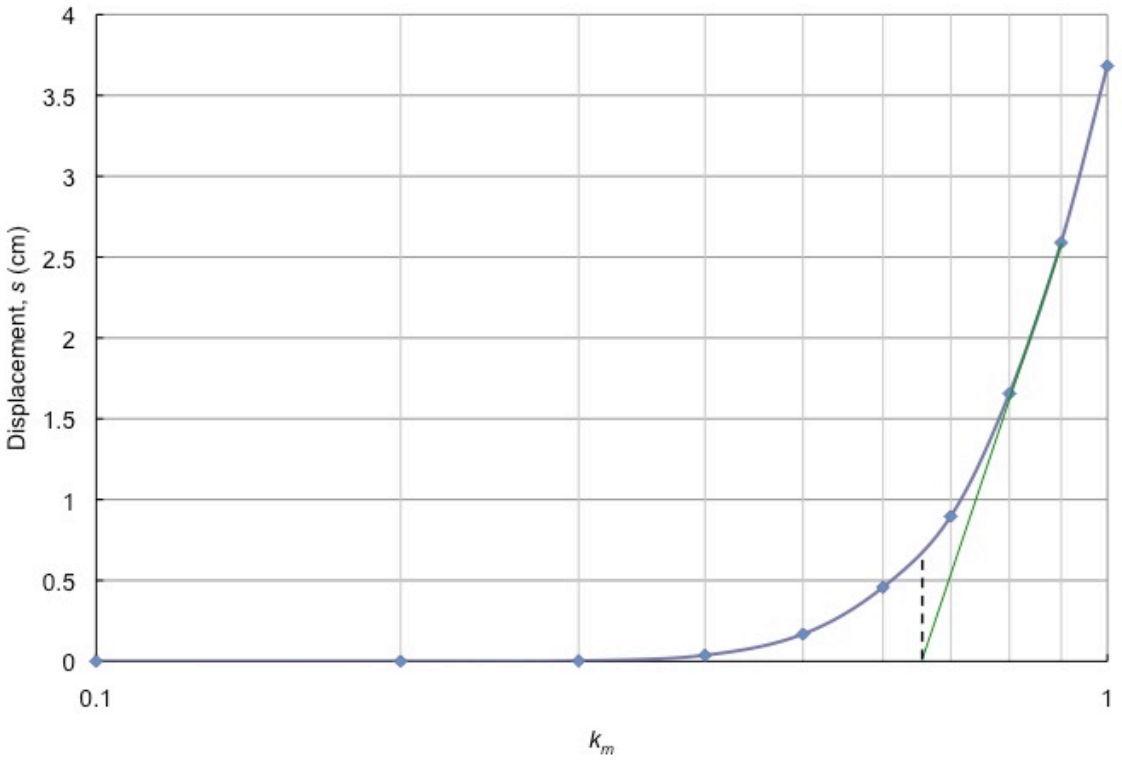

B.31. Permanent displacement calculated for the negative orientation of the fault-parallel component accelerogram generated at Gilroy, USA.

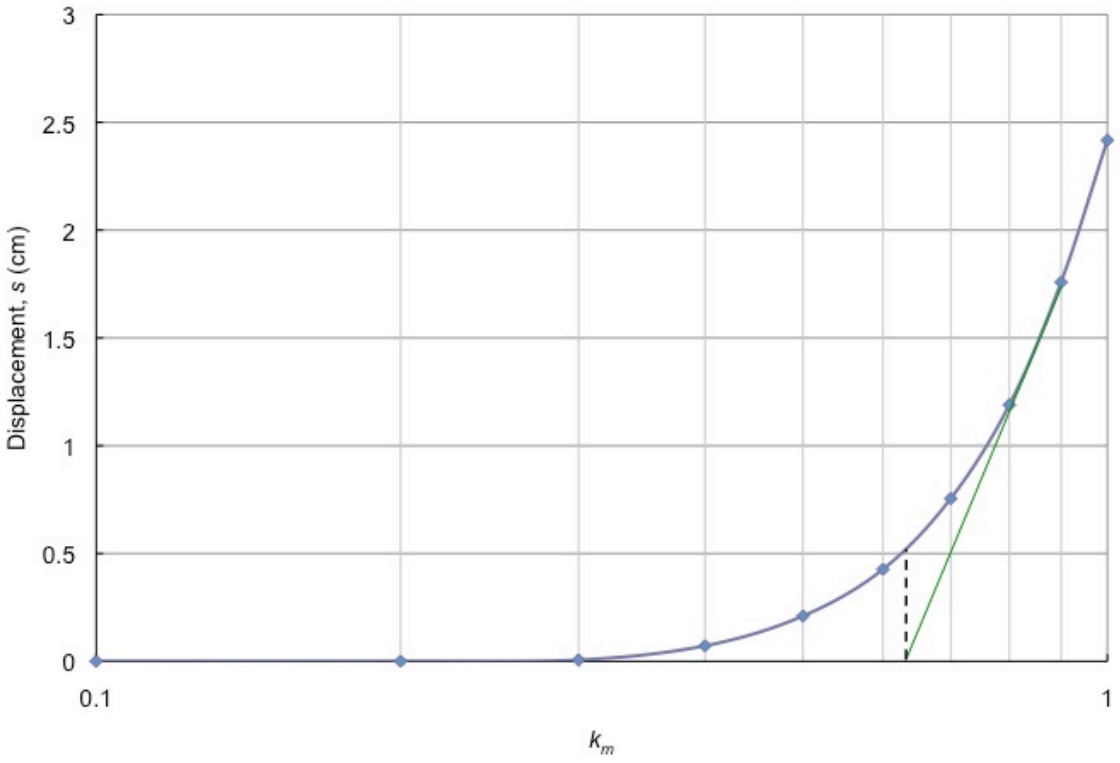

B.32. Permanent displacement calculated for the positive orientation of the fault-parallel component accelerogram generated at Gilroy, USA.

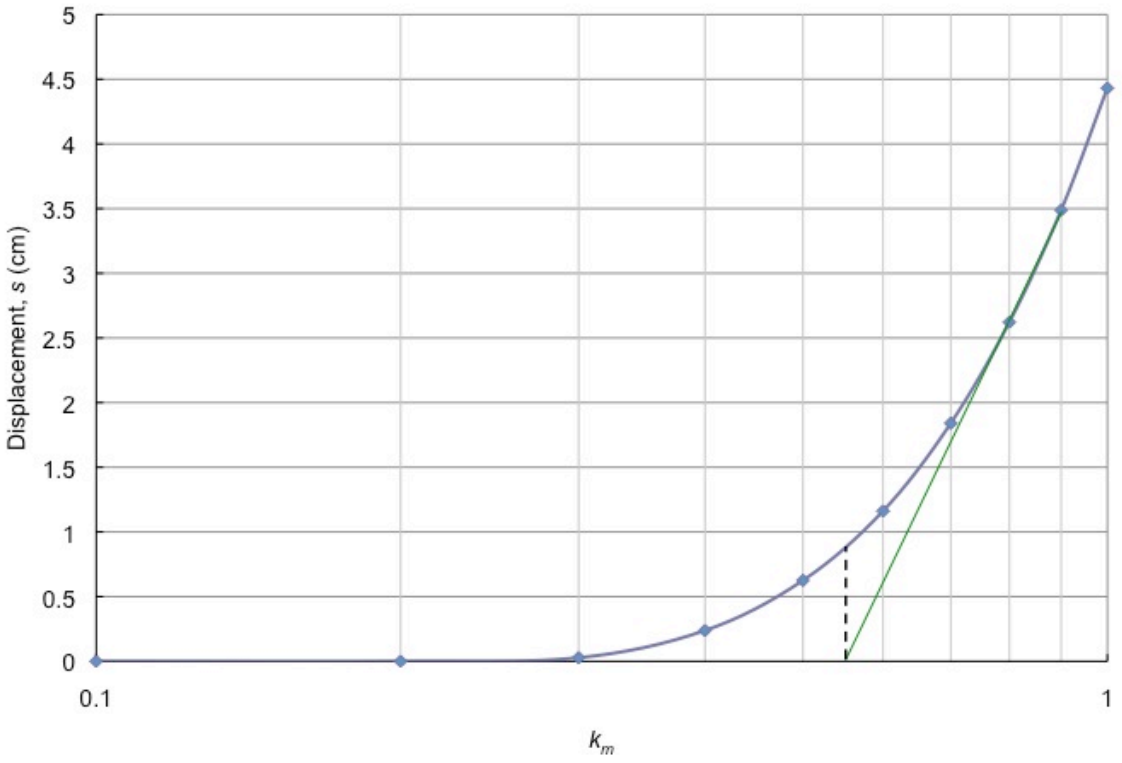

B.33. Permanent displacement calculated for the negative orientation of the fault-normal component accelerogram generated at Gilroy, USA.

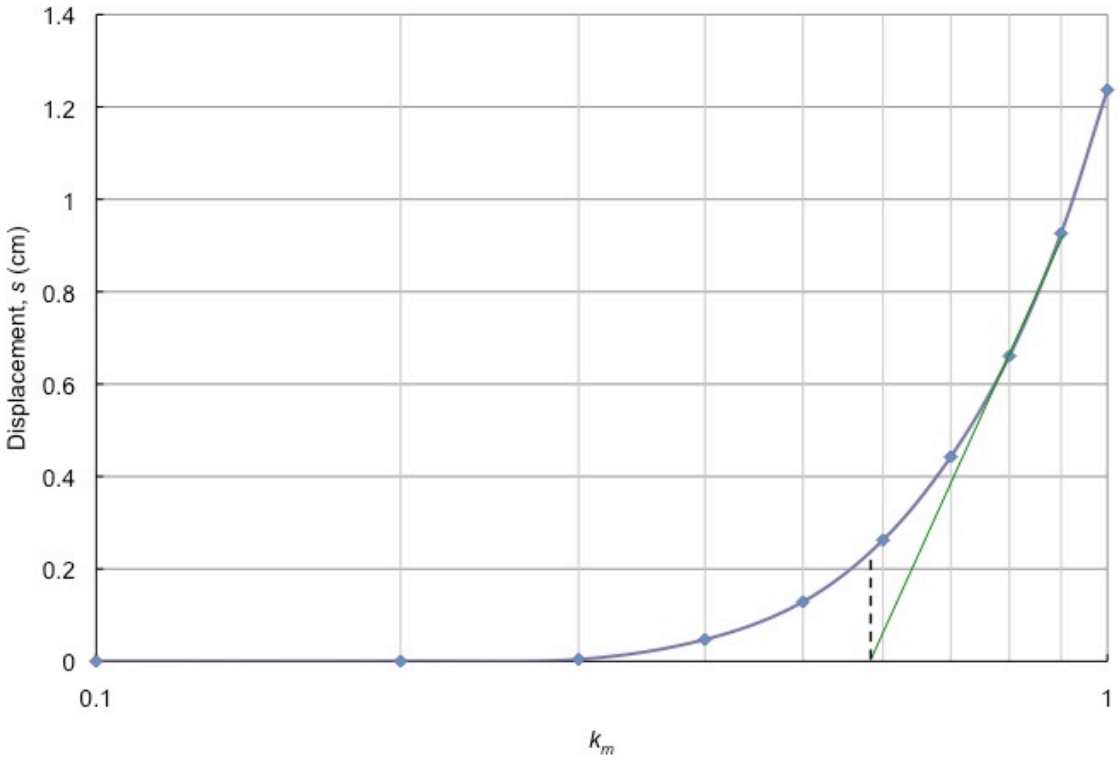

B.34. Permanent displacement calculated for the positive orientation of the fault-normal component accelerogram generated at Gilroy, USA.

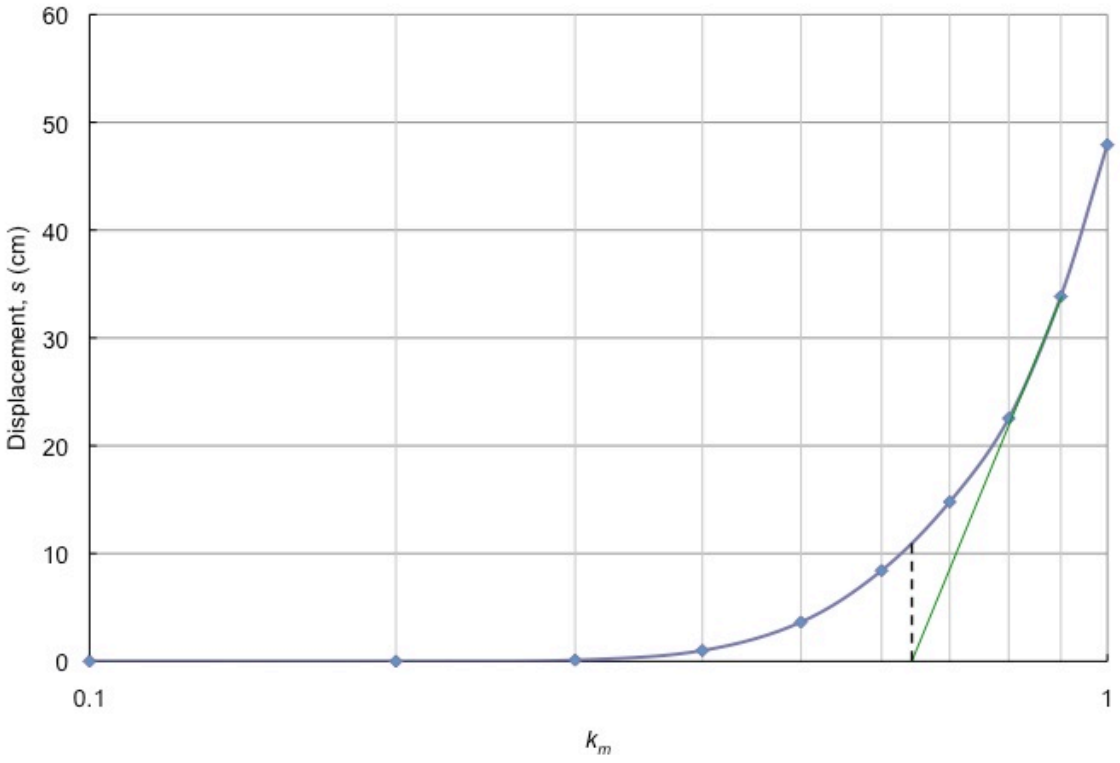

B.35. Permanent displacement calculated for the negative orientation of the fault-parallel component accelerogram generated at Kobe, Japan.

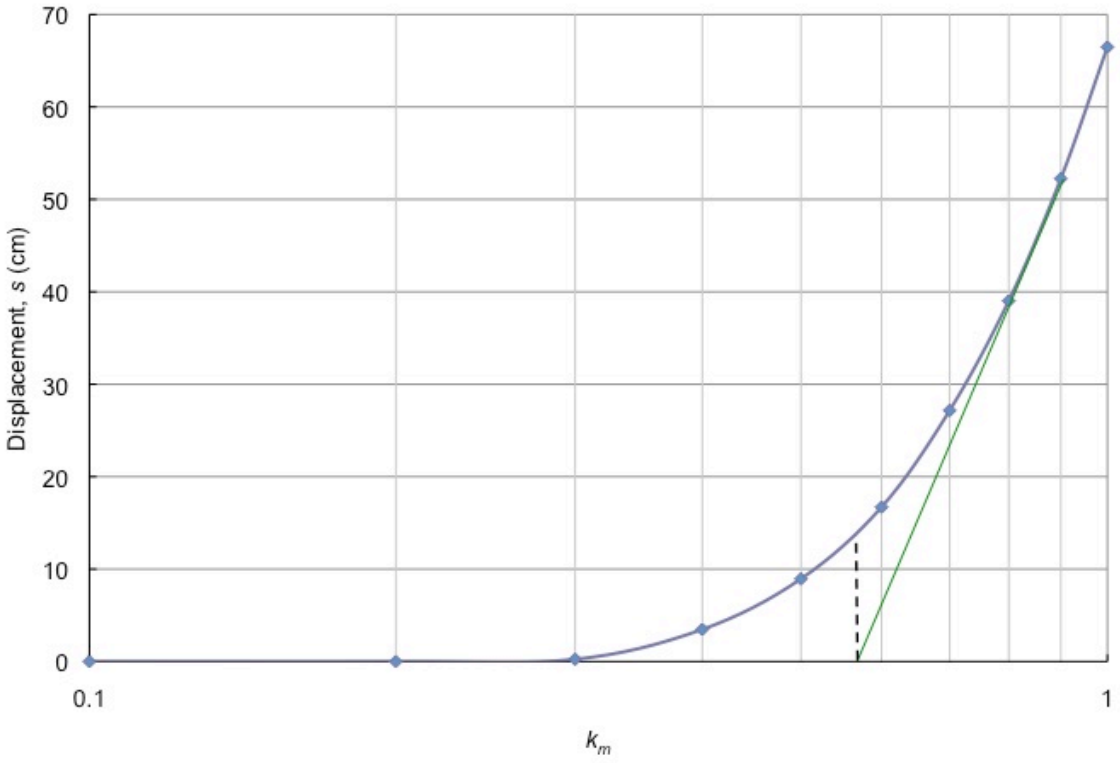

B.36. Permanent displacement calculated for the positive orientation of the fault-parallel component accelerogram generated at Kobe, Japan.

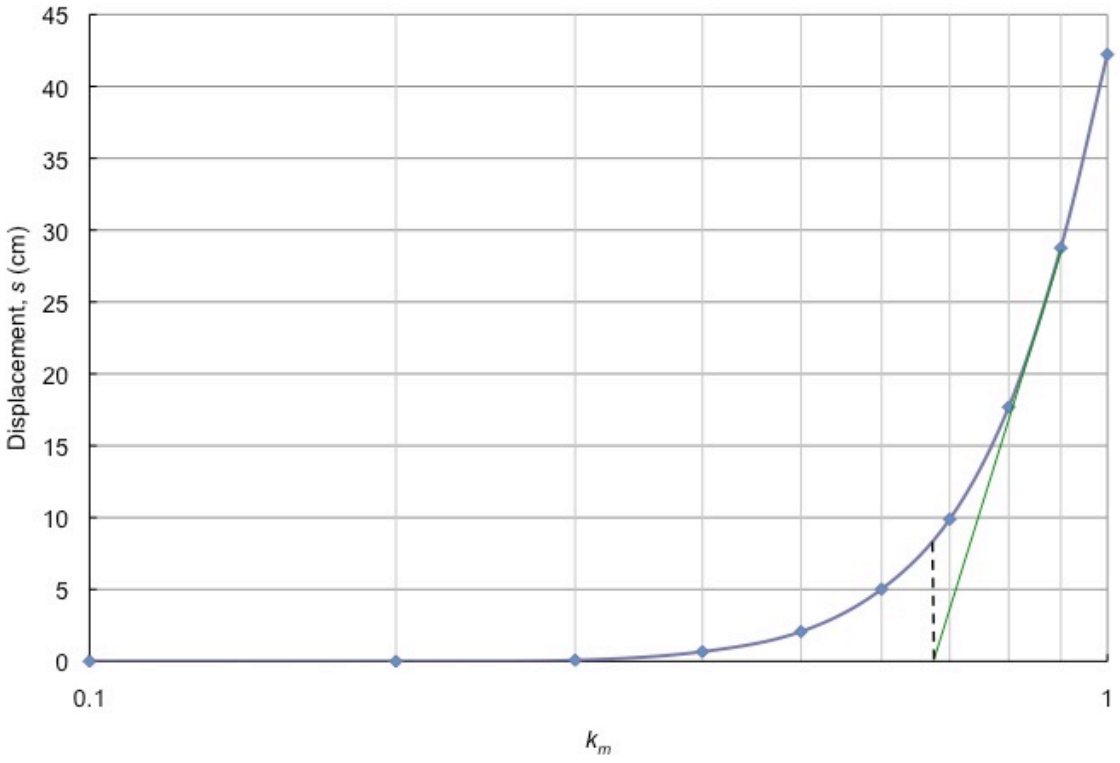

B.37. Permanent displacement calculated for the negative orientation of the fault-parallel component accelerogram generated at Loma Prieta, USA.

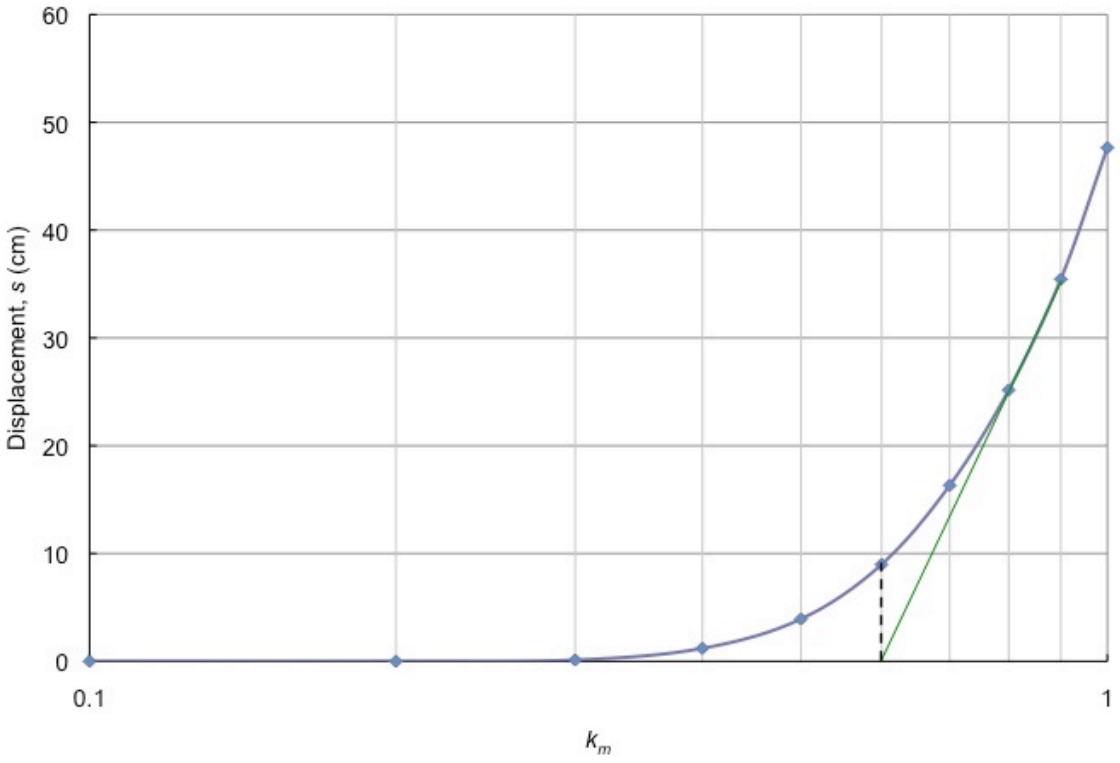

B.38. Permanent displacement calculated for the positive orientation of the fault-parallel component accelerogram generated at Loma Prieta, USA.

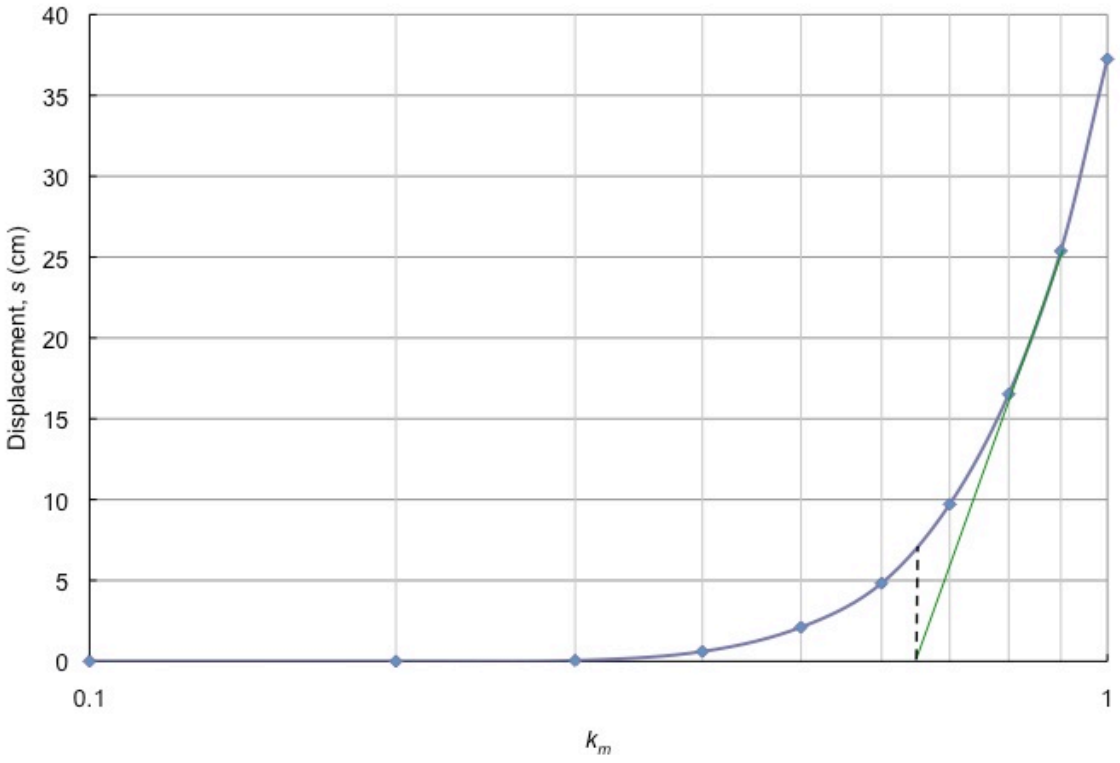

B.39. Permanent displacement calculated for the negative orientation of the fault-parallel component accelerogram generated at Loma Prieta, USA.

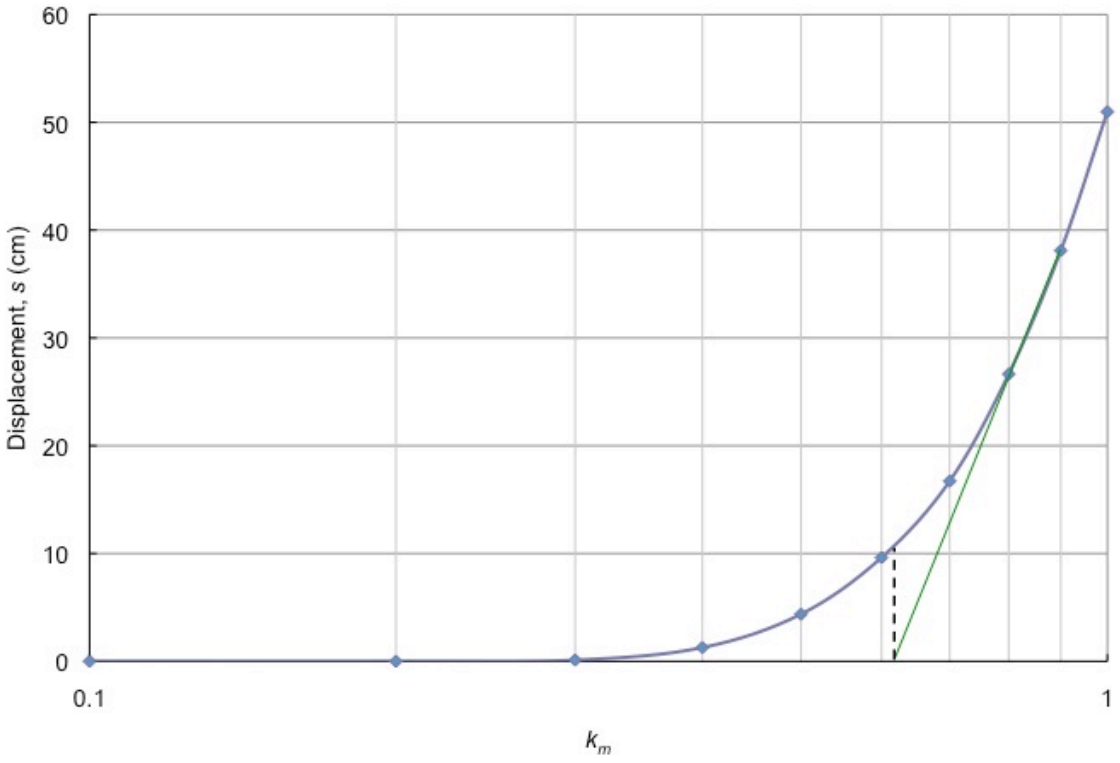

B.40. Permanent displacement calculated for the positive orientation of the fault-parallel component accelerogram generated at Loma Prieta, USA.

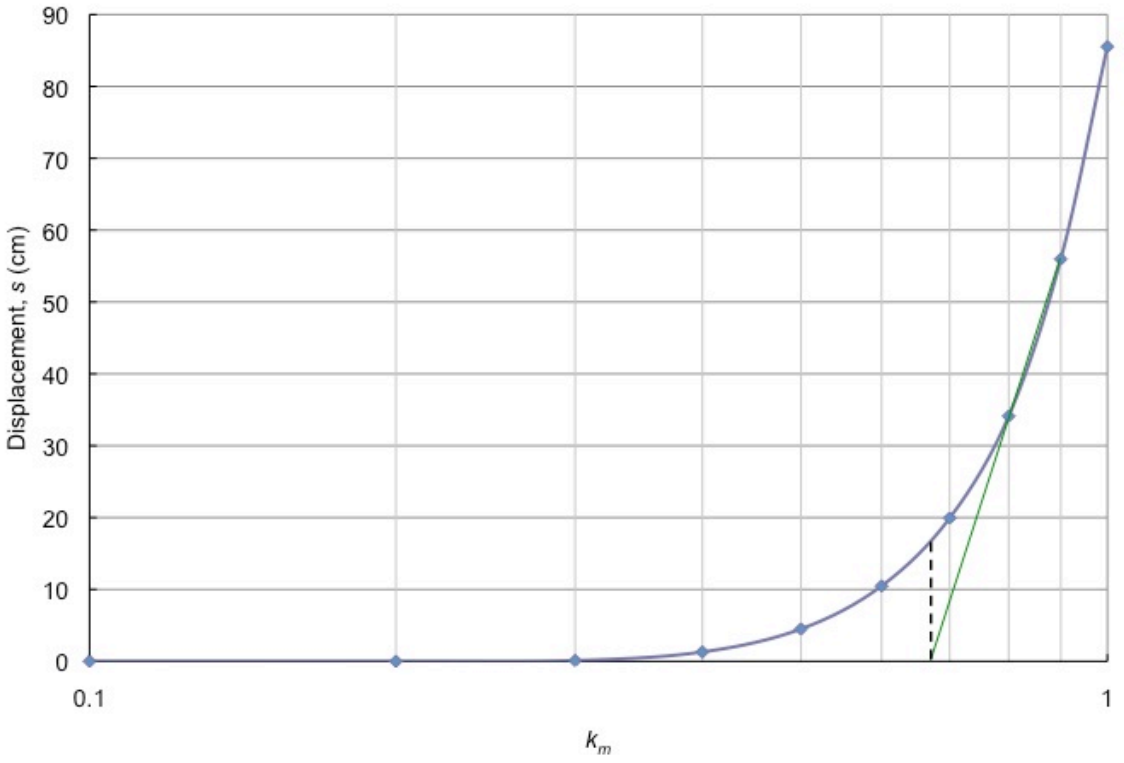

B.41. Permanent displacement calculated for the negative orientation of the fault-parallel component accelerogram generated at Taiwan.

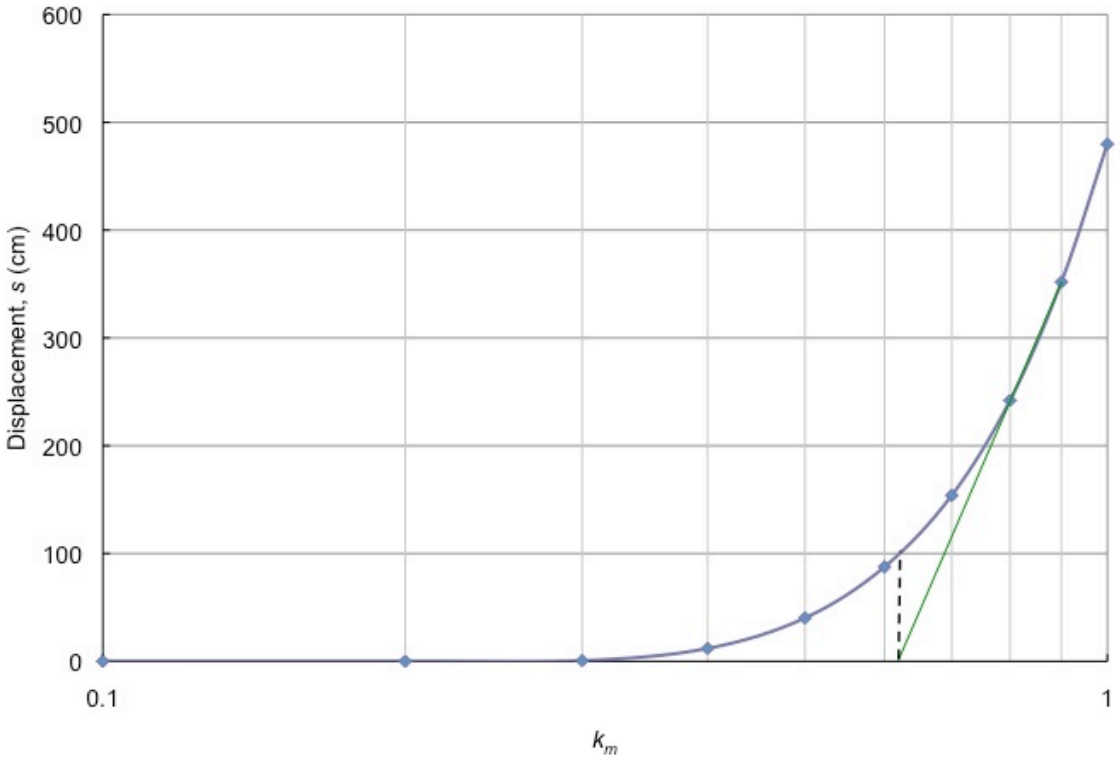

B.42. Permanent displacement calculated for the positive orientation of the fault-parallel component accelerogram generated at Taiwan.

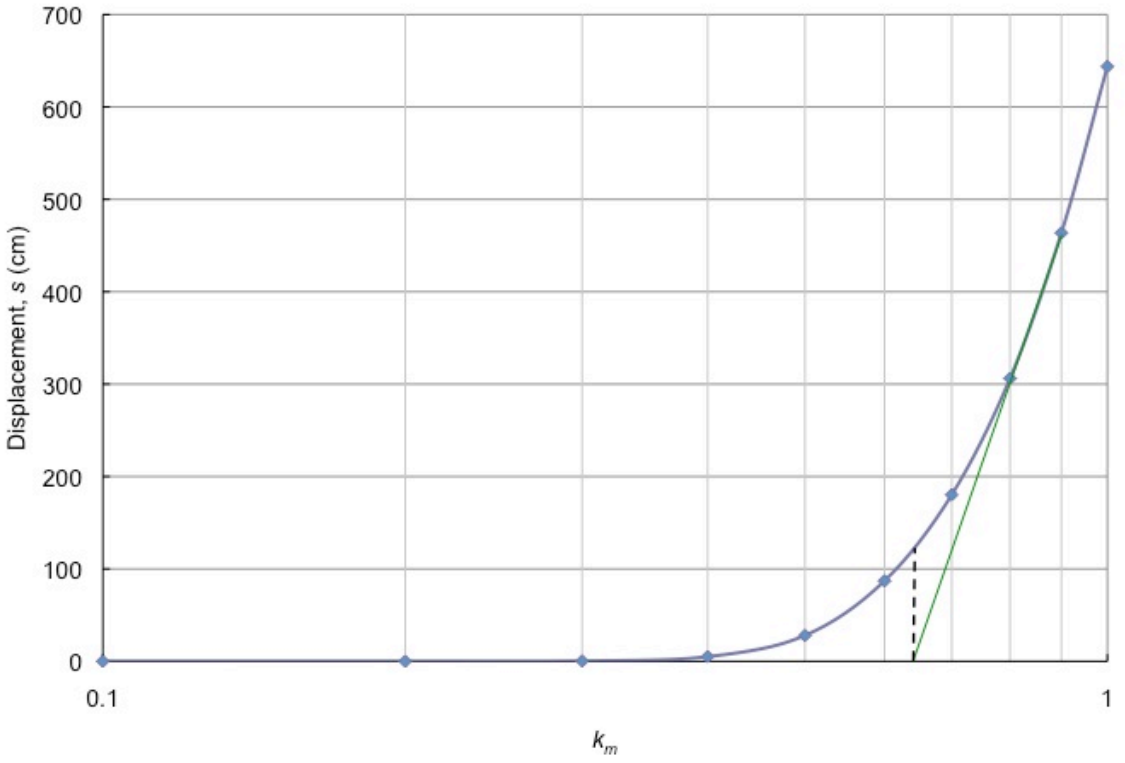

B.43. Permanent displacement calculated for the negative orientation of the fault-parallel component accelerogram generated at Taiwan.

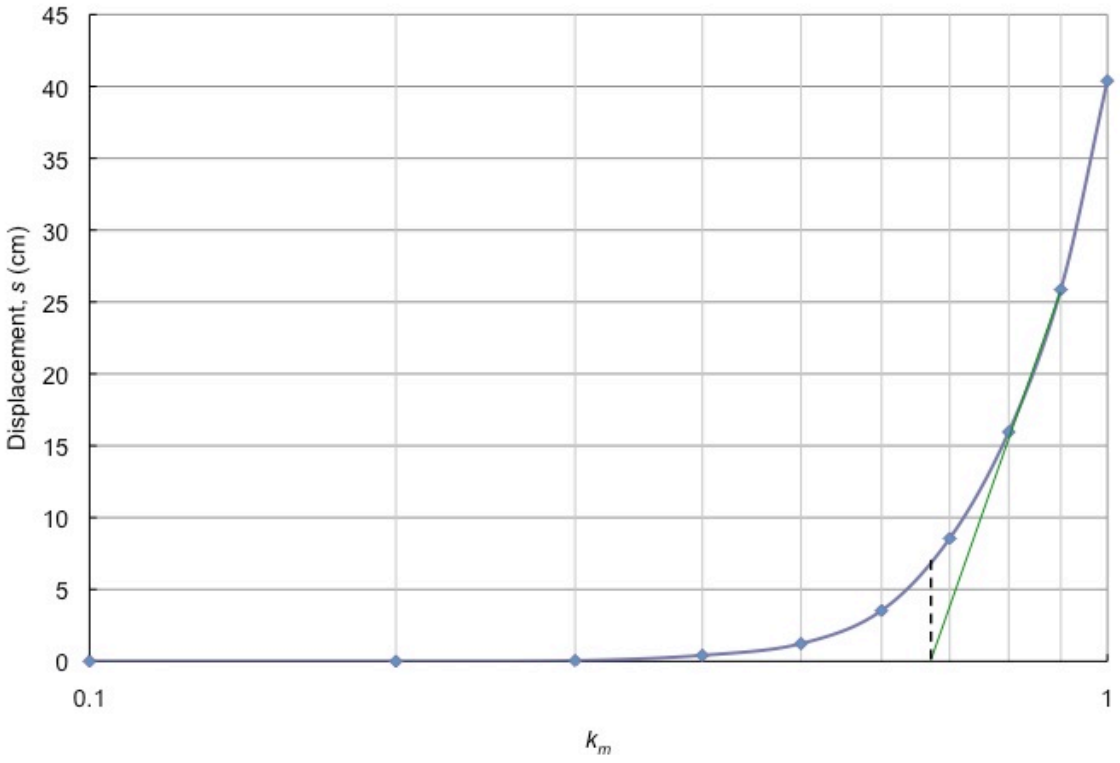

B.44. Permanent displacement calculated for the positive orientation of the fault-parallel component accelerogram generated at Taiwan.

Normal-Faulting Earthquakes in Partially

Saturated Conditions

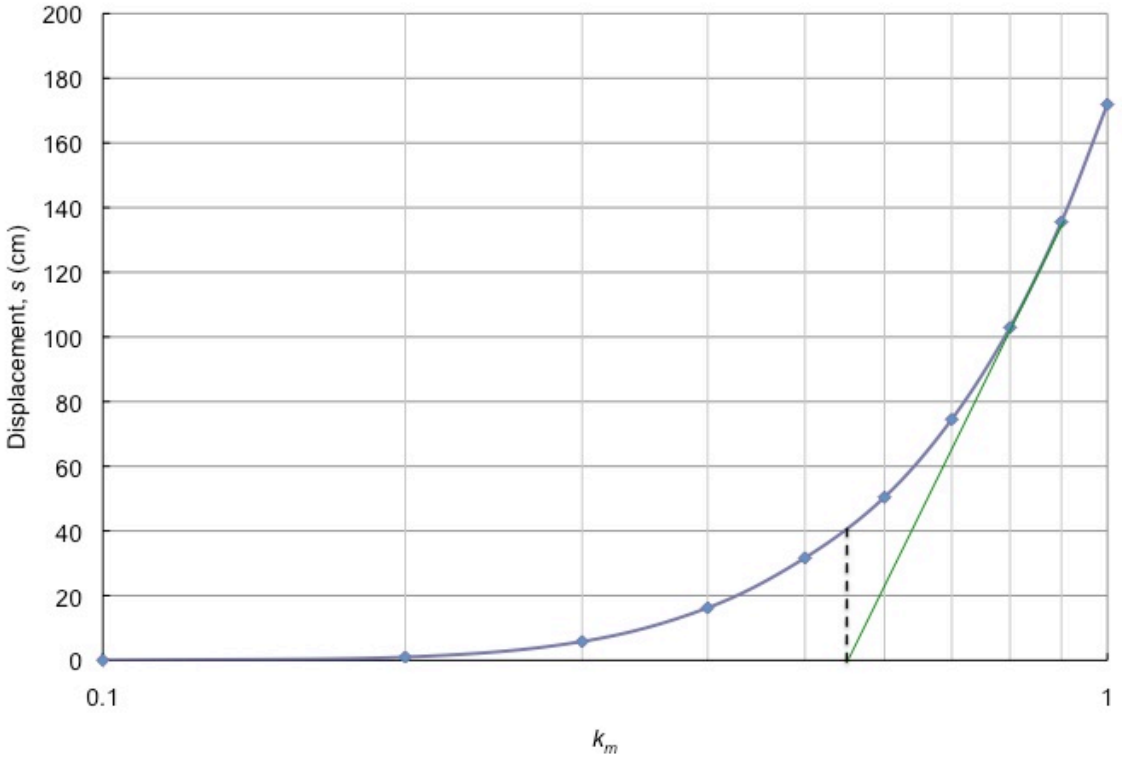

B.45. Permanent displacement calculated for the negative orientation of the fault-normal component accelerogram generated at Auletta, Italy.

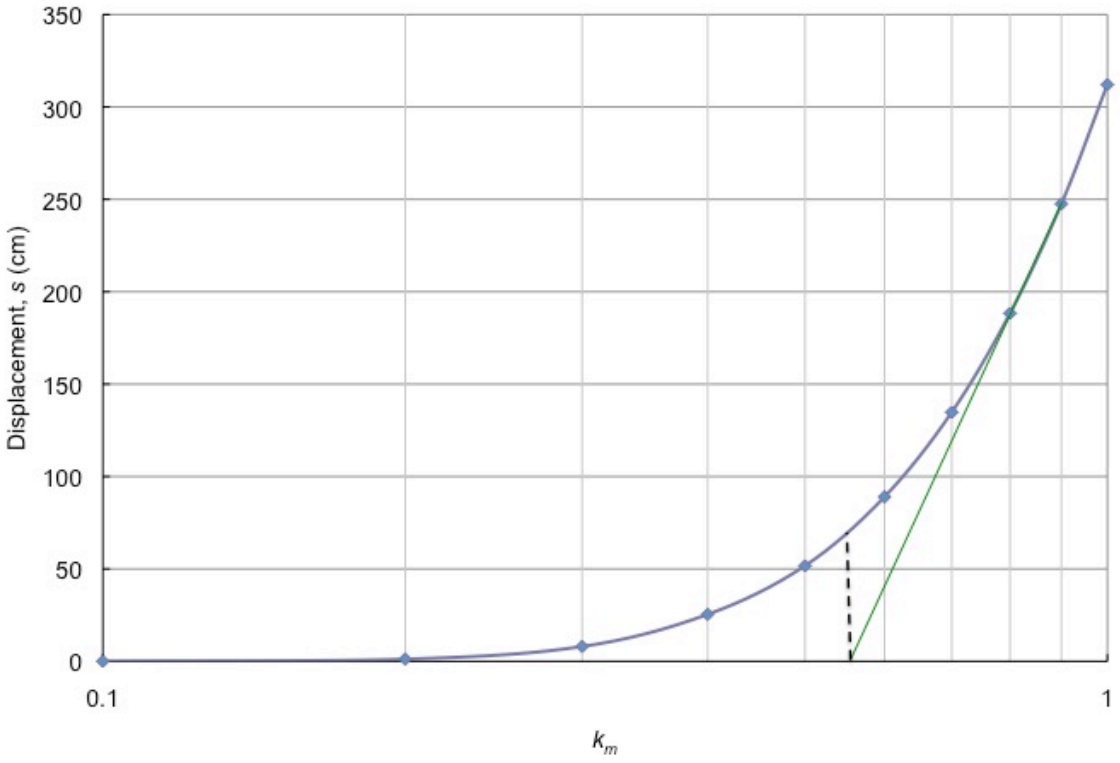

B.46. Permanent displacement calculated for the positive orientation of the fault-normal component accelerogram generated at Auletta, Italy.

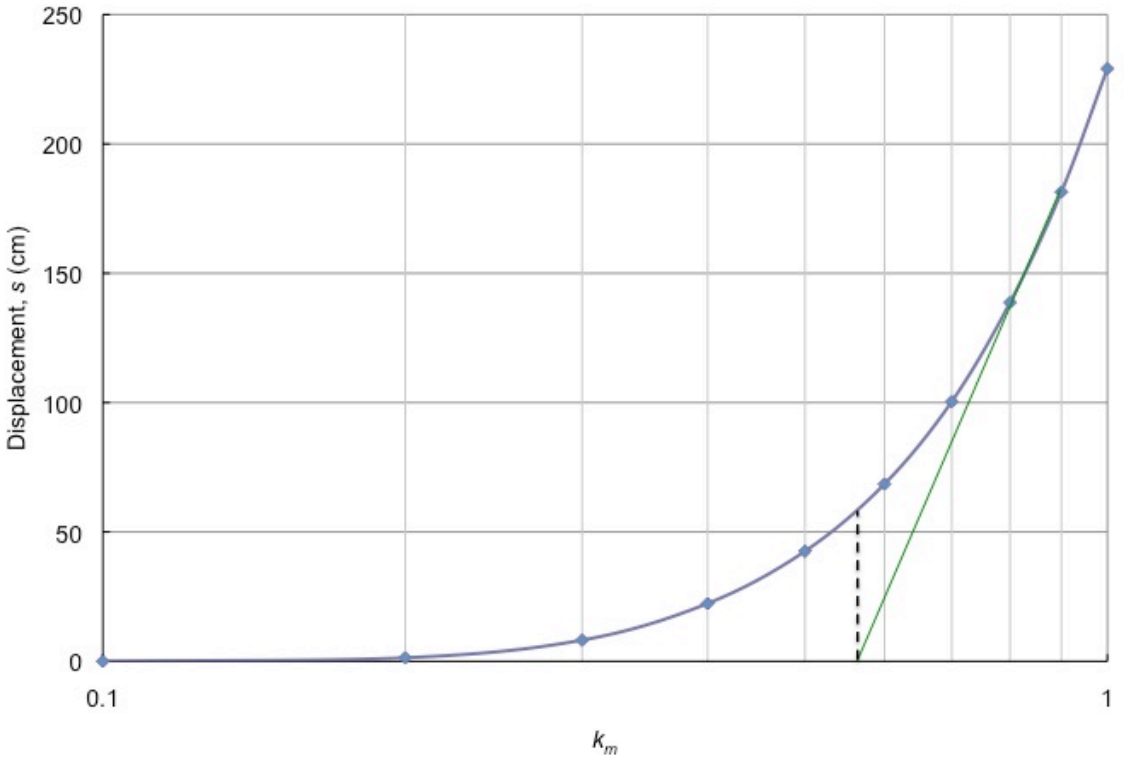

B.47. Permanent displacement calculated for the negative orientation of the fault-parallel component accelerogram generated at Auletta, Italy.

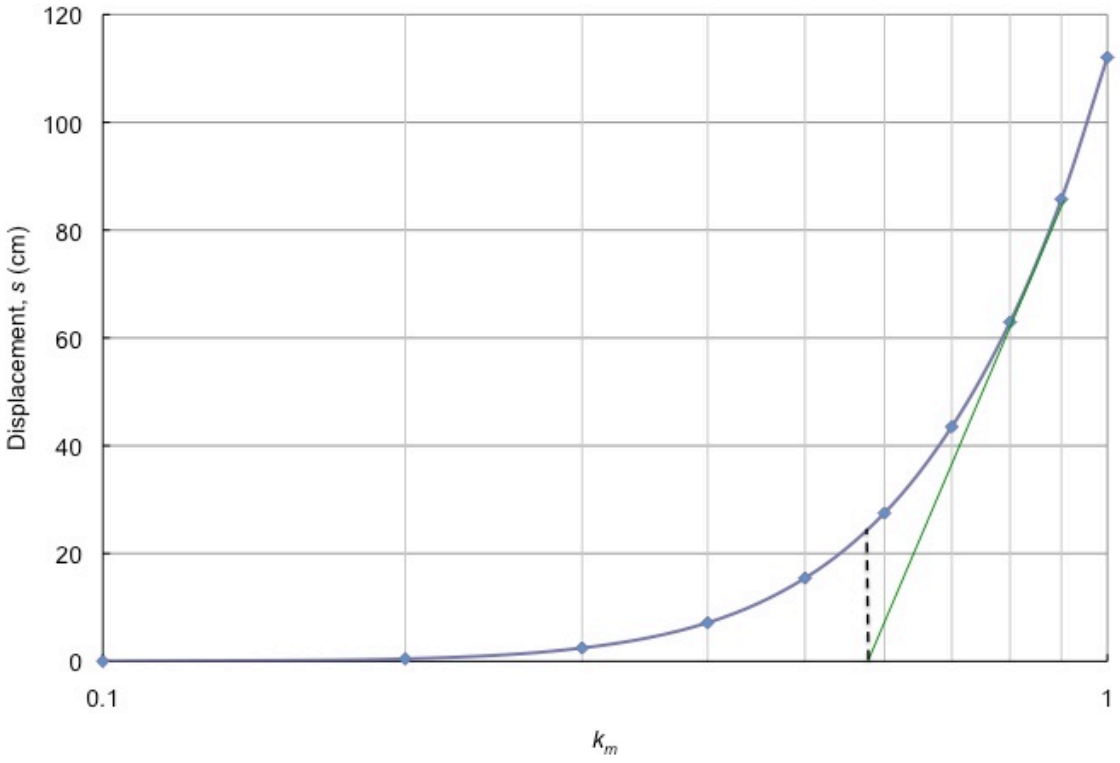

B.48. Permanent displacement calculated for the positive orientation of the fault-parallel component accelerogram generated at Auletta, Italy.

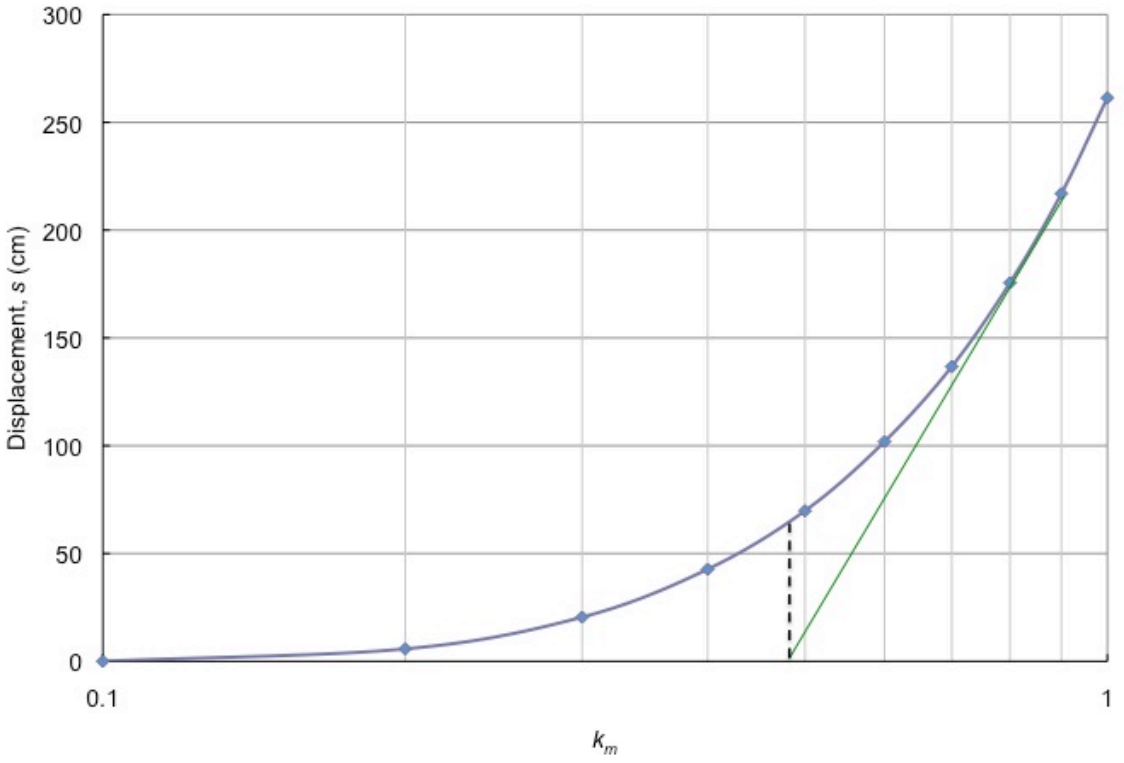

B.49. Permanent displacement calculated for the negative orientation of the fault-normal component accelerogram generated at Bagnoli, Italy.

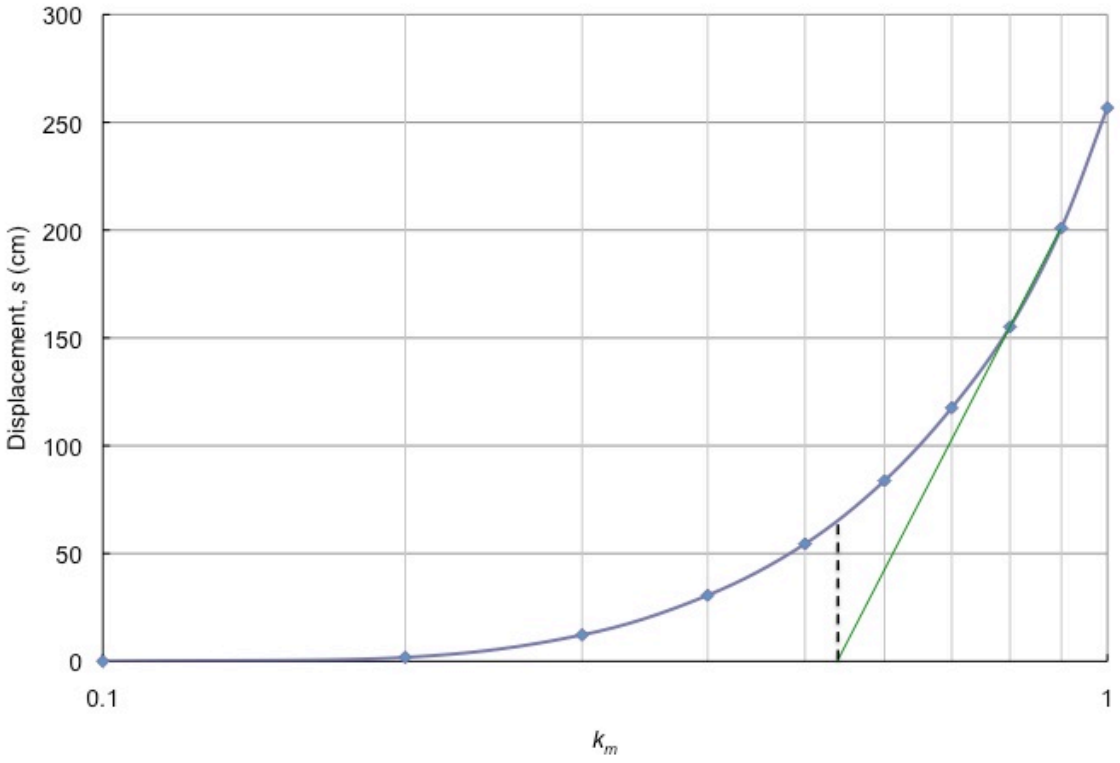

B.50. Permanent displacement calculated for the positive orientation of the fault-normal component accelerogram generated at Bagnoli, Italy.

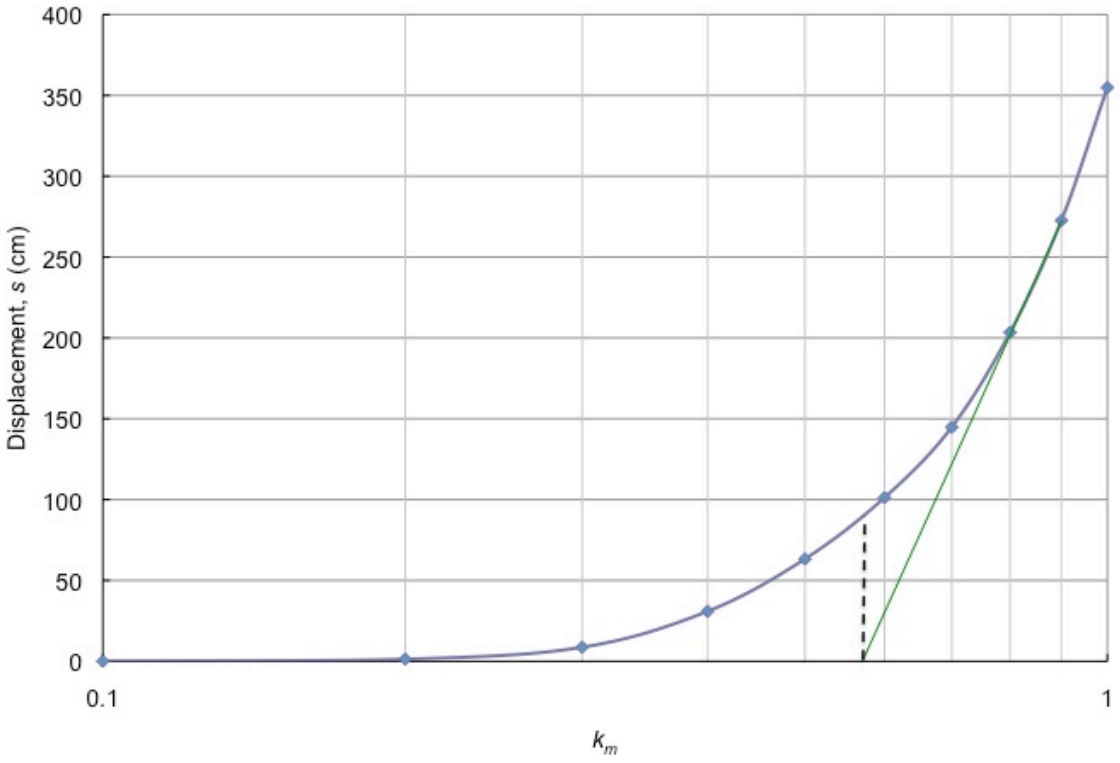

B.51. Permanent displacement calculated for the negative orientation of the fault-parallel component accelerogram generated at Bagnoli, Italy.

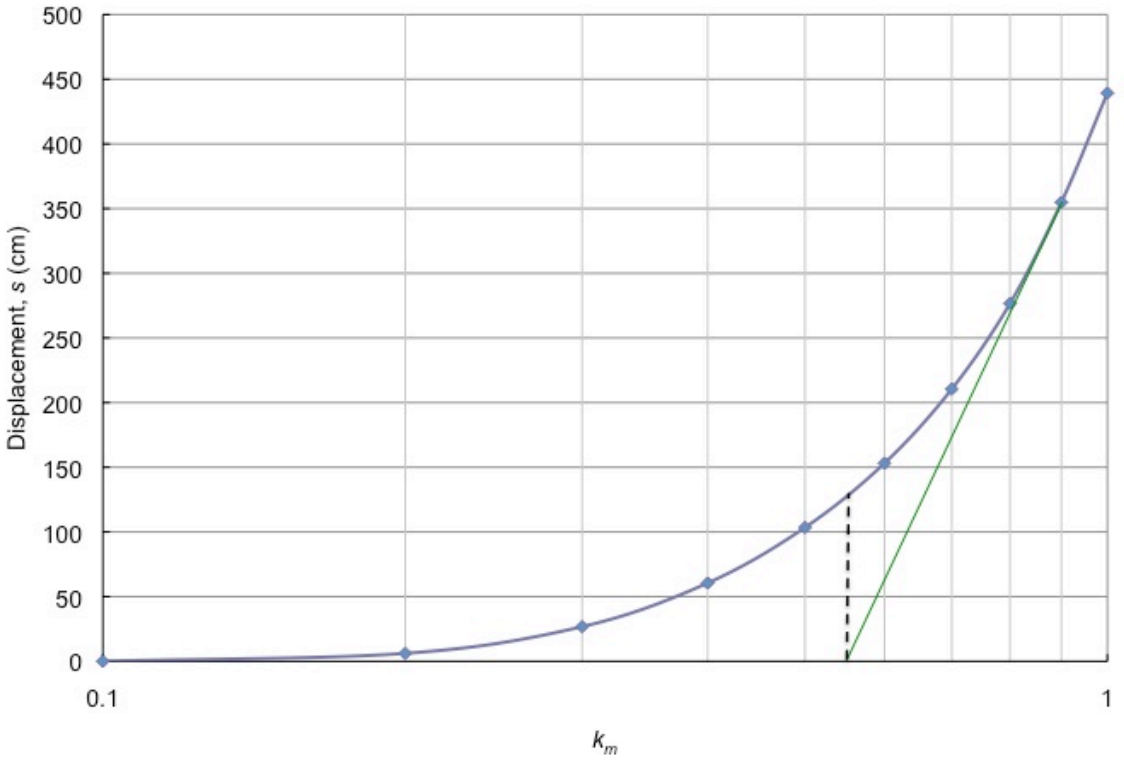

B.52. Permanent displacement calculated for the positive orientation of the fault-parallel component accelerogram generated at Bagnoli, Italy.

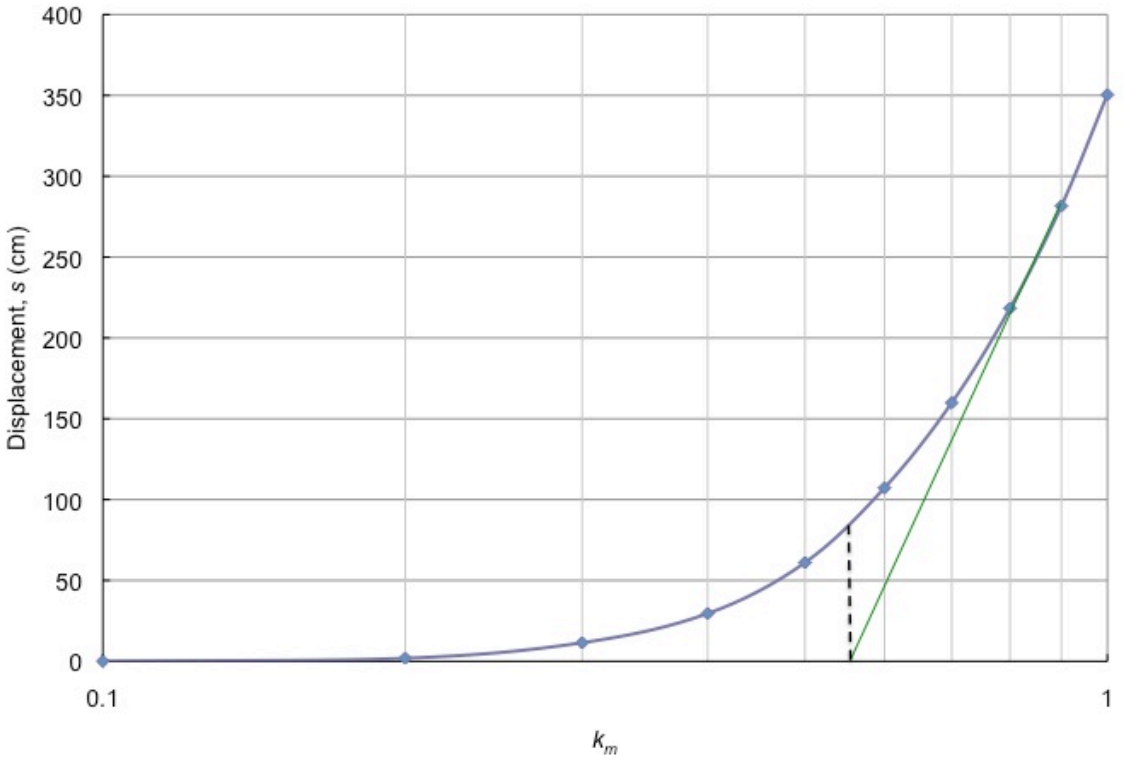

B.53. Permanent displacement calculated for the negative orientation of the fault-normal component accelerogram generated at Sturno, Italy.

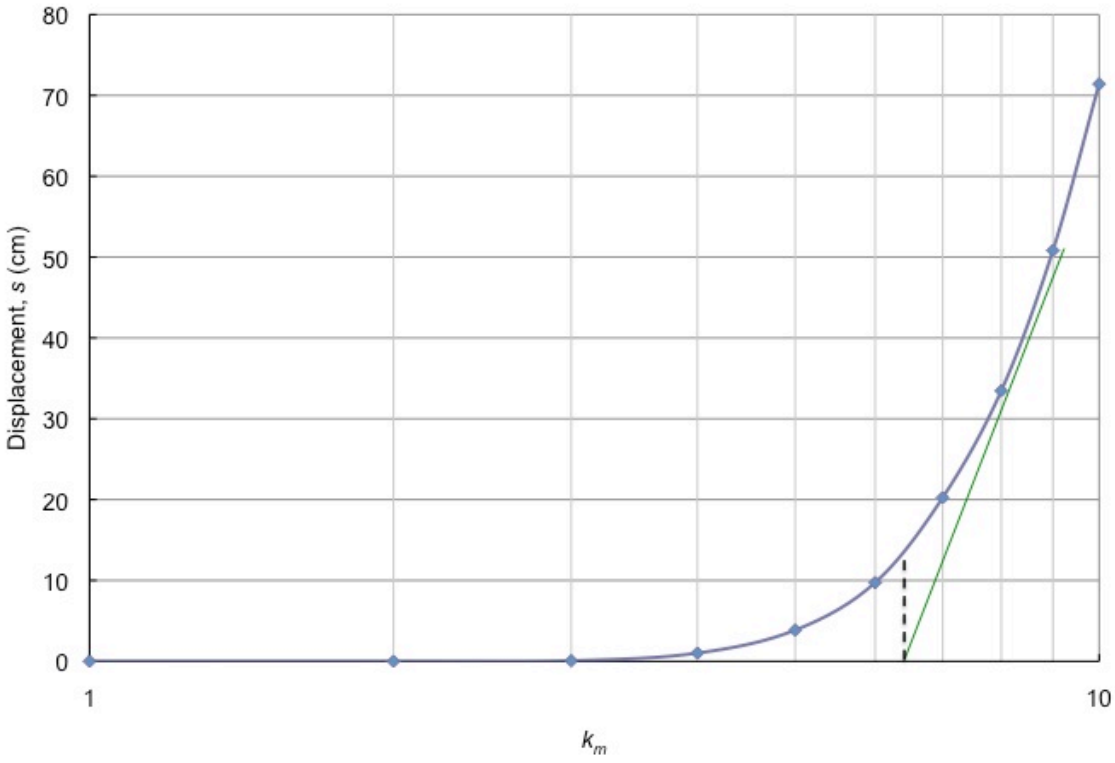

B.54. Permanent displacement calculated for the positive orientation of the fault-normal component accelerogram generated at Sturno, Italy.

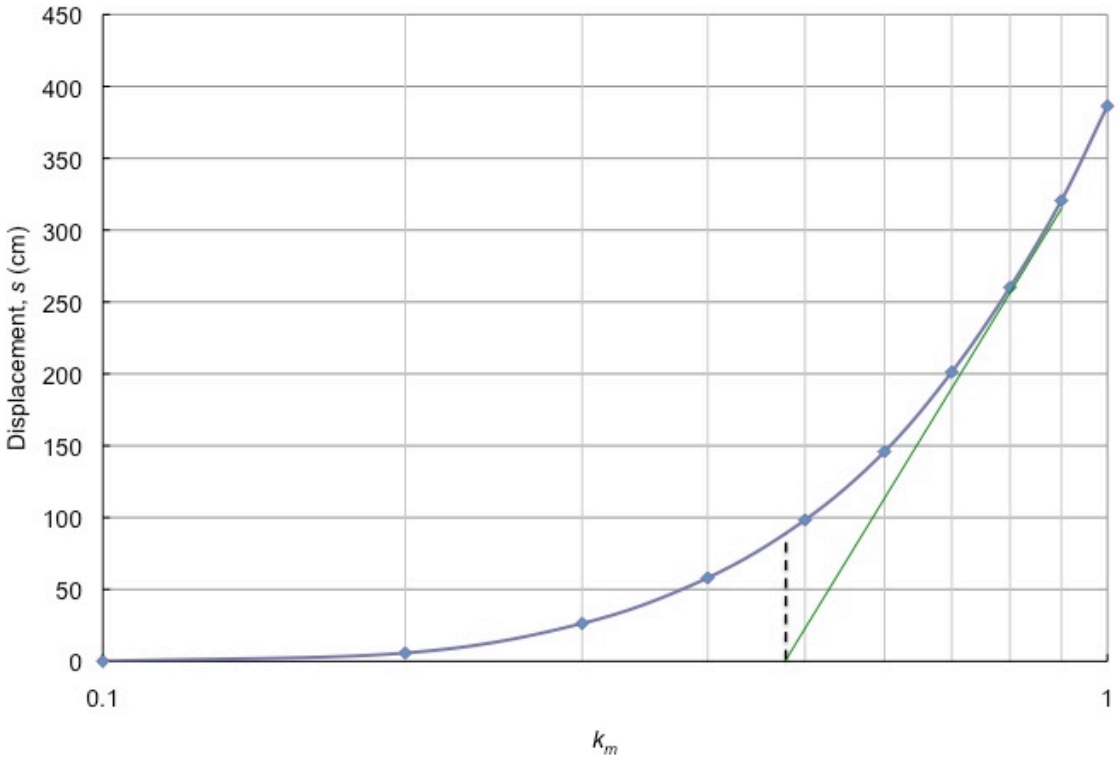

B.55. Permanent displacement calculated for the negative orientation of the fault-parallel component accelerogram generated at Sturno, Italy.

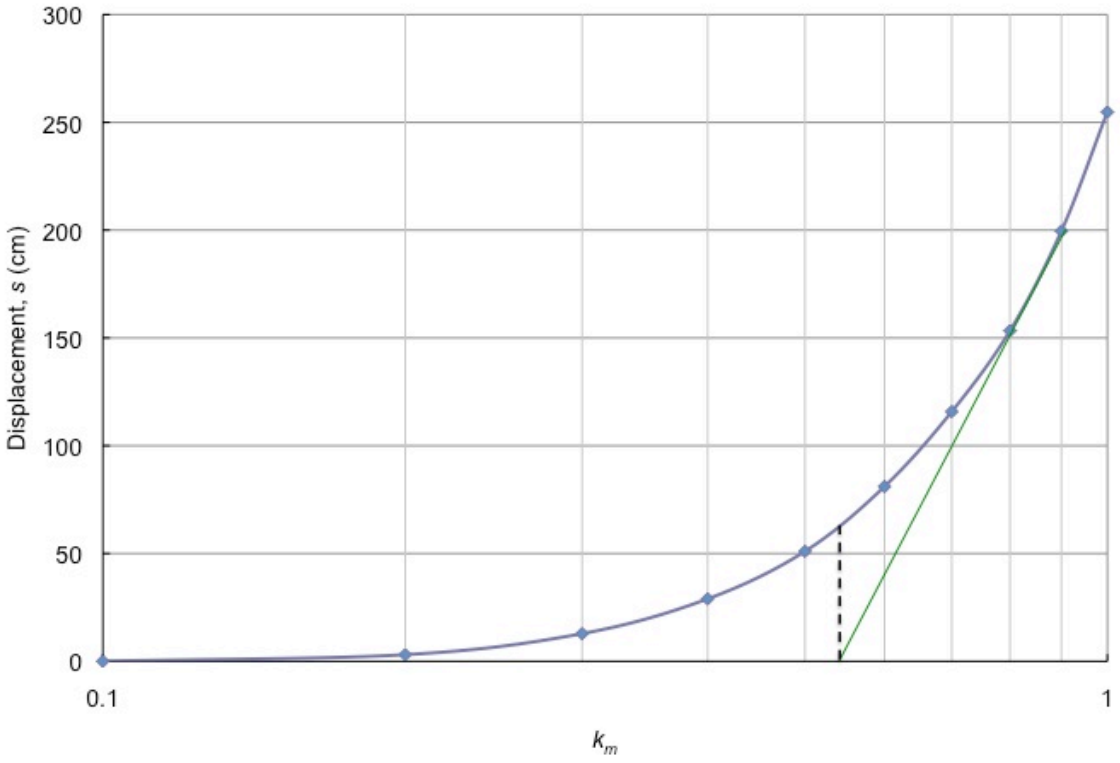

B.56. Permanent displacement calculated for the positive orientation of the fault-parallel component accelerogram generated at Sturno, Italy.

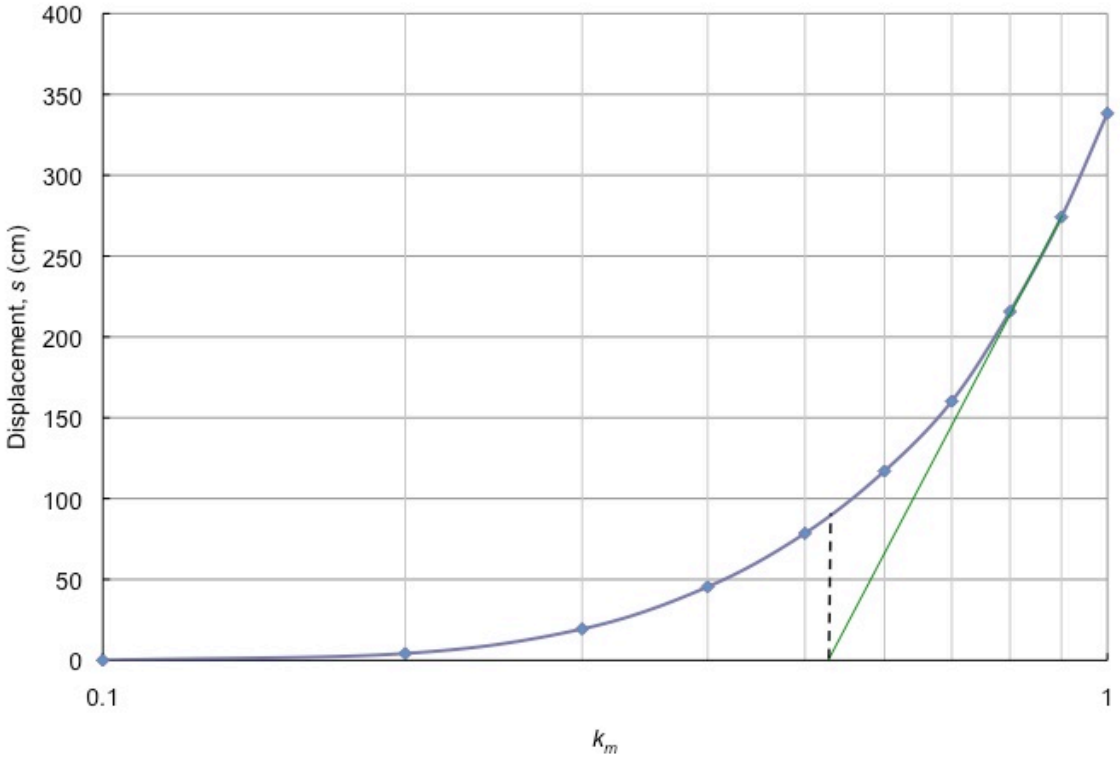

B.57. Permanent displacement calculated for the negative orientation of the fault-normal component accelerogram generated at Kocaeli, Italy.

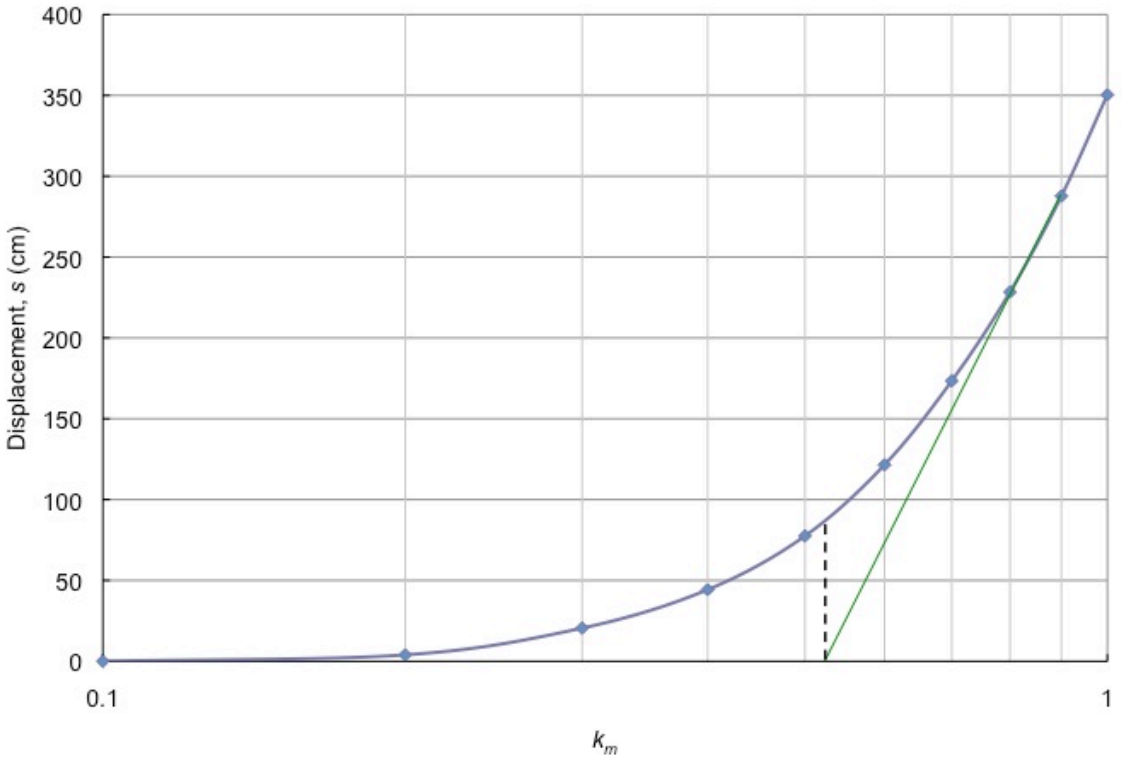

B.58. Permanent displacement calculated for the positive orientation of the fault-normal component accelerogram generated at Kocaeli, Italy.

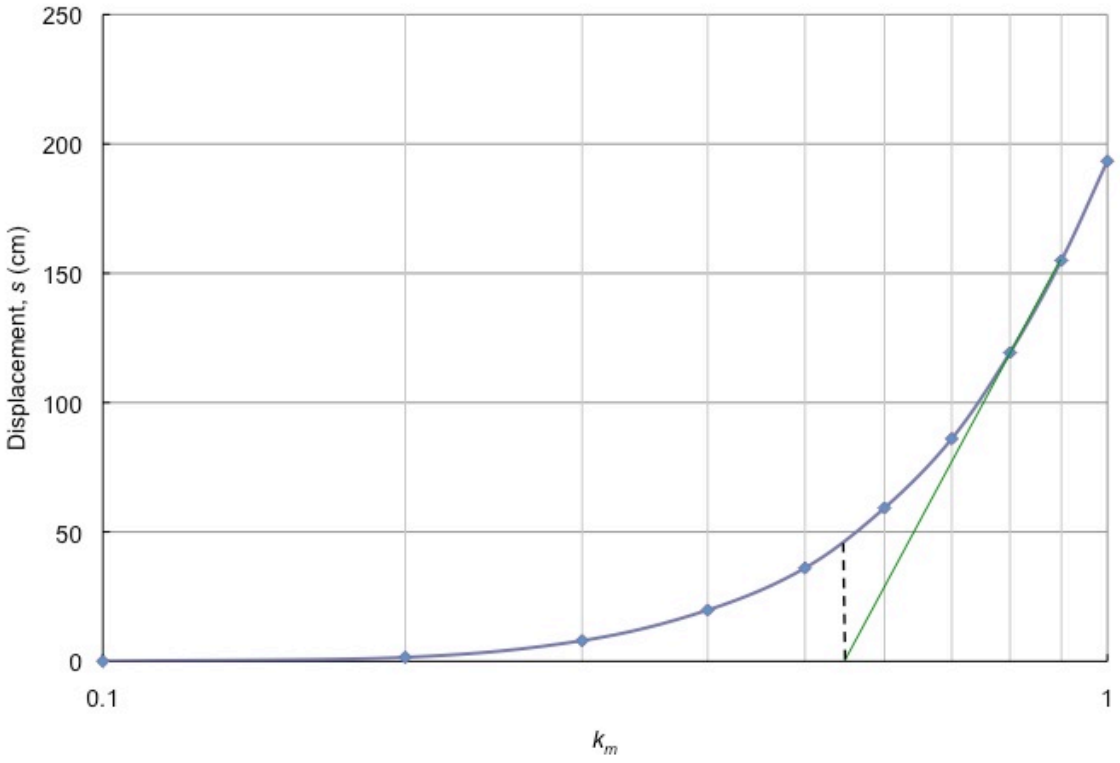

B.59. Permanent displacement calculated for the negative orientation of the fault-parallel component accelerogram generated at Kocaeli, Italy.

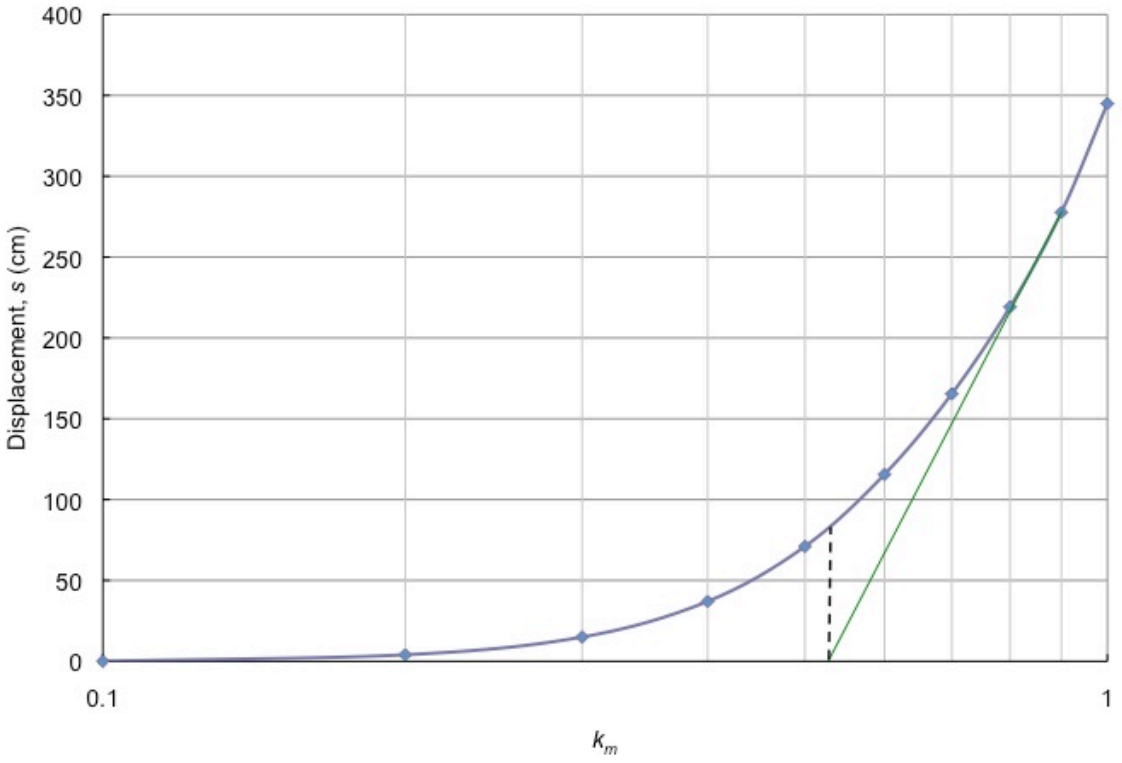

B.60. Permanent displacement calculated for the positive orientation of the fault-parallel component accelerogram generated at Kocaeli, Italy.

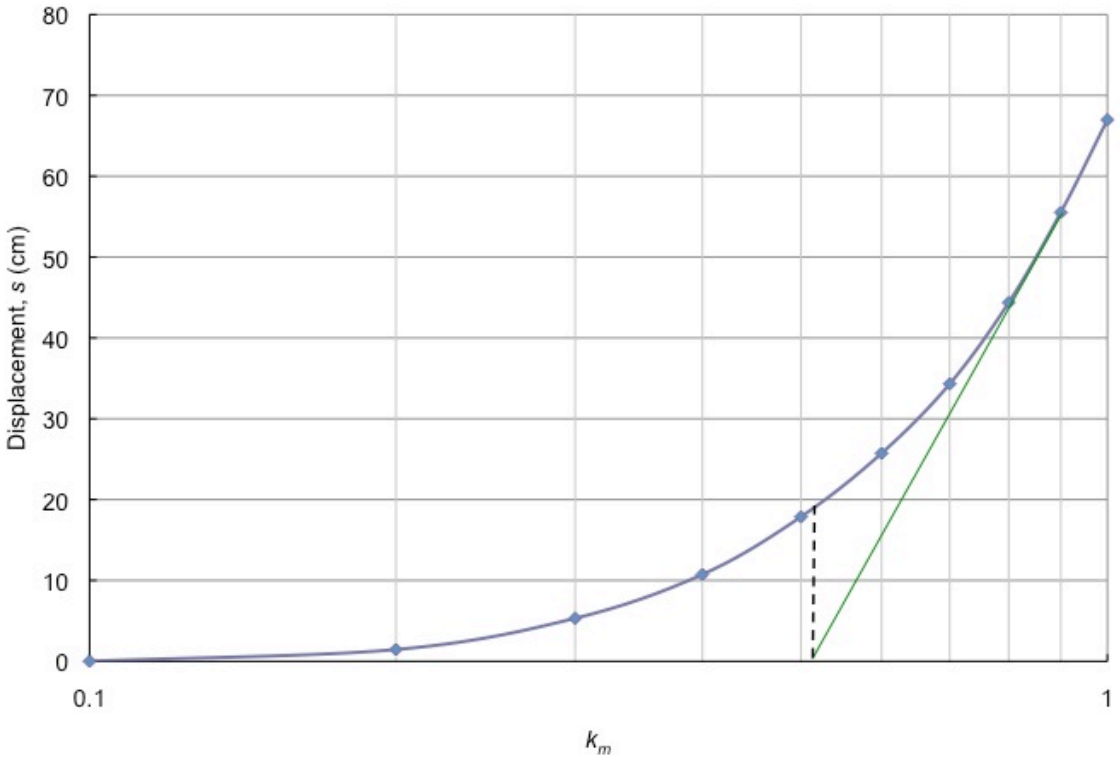

B.61. Permanent displacement calculated for the negative orientation of the fault-normal component accelerogram generated at Loma Prieta, USA.

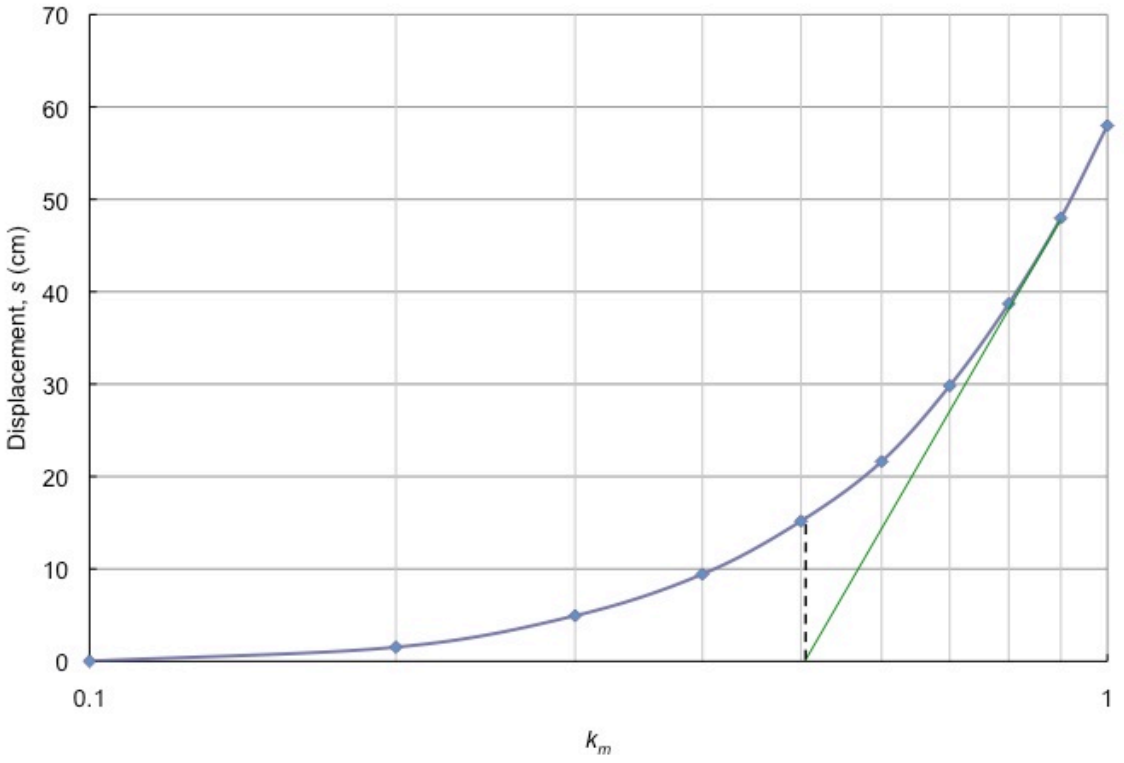

B.62. Permanent displacement calculated for the positive orientation of the fault-normal component accelerogram generated at Loma Prieta, USA.

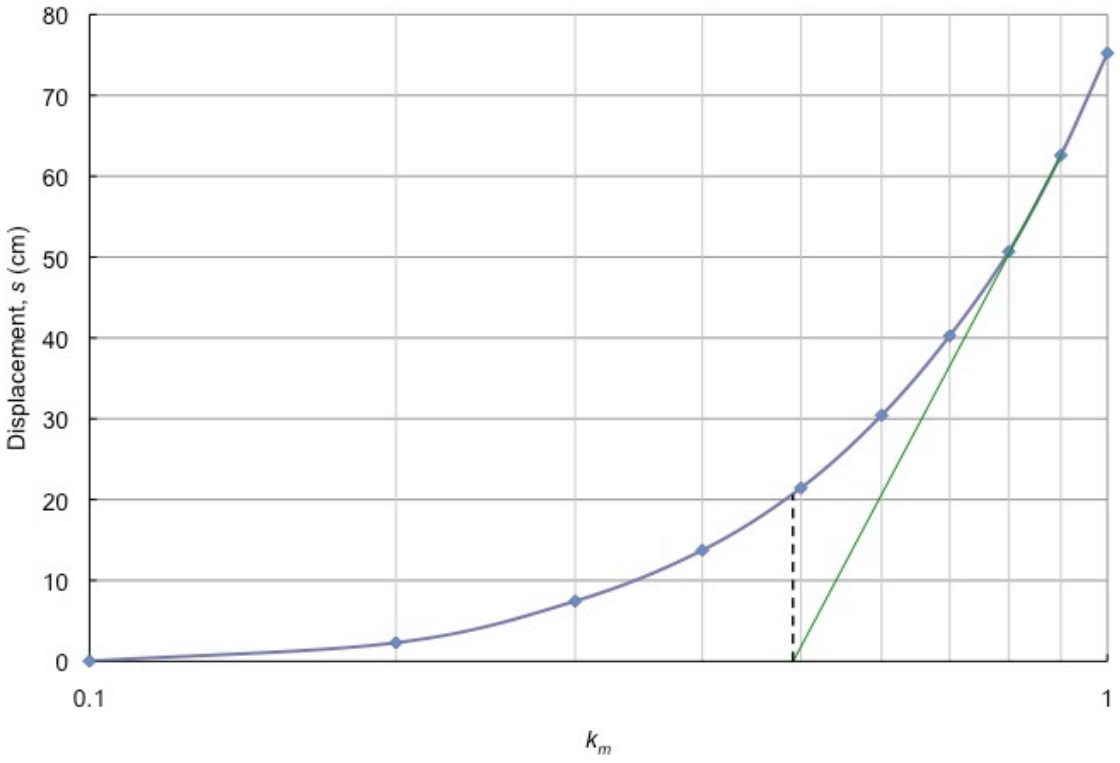

B.63. Permanent displacement calculated for the negative orientation of the fault-parallel component accelerogram generated at Loma Prieta, USA.

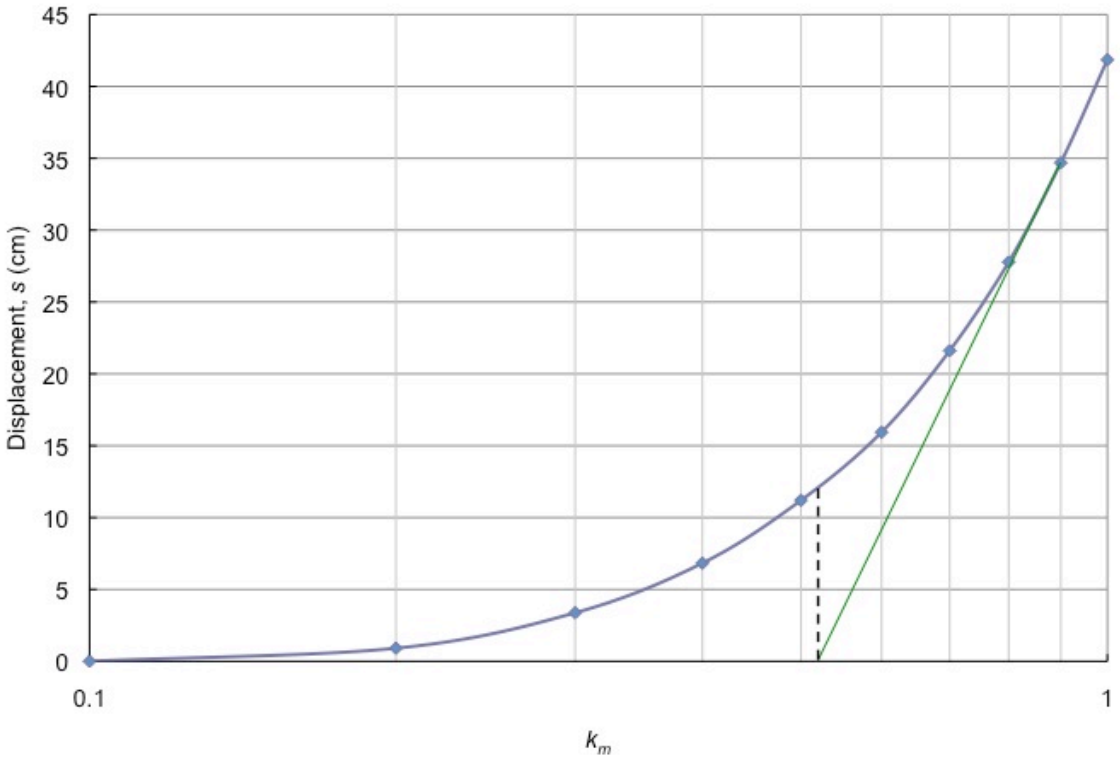

B.64. Permanent displacement calculated for the positive orientation of the fault-parallel component accelerogram generated at Loma Prieta, USA.

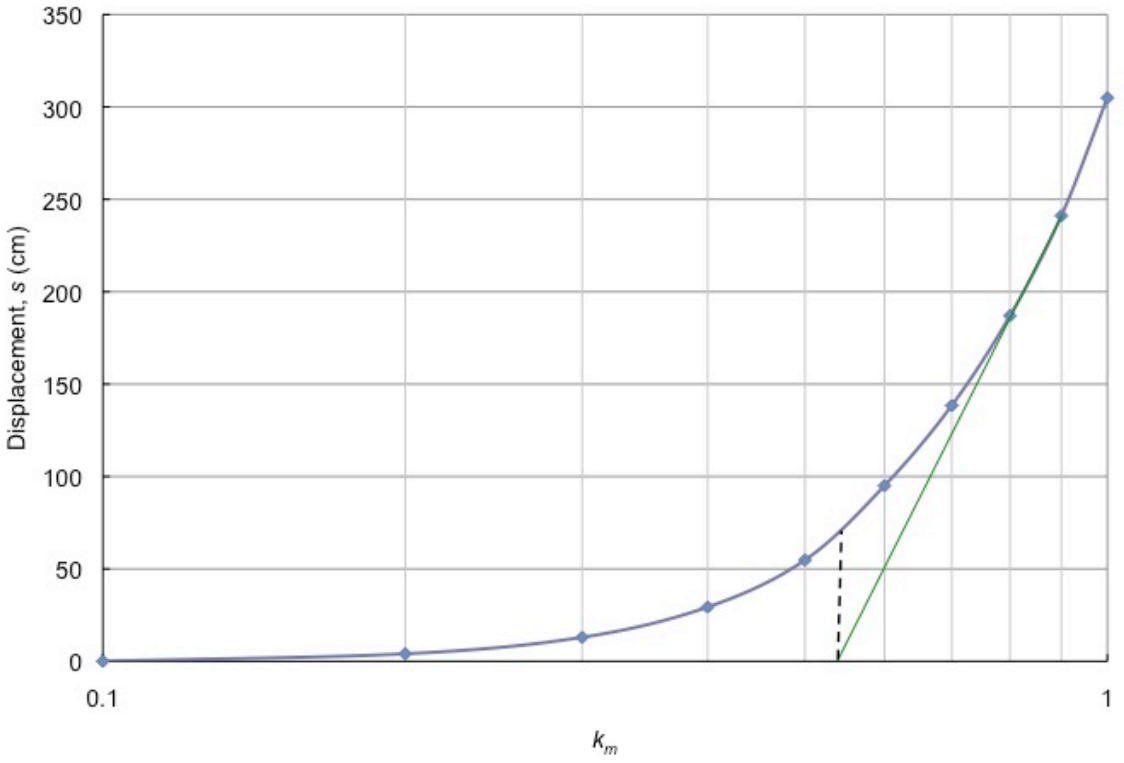

B.65. Permanent displacement calculated for the negative orientation of the fault-normal component accelerogram generated at Tabas, Iran.

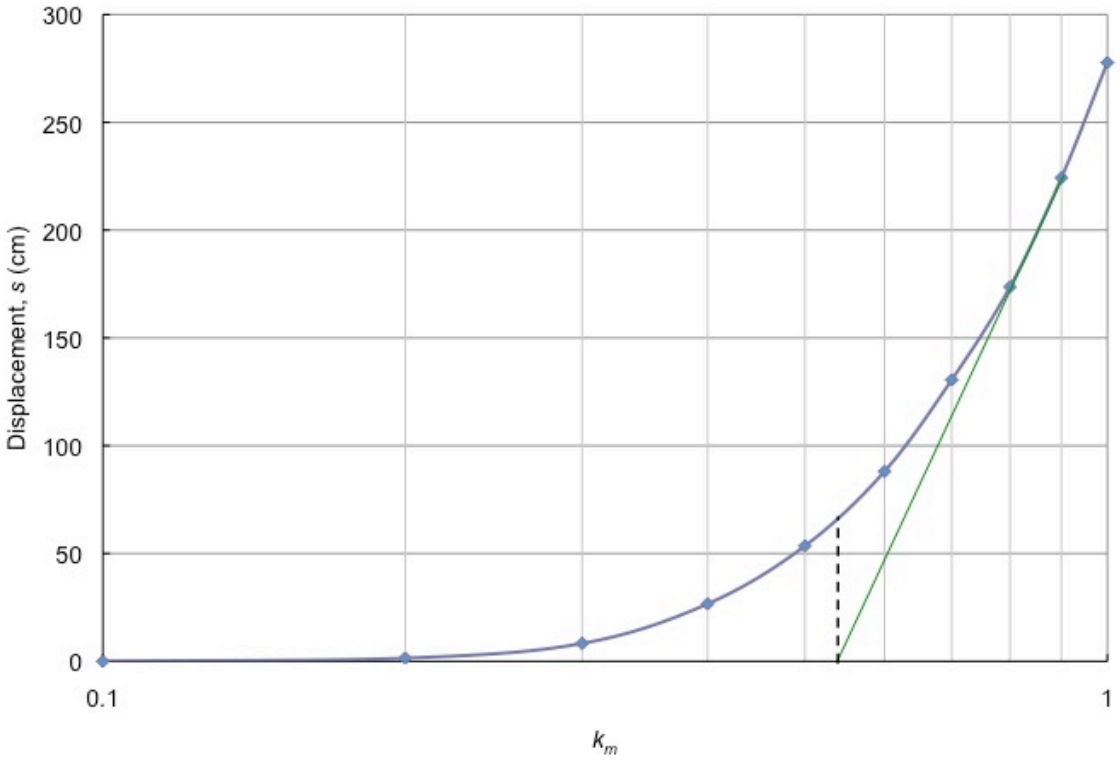

B.66. Permanent displacement calculated for the positive orientation of the fault-normal component accelerogram generated at Tabas, Iran.

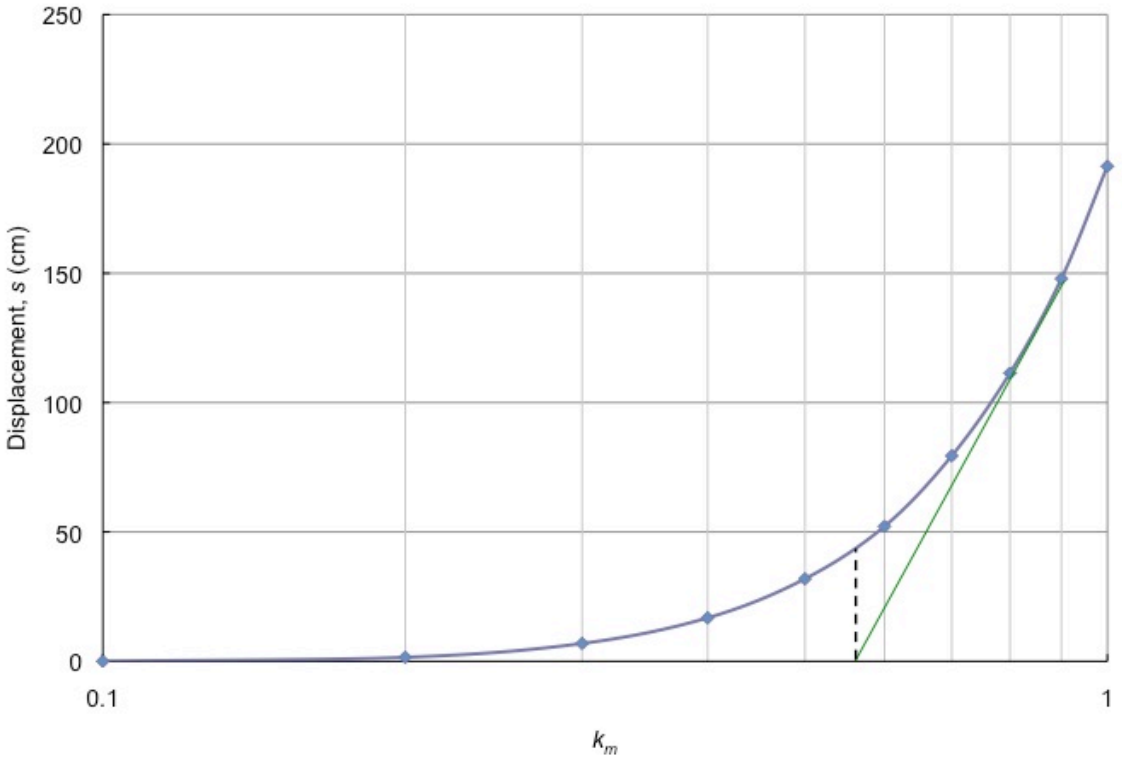

B.67. Permanent displacement calculated for the negative orientation of the fault-parallel component accelerogram generated at Tabas, Iran.

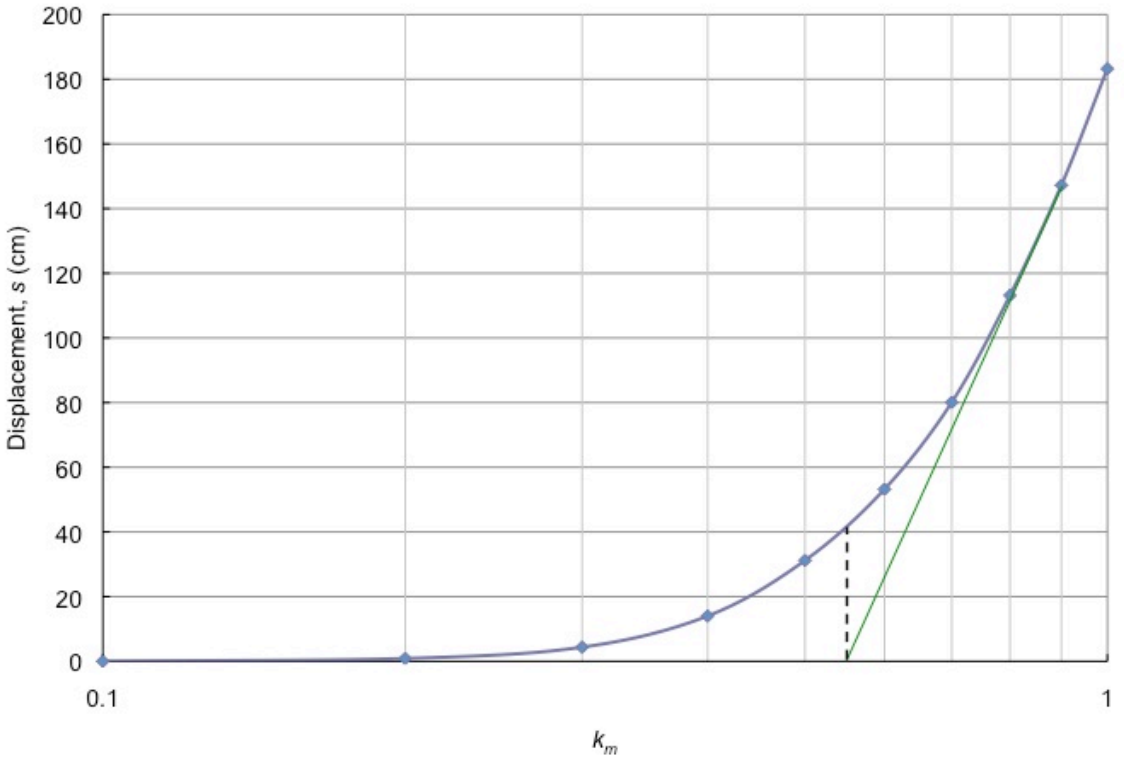

B.68. Permanent displacement calculated for the positive orientation of the fault-parallel component accelerogram generated at Tabas, Iran.

Seismic Waveforms in Partially

Saturated Conditions

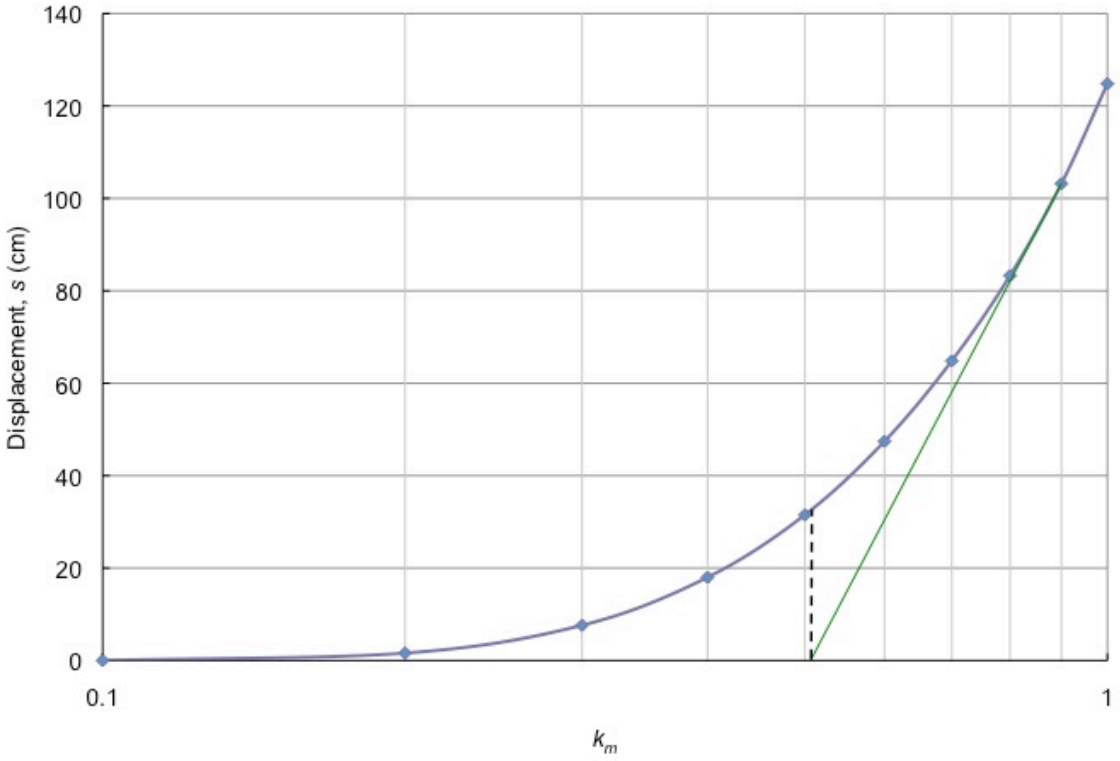

B.69. Permanent displacement calculated for the negative orientation of the fault-normal component accelerogram generated at Chuetsu, Japan.

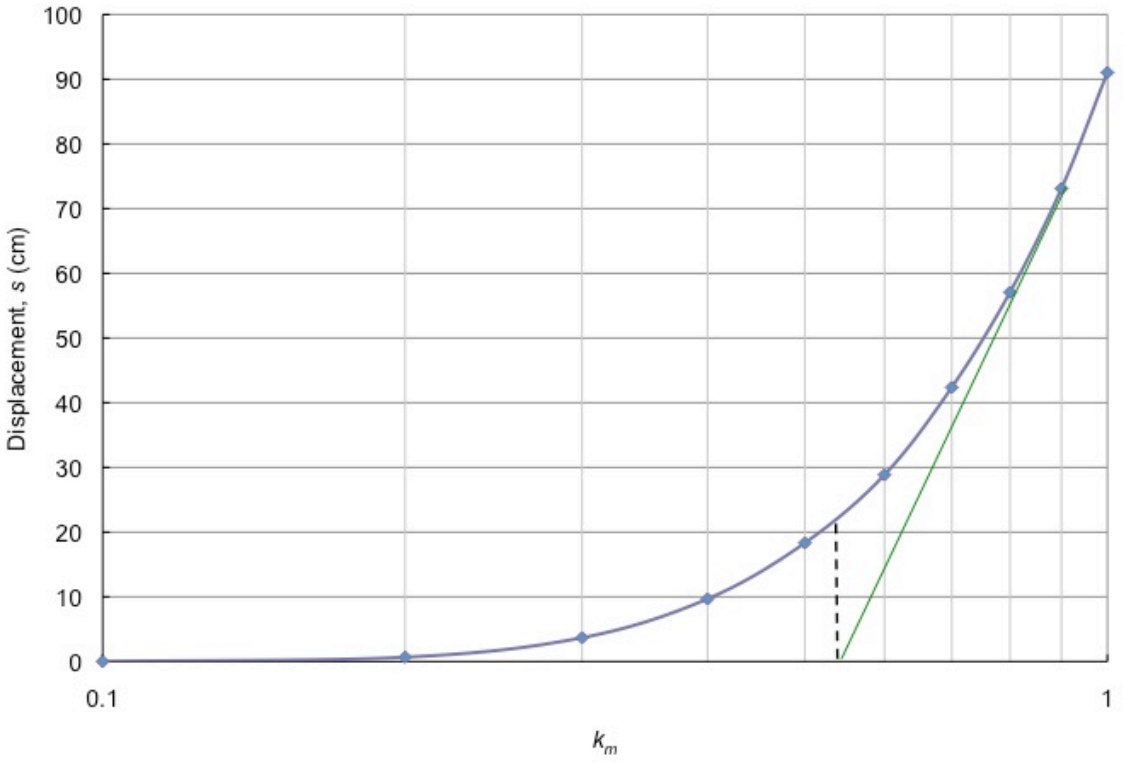

B.70. Permanent displacement calculated for the positive orientation of the fault-normal component accelerogram generated at Chuetsu, Japan.

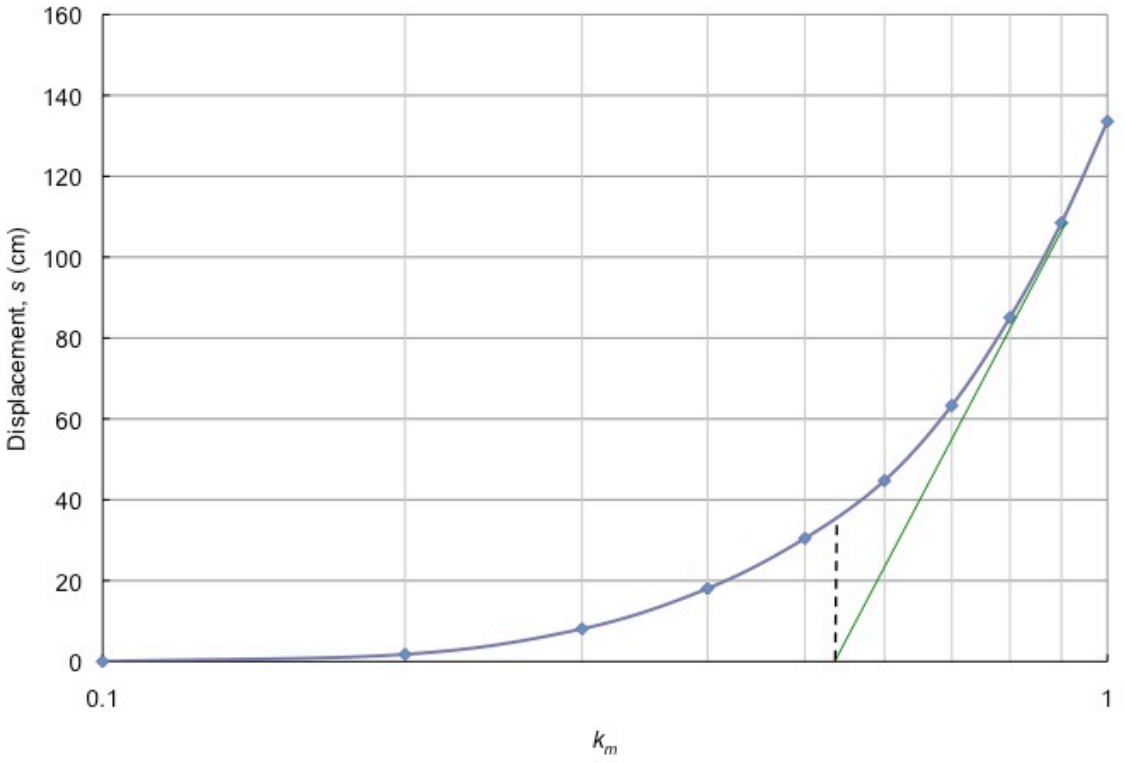

B.71. Permanent displacement calculated for the negative orientation of the fault-parallel component accelerogram generated at Chuetsu, Japan.

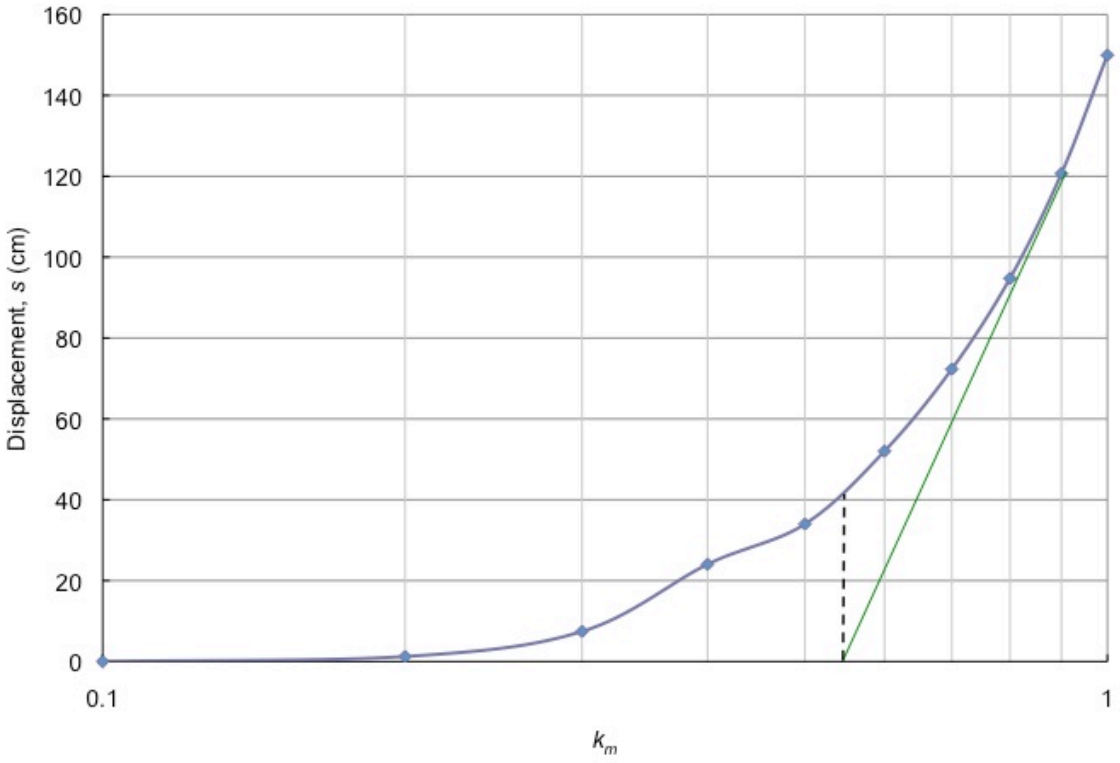

B.72. Permanent displacement calculated for the positive orientation of the fault-parallel component accelerogram generated at Chuetsu, Japan.

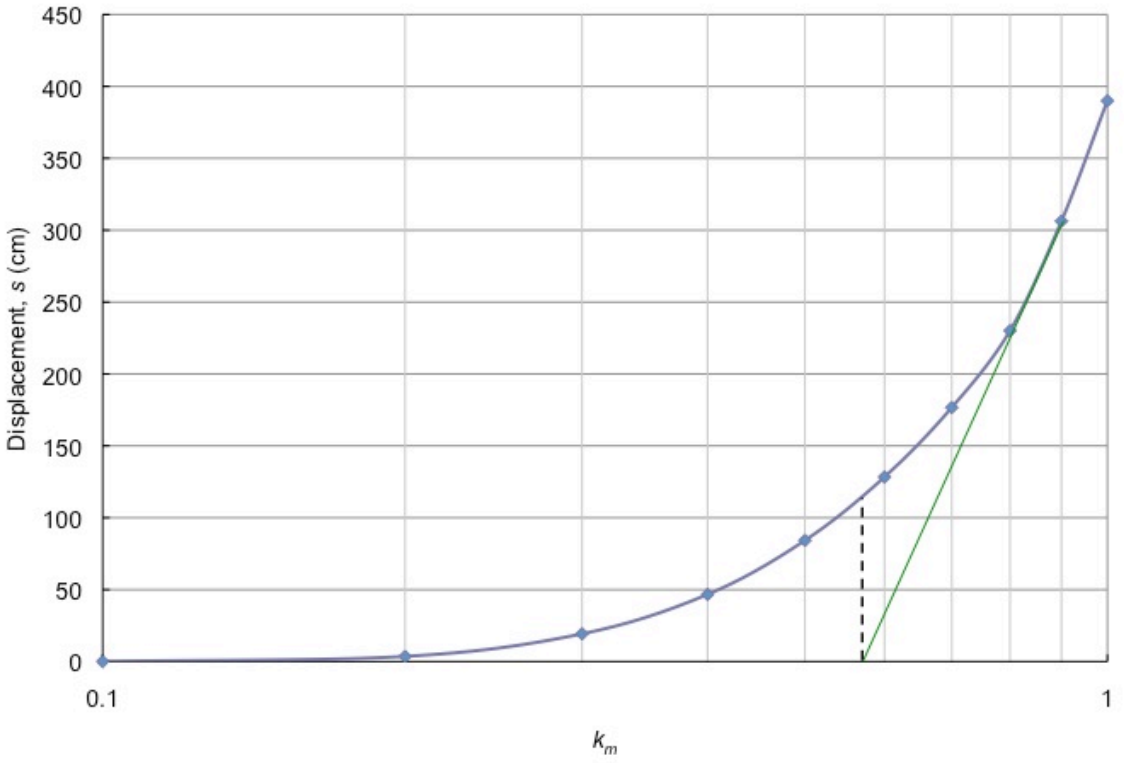

B.73. Permanent displacement calculated for the negative orientation of the fault-normal component accelerogram generated at El Salvador.

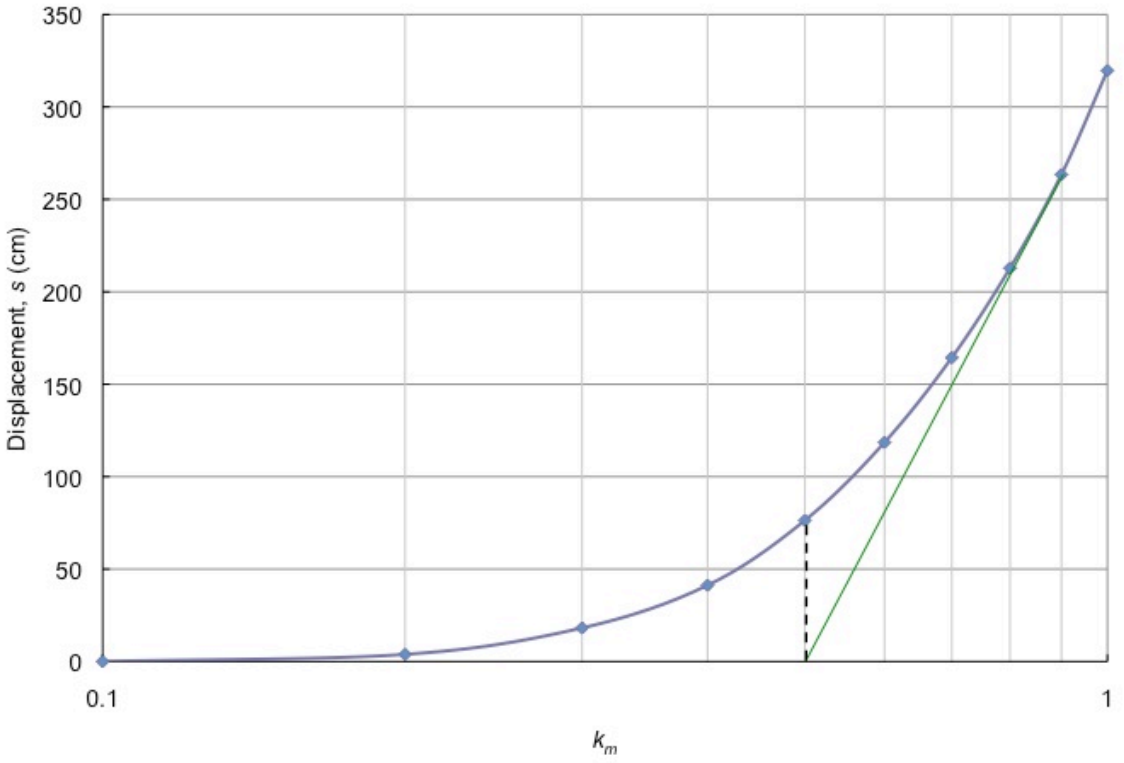

B.74. Permanent displacement calculated for the positive orientation of the fault-normal component accelerogram generated at El Salvador.

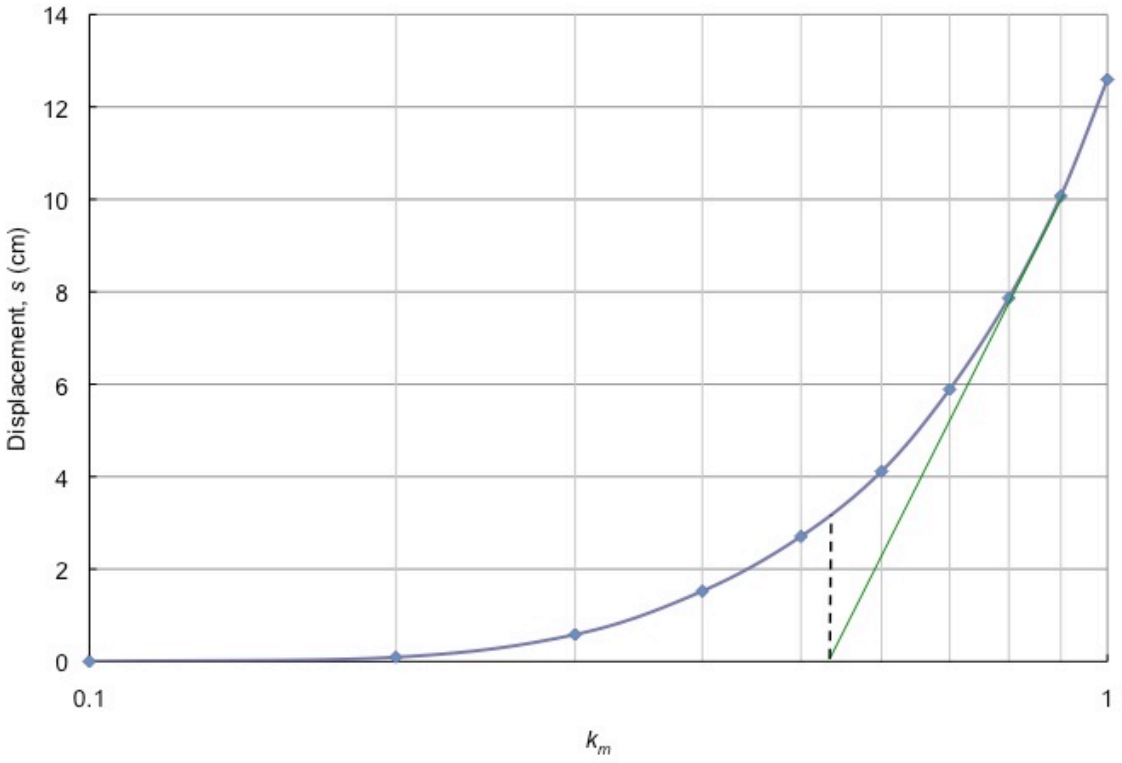

B.75. Permanent displacement calculated for the negative orientation of the fault-parallel component accelerogram generated at Gilroy, USA.

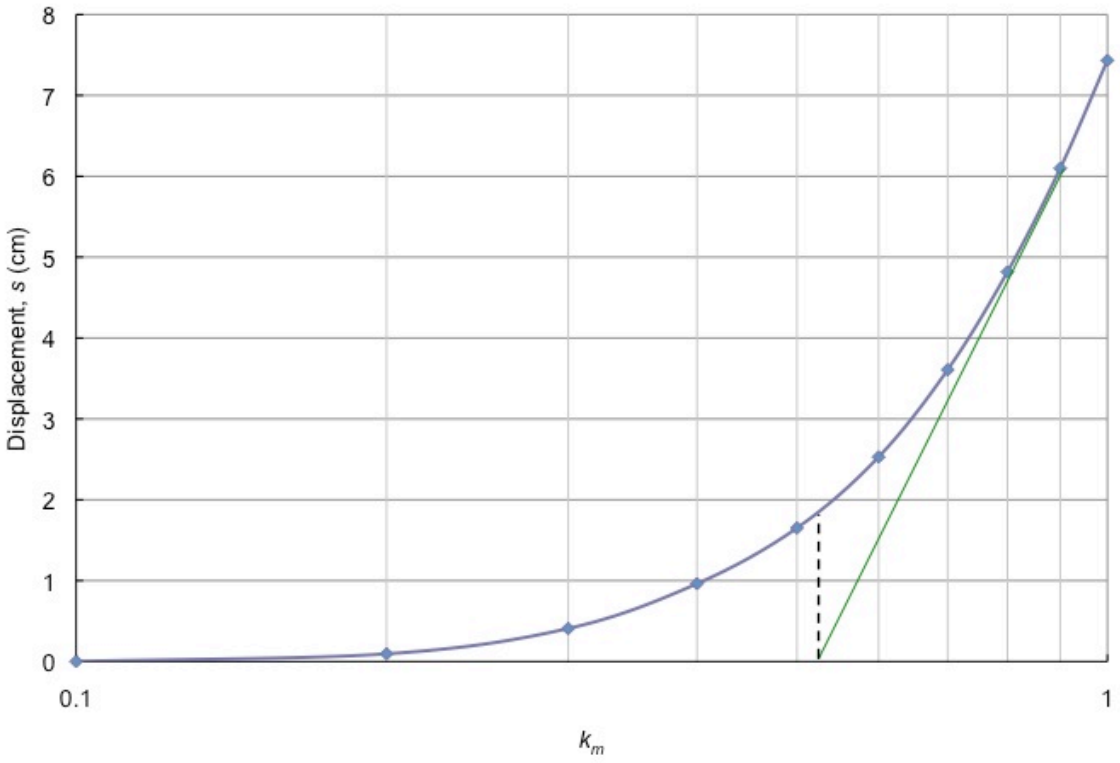

B.76. Permanent displacement calculated for the positive orientation of the fault-parallel component accelerogram generated at Gilroy, USA.

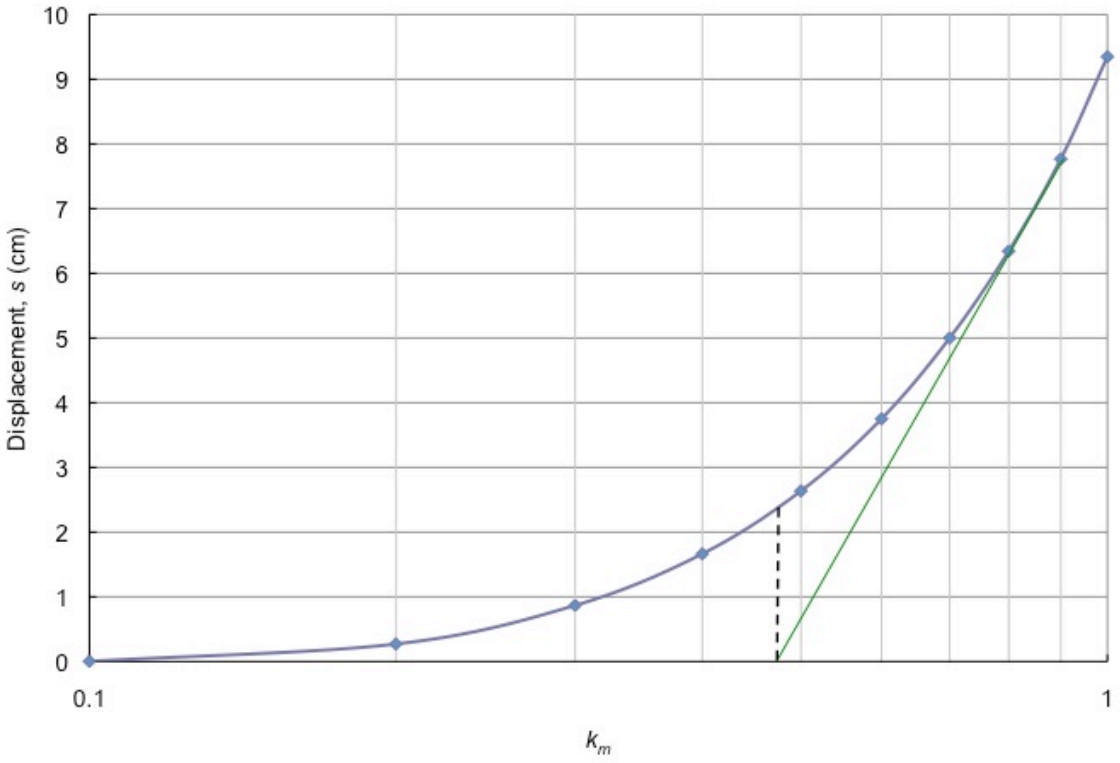

B.77. Permanent displacement calculated for the negative orientation of the fault-normal component accelerogram generated at Gilroy, USA.

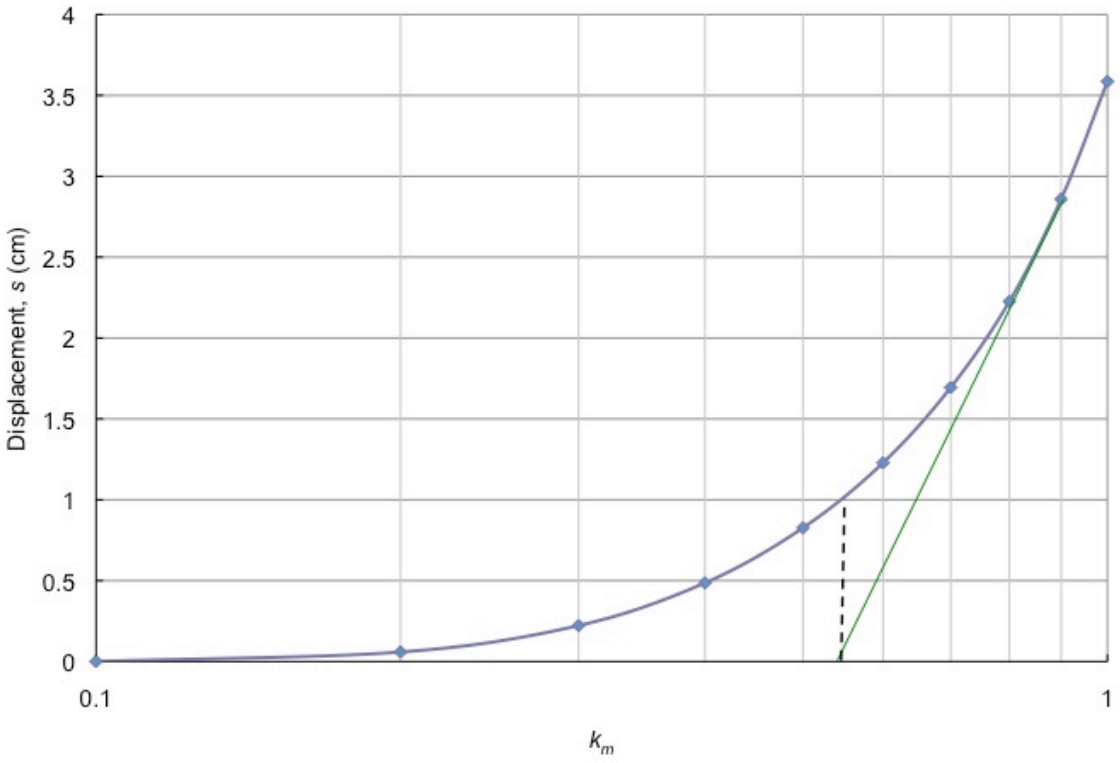

B.78. Permanent displacement calculated for the positive orientation of the fault-normal component accelerogram generated at Gilroy, USA.

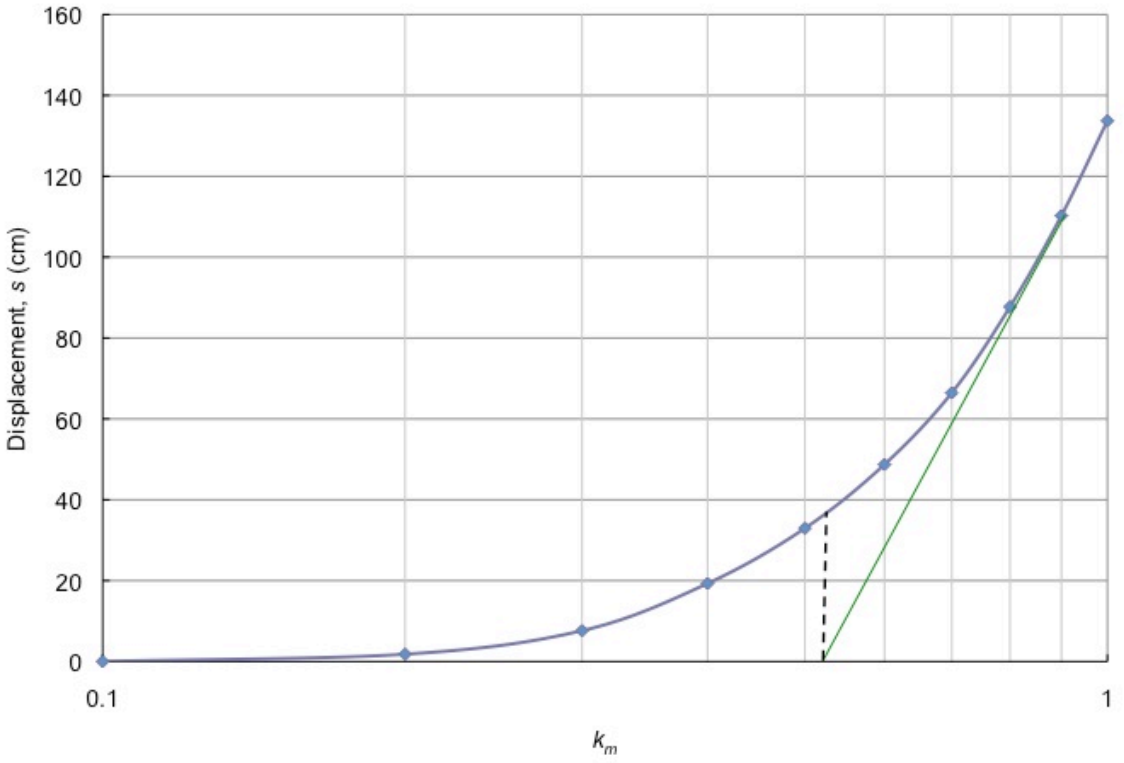

B.79. Permanent displacement calculated for the negative orientation of the fault-parallel component accelerogram generated at Kobe, Japan.

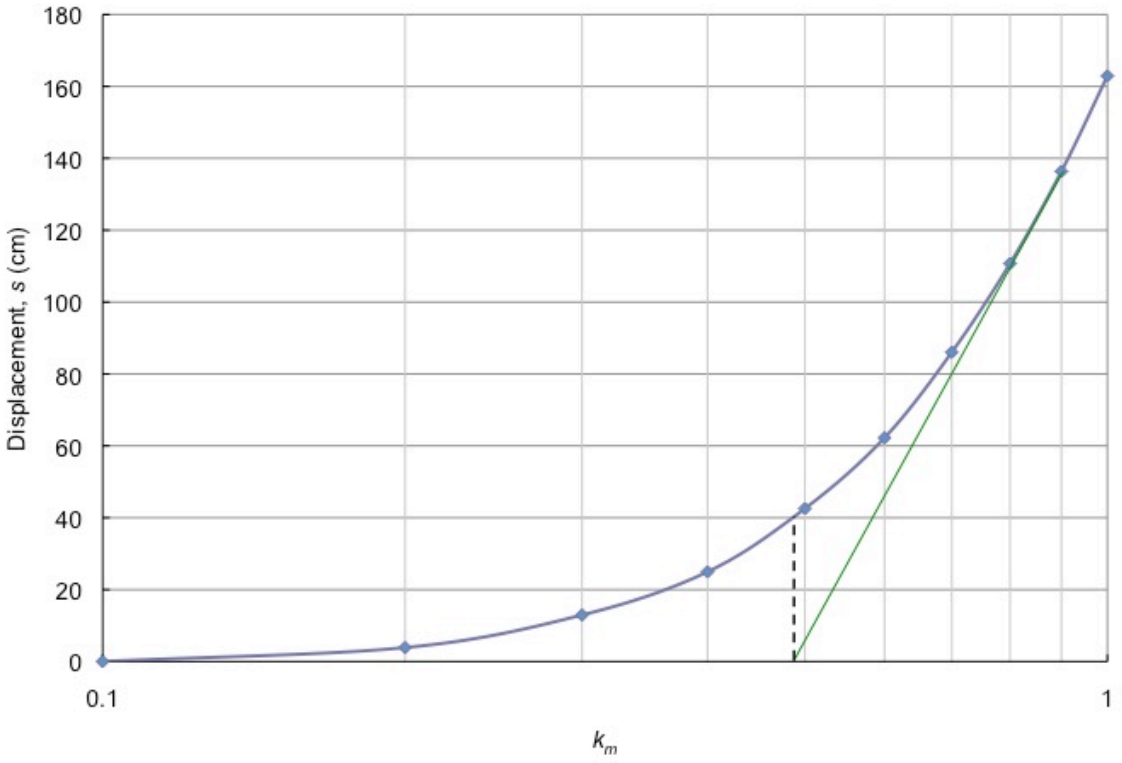

B.80. Permanent displacement calculated for the positive orientation of the fault-parallel component accelerogram generated at Kobe, Japan.

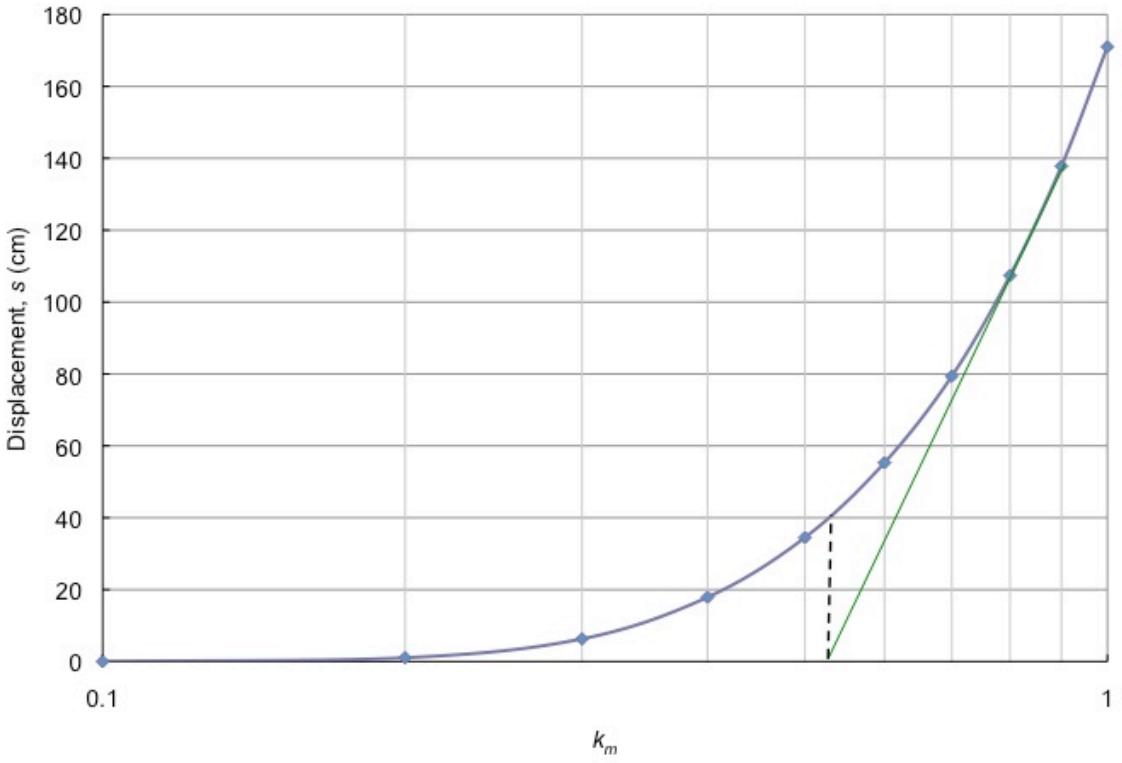

B.81. Permanent displacement calculated for the negative orientation of the fault-parallel component accelerogram generated at Loma Prieta, USA.

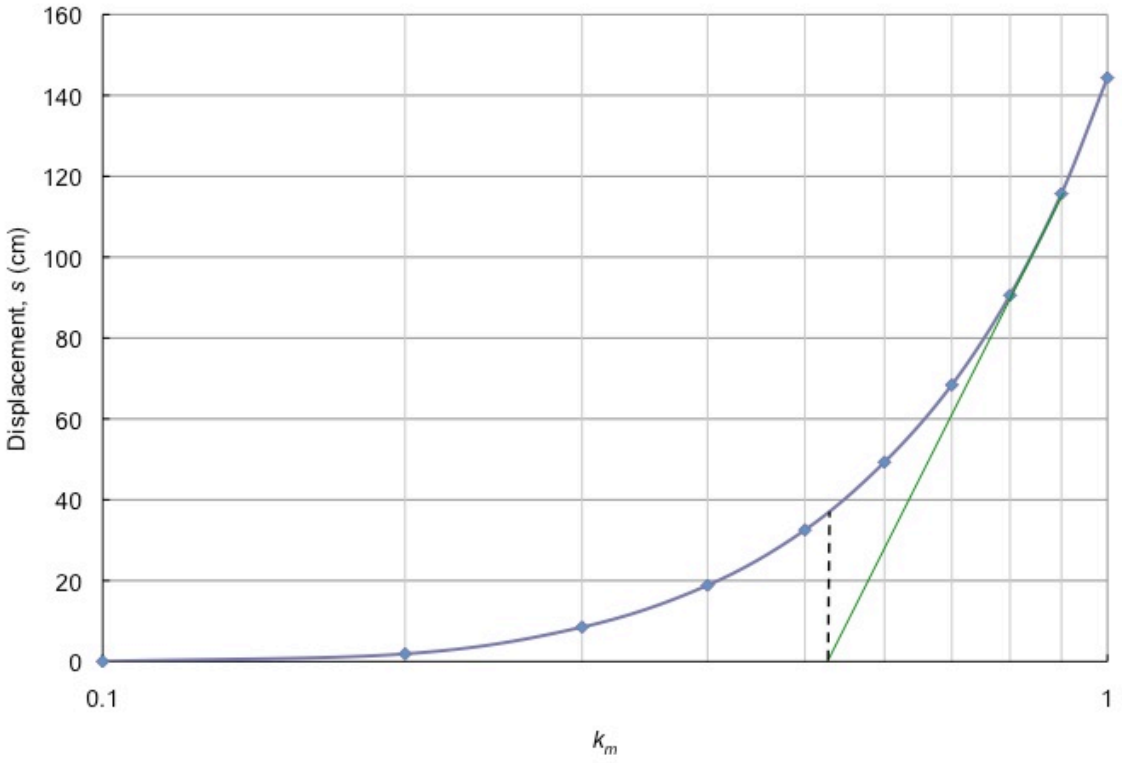

B.82. Permanent displacement calculated for the positive orientation of the fault-parallel component accelerogram generated at Loma Prieta, USA.

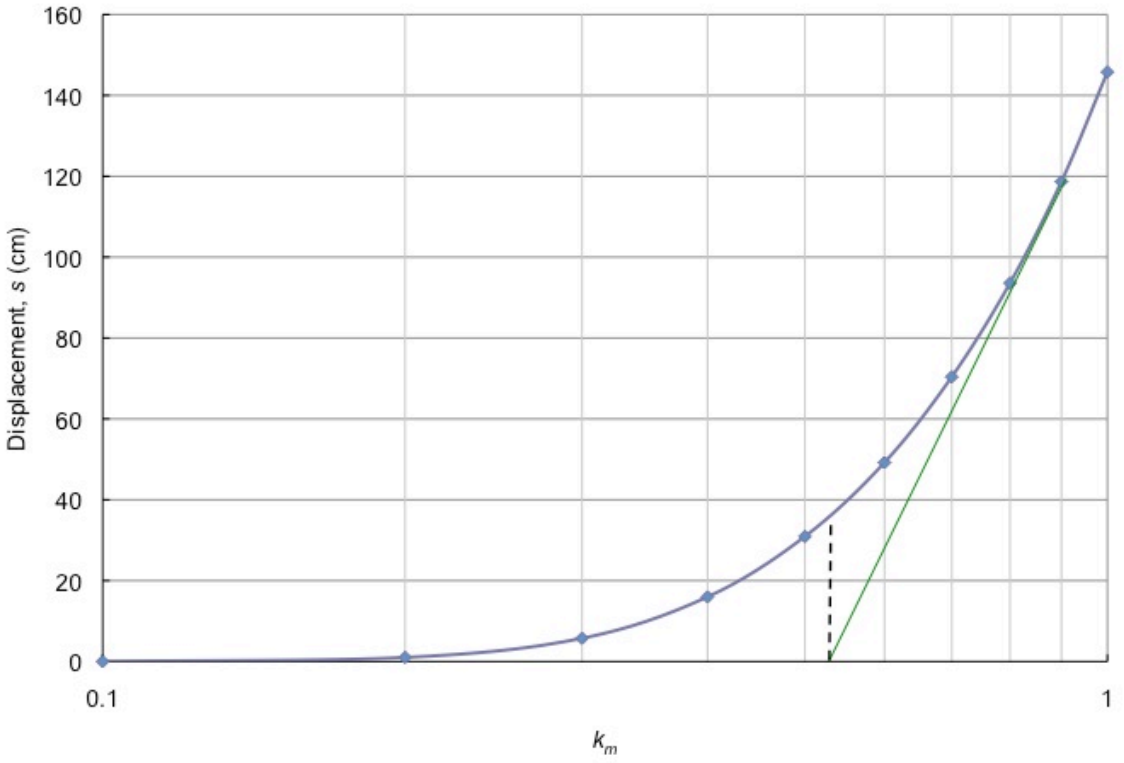

B.83. Permanent displacement calculated for the negative orientation of the fault-parallel component accelerogram generated at Loma Prieta, USA.

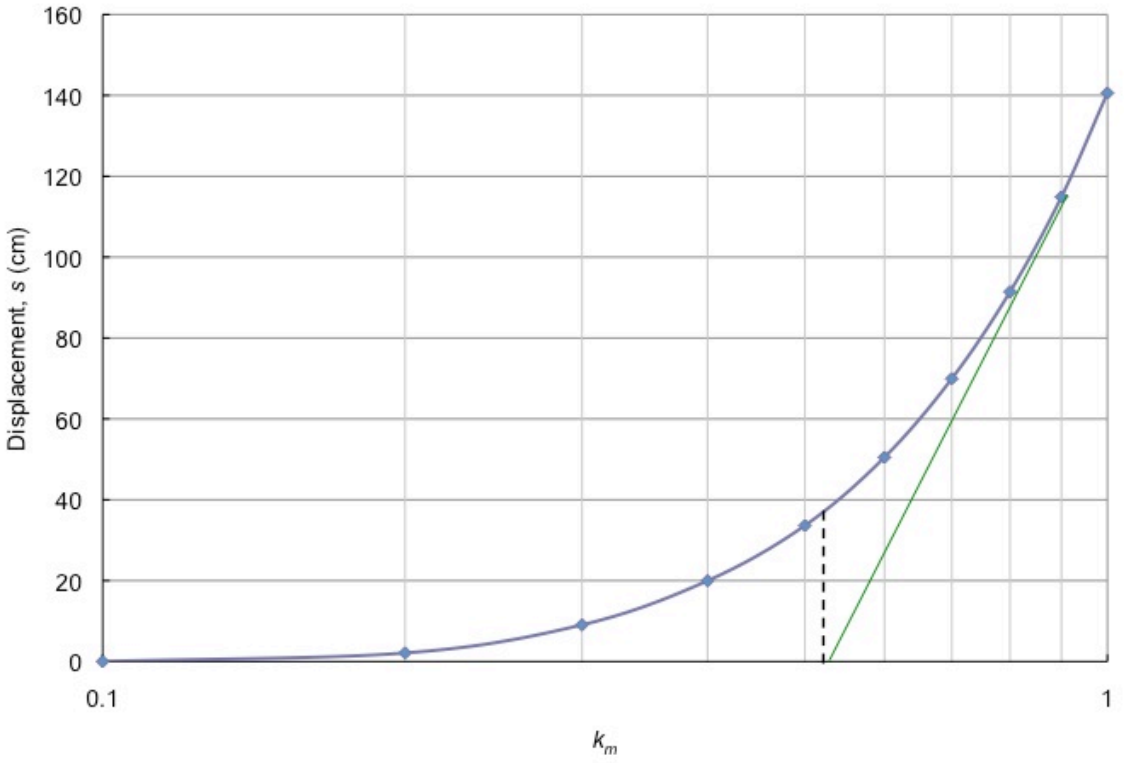

B.84. Permanent displacement calculated for the positive orientation of the fault-parallel component accelerogram generated at Loma Prieta, USA.

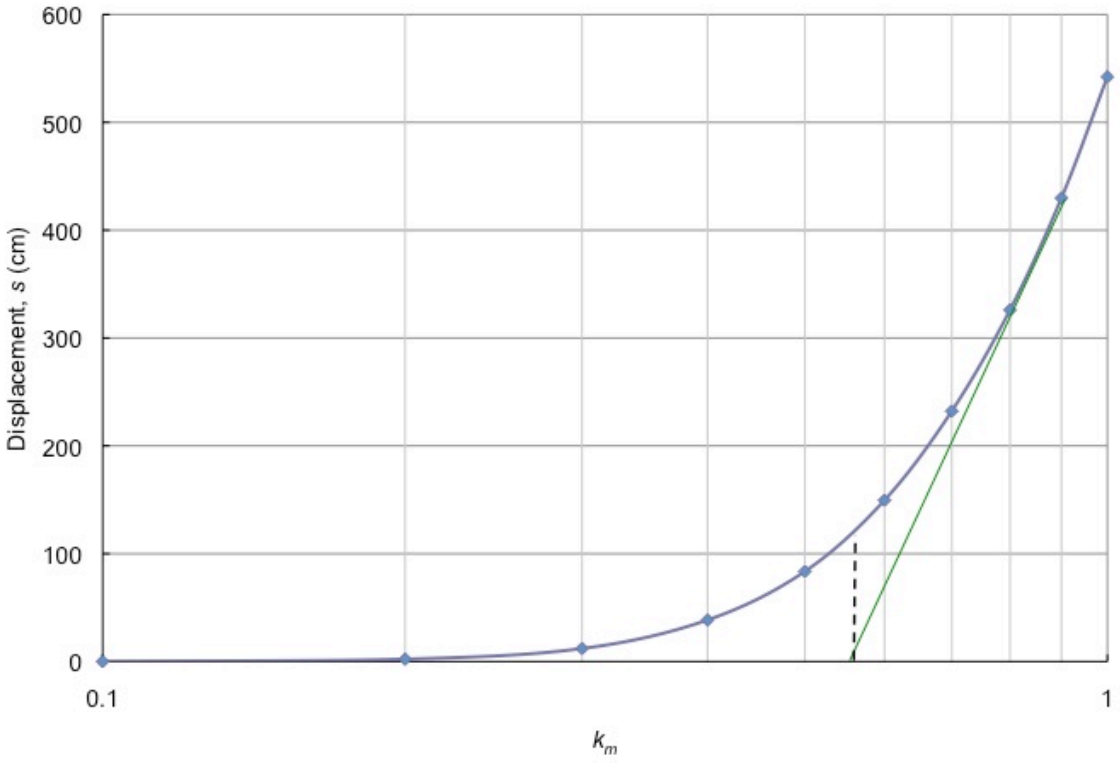

B.85. Permanent displacement calculated for the negative orientation of the fault-parallel component accelerogram generated at Taiwan.

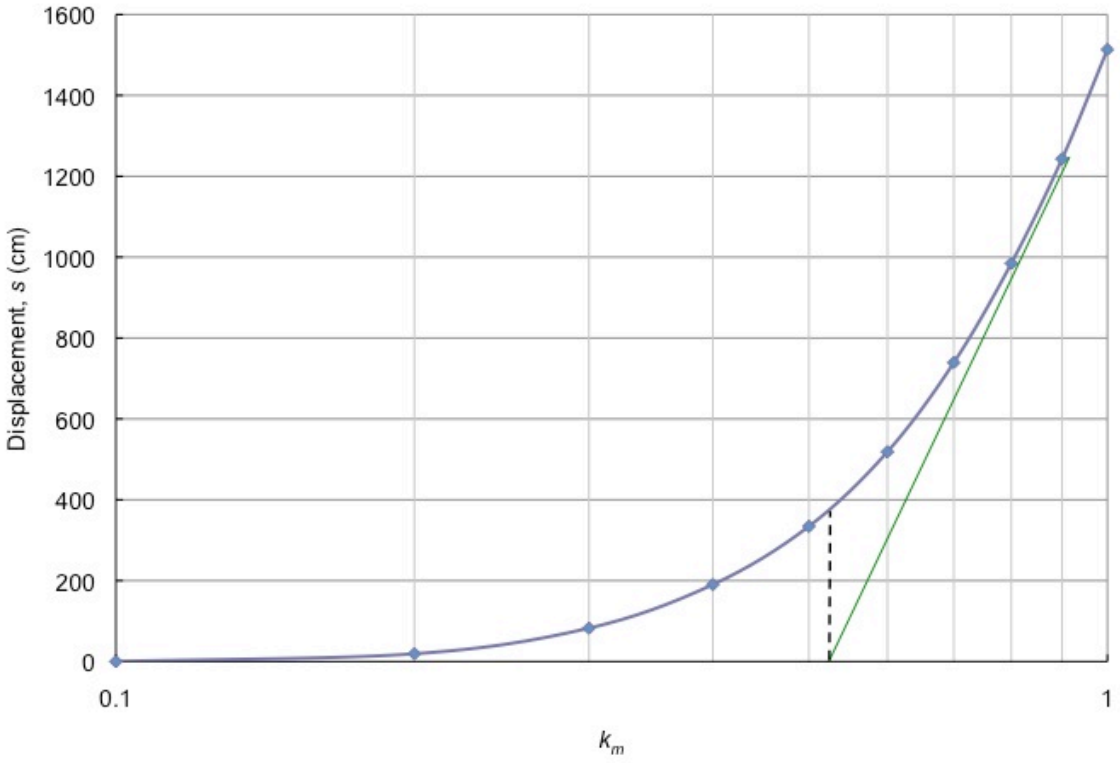

B.86. Permanent displacement calculated for the positive orientation of the fault-parallel component accelerogram generated at Taiwan.

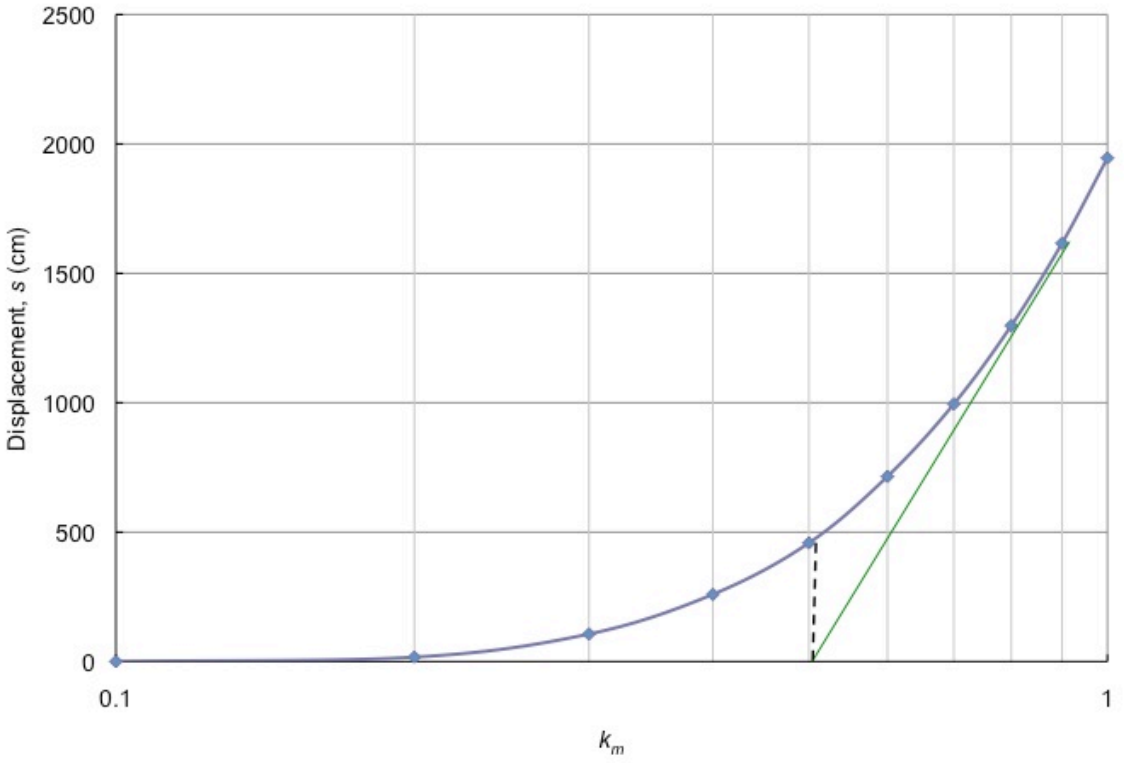

B.87. Permanent displacement calculated for the negative orientation of the fault-parallel component accelerogram generated at Taiwan.

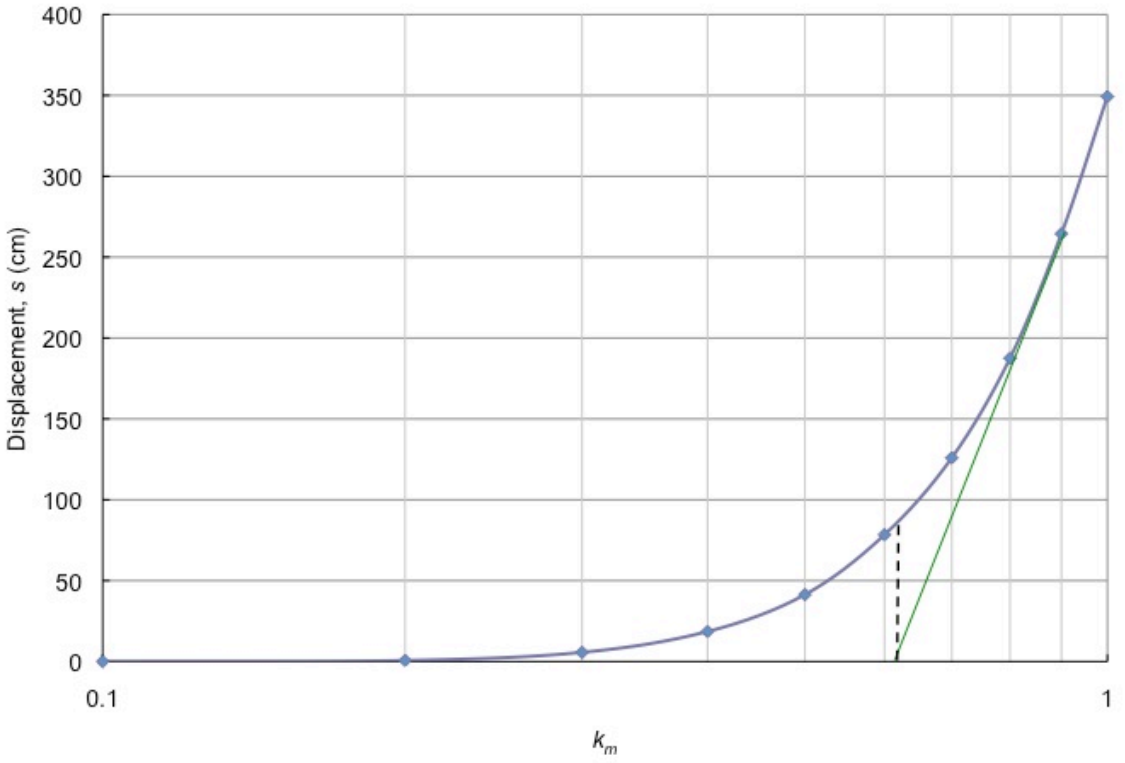

B.88. Permanent displacement calculated for the positive orientation of the fault-parallel component accelerogram generated at Taiwan.

REFERENCES

Arias, A. (1970). A measure of earthquake intensity, *in* Hansen, R.J., ed., Seismic design for nuclear power plants: Cambridge, Massachusetts, Massachusetts Institute of Technology Press, p. 438-483.

Ashland, F.X. (2007). Active landslides in the Creekside Drive area, Mountain Green, Morgan County, Utah, between June 2005 and December 2006. Utah Geological Survey Report of Investigation 260.

Ashland, F.X. (2008). Reconnaissance of the Draper Heights Landslide and other possible earthquake-induced, shallow, disrupted soil and rock slides near Draper, UT. Utah Geological Survey Open-File Report 519.

Ashland, F.X., Giraud, R.E., McDonald, G.N., and Elliott, A.H. (2008). Ground-water conditions in the Green Pond Landslide, Weber County, Utah. Utah Geological Survey Open-File Report 528.

Chugh, A.K. (1995). Dynamic displacement analysis of embankment dams. Geotechnique, v. 45 no. 2, p. 295-299.

Conforth, D.H. (2005). Landslides in Practice: Investigation, analysis, and remedial. Preventative options in soils. John Wiley & Sons, Inc., New Jersey.

Coogan, J.C., and King, J.K. (2006). Interim geologic map of the Durst Mountain quadrangle, Morgan and Weber Counties, Utah, Utah Geological Survey.

Duross, C.B., Personius, S.F., Crone, A.J., McDonald, G.N., and Lidke, D.J. (2009). Paleoseismic investigation of the northern Weber segment of the Wasatch Fault Zone at the Rice Creek trench site, North Ogden, Utah. Utah Geological Survey Special Study 130.

Forman, S.L., Nelson, A.R., and McCalpin, J.P., 1991, Thermoluminescence dating of fault-scarp-derived colluvium—deciphering the timing of earthquakes on the Weber segment of the Wasatch fault zone, north-central Utah: Journal of Geophysical Research, v. 96, no. B1, p. 595–605.

GEO-SLOPE International, Ltd. (2007). GeoStudio tutorials, Geo-Slope International Ltd, p 485.

Janbu, N. (1954). Applications of composite slip surfaces for stability analysis. in: Proceedings of the European Conference on the Stability of Earth Slopes, vol. 3. Stockholm, p. 39-43.

Jibson, R.W., and Harp, E.L. (1995) The Springdale landslide. In Christenson, G.E. (editor), *The September 2, 1992 Ml 5.8 St. George Earthquake, Washington County, Utah*, Utah Geological Survey Circular 88: Utah Department of Natural Resources, Salt Lake City, UT, pp. 21-30.

Jibson, R.W., and Harp, E.L. (1996) The Springdale, Utah, Landslide: An extraordinary event. Environmental & Engineering Geoscience, Vol. II, No. 2, Summer 1996, pp. 137-150.

Lund, W.R., 2005, Consensus preferred recurrence-interval and vertical slip-rate estimates—review of Utah paleoseismic-trenching data by the Utah Quaternary Fault Parameters Working Group: Utah Geological Survey Bulletin 134.

Machette, M.N., Personius, S.F., Nelson, A.R., Schwartz, D.P., and Lund, W.R. (1991) Segmentation and history of Holocenee arthquakes, Wasatch fault zone, Utah, Journal of Structural Geology, 13, 137-149.

McCalpin, J.P., Forman, S.L., and Lowe, M., 1994, Reevaluation of Holocene faulting at the Kaysville site, Weber segment of the Wasatch fault zone, Utah: Tectonics, v. 3, no. 1, p. 1–16.

Nelson, N.R., Lowe, M., Personius, S., Bradley, L.A., Forman, S.L., Klauk, R., and Garr, J. (2006) Holocene earthquake history of the northern Weber Segment of the Wasatch Fault Zone, Utah. Utah Geological Survey Miscellaneous Publication 05-8, 39 p., 2 plates.

Newmark, N.M. (1965). Effects of earthquakes on dams and embankments. Geotechnique, 15(2), 139-149.

ProMAX2D Seismic Data Processing Software (2003) Version 2003.12.1.

Reddy, K.R. (2002) Engineering properties of soils based on laboratory testing. http://www.uic.edu/classes/cemm/cemmlab/.

Stokes, W.L. (1977). Subdivisions of the major physiographic provinces in Utah. Utah Geol 4(1), 1-17.

Trandafir, A.C., and Sassa, K. (2005) Seismic triggering of catastrophic failures on shear surfaces in saturated cohesionless soils. Canadian Geotechnical Journal, v. 42, no. 1, pp. 229-251.

Trandafir, A.C., and Sassa, K. (2006) Performance-based assessment of earthquake-induced catastrophic landslide hazard in liquefiable soils. Geotechnical and Geological Engineering, no. 24, pp. 1627-1639.

Trandafir, A.C., and Amini, Z.A. (2009) Yielding mechanism of shallow mass movements in completely decomposed Norwood Tuff: the Zigzag Sign landslide, Utah. Environmental Geology, Vol. 57, No. 6, pp. 1443-1451.